

The
University
Of
Sheffield.

The identification and analysis of MHD waves and oscillations in localised solar atmospheric wave guides

Nabil Freij

School of Mathematics and Statistics
University of Sheffield

This dissertation is submitted for the degree of
Doctor of Philosophy

Supervisor: Robertus Erdélyi

September 2015

In memory of my father.

Declaration

I hereby declare that except where specific reference is made to the work of others, the contents of this dissertation are original and have not been submitted in whole or in part for consideration for any other degree or qualification in this, or any other university. This dissertation is my own work and contains nothing which is the outcome of work done in collaboration with others, except as specified in the text and Acknowledgements. This dissertation contains fewer than 65,000 words including appendices, bibliography, footnotes, tables and equations and has fewer than 150 figures.

Nabil Freij
September 2015

Acknowledgements

There are many people and organizations I would like to thank during the four years of my PhD.

Firstly, the official acknowledgements. To start, the instruments and their support teams who made this research possible. SDO/AIA and SDO/HMI data are used courtesy of NASA/SDO and the AIA and HMI science teams. The Swedish 1-m Solar Telescope is operated on the island of La Palma by the Institute for Solar Physics of Stockholm University in the Spanish Observatorio del Roque de los Muchachos of the Instituto de Astrofísica de Canarias. I want to thank Luc Rouppe van der Voort (Institute of Theoretical Astrophysics, University of Oslo) and J. de la Cruz Rodriguez (University of Uppsala, Sweden) for data reductions with MOMFBD for SST/CRISP. DST/ROSA and DST/IBIS data used in this thesis were obtained with the facilities of the National Solar Observatory, which is operated by the Association of Universities for Research in Astronomy, Inc. The DOT was operated by Utrecht University (The Netherlands) at Observatorio del Roque de los Muchachos of the Instituto de Astrofísica de Canarias (Spain) funded by the Netherlands Organisation for Scientific Research NWO, The Netherlands Graduate School for Astronomy NOVA, and SOZOU. The DOT efforts were part of the European Solar Magnetism Network. The SVST was operated by the Institute for Solar Physics, Stockholm, at the Observatorio del Roque de los Muchachos of the Instituto de Astrofísica de Canarias (La Palma, Spain). The computational tools used to analyse the data provided, AstroPy The Astropy Collaboration et al. (2013), Ginga, IPython (Perez and Granger, 2007), Matplotlib Hunter (2007), NumPy (Jones et al., 2001), SciPy (Jones et al., 2001), scikit-image (van der Walt et al., 2014), SolarSoft (Freeland and Handy, 1998), SunPy (The SunPy Community et al., 2015) and SymPy SymPy Development Team (2014) I want to thank J. Terradas for providing the EMD routines used in the data analysis. Wavelet power spectra were calculated using a modified computing algorithms of wavelet transform original of which was developed and provided by C. Torrence and G. Compo, and is available at URL: <http://paos.colorado.edu/research/wavelets/>. The Science and Technology Facilities Council (STFC) funded my studies and my travels around Europe.

Secondly, the people I have come across during my PhD. I would like to thank Steven Christie for inviting me to give a talk at NASA GSFC. Chris (and Helen by extension), for helping me throughout my PhD. Without his ability to encourage me to carry on and his technique for fine writing and science, I would have been very lost. Thank you for out doing me at every turn. I want to also thank Chris's seven papers for getting Chris his two jobs and keeping him around for Freddie. Tom, for his ability to ignore me whenever I say hello, I have never been so insulted. Freddie, for those gains, the numerous nights out (getting drunk has never been so fun) and his bitching talk at NASA GSFC. Stevie, for his inability to eat nice food which provided many hours of entertainment and his incredible ability to eat an entire loaf of bread in a single sitting. Stevie's mother for making sure Stevie had clean socks. Stuart, for all that Python support he provided me, without my papers would of been very barren. Sky (and Beth by extension), for letting me annoy them for 4 years (or was it just 3 months?) with my grating personality. It was an honour for me to be a part of your marriage and long it may continue. I want to thank my fountain pen collection for being there through thick and thin. The office has been a fantastic environment, through the magic craze, the ball games, the breaking incidents and the antics of Freddie. I do apologise for the loudness that I have caused. But I can say without hesitation, that it has been the best four years so far in my life and I have met some truly amazing human beings. Sorry I can't include everyone by name but I want to thank everyone else I have met during my PhD as well.

I would like to thank my PhD supervisor Robertus Erdélyi. Without him giving me the chance to do this PhD, I would be doing some sort of normal job. He believed in me and gave me this opportunity, which I am very grateful for. He has been a fantastic supervisor, encouraging me to push myself and being patient at the times I've been slow or stupid.

Last but not least, my family. I want to thank my mother and sister supporting me through my time at Sheffield. It as always been a comfort to know that I can go back whenever I needed to. I'll be home soon.

Abstract

There has been ubiquitous observations of wave-like motions in the solar atmosphere for decades and the presence of magneto-acoustic waves in magnetic structures in the solar atmosphere is well-documented. In this thesis, we aim to detect and identify magnetohydrodynamic (MHD) sausage waves in the lower solar atmosphere. In order to achieve this, high-resolution ground-based data is taken from numerous solar telescopes. For this thesis, two sunspots and three magnetic pore were chosen as examples of MHD waveguides in the lower solar atmosphere. Combining the Wavelet Transform and Empirical Mode Decomposition, we determined characteristic periods within the cross-sectional area and intensity time series and several oscillations have been detected within these waveguides. Then, by applying the theory of linear MHD, we identified the mode of these oscillations and concluded that they can be classified as slow sausage MHD waves. Further, we determined several key properties of these oscillations such as the radial velocity perturbation, magnetic field perturbation and vertical wavenumber using magneto-seismology. The estimated range of the related wavenumbers reveals that these oscillations are trapped within these magnetic structures. Our results suggest that the detected oscillations are standing harmonics, and, this allows us to estimate the expansion factor of the waveguides by employing magneto-seismology. Finally, we analysed Running Penumbral Waves (RPWs). RPWs have always thought to be radial wave propagation that occur within sunspots. Here, RPWs within a magnetic pore are observed for the first time and are interpreted as Upwardly Propagating Waves (UPWs) due to the lack of a penumbra that is required to support RPWs. These UPWs are also observed co-spatially and co-temporally within two elemental lines that sample the Transition Region and low corona. The observed UPWs are travelling at a horizontal velocity of around $17 \pm 0.5 \text{ km s}^{-1}$ and a minimum vertical velocity of $42 \pm 21 \text{ km s}^{-1}$. The estimated energy of the waves is around 150 W m^{-2} , which is on the lower bounds required to heat the quiet-Sun corona.

Table of contents

1	Introduction	1
1.1	The Sun	2
1.1.1	The structure of the solar interior	4
1.1.1.1	The Core	4
1.1.1.2	The Radiative Zone	5
1.1.1.3	The Tachocline	5
1.1.1.4	The Convection Zone	5
1.1.2	The solar atmosphere	5
1.1.2.1	The photosphere	6
1.1.2.2	The chromosphere	12
1.1.2.3	The transition region	14
1.1.2.4	The corona	15
1.2	MHD Theory	16
1.2.1	MHD Equations	16
1.2.2	MHD waves in cylindrical flux tubes	18
2	Data Collection and Analysis	23
2.1	Overview	24
2.2	Data Sources	24
2.2.1	Swedish Solar Telescope	25
2.2.2	Solar Dynamics Observatory	28
2.2.3	Other Ground Telescopes	28
2.3	Data Analysis	30
2.3.1	FFT	31
2.3.2	Wavelet Transform	33
2.3.3	Empirical Mode Decomposition	34
2.4	Area Analysis	35
2.4.1	Data Source	36

3 Analysis of Area Oscillations	45
3.1 Overview	46
3.2 Data collection and method of analysis	47
3.3 Results and discussion	50
3.3.1 LOS, circularity, and evolution of the waveguide	50
3.3.2 MHD theory for phase relations	50
3.3.3 Sunspot, 7 July 1999 , AR 8620	52
3.3.4 Sunspot, 13 July 2005, AR 10789	56
3.3.5 Pore, 15 October 2008	61
3.4 Standing harmonics	62
3.5 Conclusion	64
4 Slow MHD sausage waves	65
4.1 Introduction	66
4.2 Data and Method of Analysis	70
4.3 MHD wave theory	71
4.3.1 The sausage mode	71
4.3.2 Period ratio of standing slow MHD wave	74
4.4 Results and Discussion	75
4.4.1 DOT Pore	75
4.4.2 ROSA Pore	79
4.4.3 Standing Oscillations	82
4.5 Conclusions	87
5 Upwardly Propagating Waves	89
5.1 Introduction	90
5.2 Data Collection and Reduction	91
5.3 Results	93
5.3.1 The observed Active Region	93
5.3.2 Upwardly Propagating Waves	96
5.3.3 Energy of UPWs	101
5.4 Discussion	102
6 Conclusion	105
6.1 Overview of the thesis	106
6.2 Summary of Results	106
6.3 Future Work and Questions	110
References	113

Appendix A Mathematical Derivation	131
---	------------

Chapter 1

Introduction

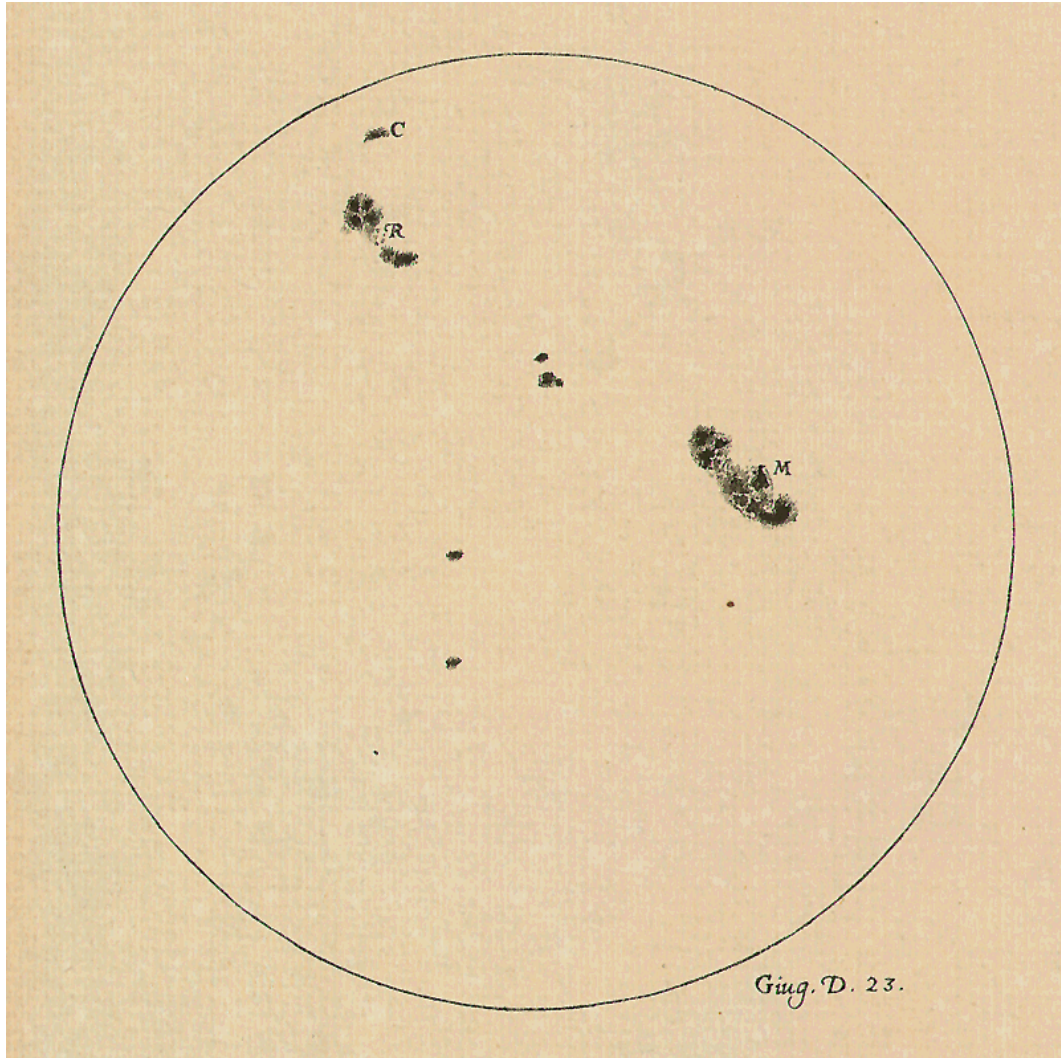


Fig. 1.1 A drawing of the solar surface by Galileo in the 17th century. The creation of the telescope forever changed astronomy. Here, the sunspot structure can be resolved; the inner (umbra) and outer (penumbra) regions can be seen clearly. Image credit goes to Project (2015).

1.1 The Sun

Our local star is known as the Sun and is a semi-common and uninteresting main sequence star (if you happen to be an astrophysicist). However to the general public and more importantly solar physicists, it forms the backbone of their lives. From simply as mundane as waking up at sunrise to making a long and (hopefully) successful career out of studying the Sun.

For early humans, it appeared as a giant ball in the sky that seemed to revolve around the Earth and it defied any human understanding. Since the dawn of mankind, the mythology surrounding the Sun has been numerous. From the New World, the Aztec's had a Sun god called Tonatiuh. Without constant human sacrifice (mainly

their enemies), they believed that the Sun would not move through the sky. From the Far East, the Chinese originally had 10 suns who took turns moving through the sky. However, these suns were mischievous and decided to all appear at the same time. This made life utterly unbearable on Earth, so an archer bestowed with a unique bow shot down 9 of the suns, leaving the one Sun we have today. From the Old World, the Greeks and Romans believed in Apollo who is the son of Zeus and Leto. He was known as the god of music, healing, light, truth and the Sun; a very busy god. With the decline of polytheism and the rise of monotheism, these gods and stories quickly became consigned to history. For a review of many more solar mythologies, see Olcott (1914).

The Sun had always been observed with the naked eye, sunspots had been visible and recorded by the ancient Chinese, further, many solar calenders were created to order human society. However, no systematic studies of the Sun had ever taken place. It took the enlightenment in Europe to mark the start of a transformation of society which led to the invention of the telescope (among other things). This is what started modern astronomy.

The telescope was the device that allowed humanity's knowledge of our solar system to radically change. It was possible to observe the Sun in much greater detail for the first time. Galileo drew many full disc images of the Sun and Figure 1.1 is one such example. With the telescope, the umbra and penumbra of sunspots was easily differentiated for the first time. Further, magnetic pores can be seen in the image. From here, many other discoveries were made such as the sunspot cycle, differential rotation and solar flares. With more time and a solar eclipse, layers of the solar atmosphere were finally observed, such as the chromosphere and the corona. The age of solar physics had finally begun.

The scientific understanding of the Sun has advanced by leaps and bounds, especially during the past sixty years. This is mainly due to the launch of space missions, whether it was SkyLab or the numerous satellites now pointed at the Sun. The removal of the Earth's atmosphere was a decisive step, allowing the observation of spectral lines not possible on Earth and vastly improving the quality of observational data. The solar physics community is hard at work analysing the massive amount of data that is available and expanding our knowledge of the Sun. However, there are still crucial challenges to overcome. They have in essence become the holy grails of solar physics: how the corona is heated and what is the dynamo process behind the solar magnetic field.

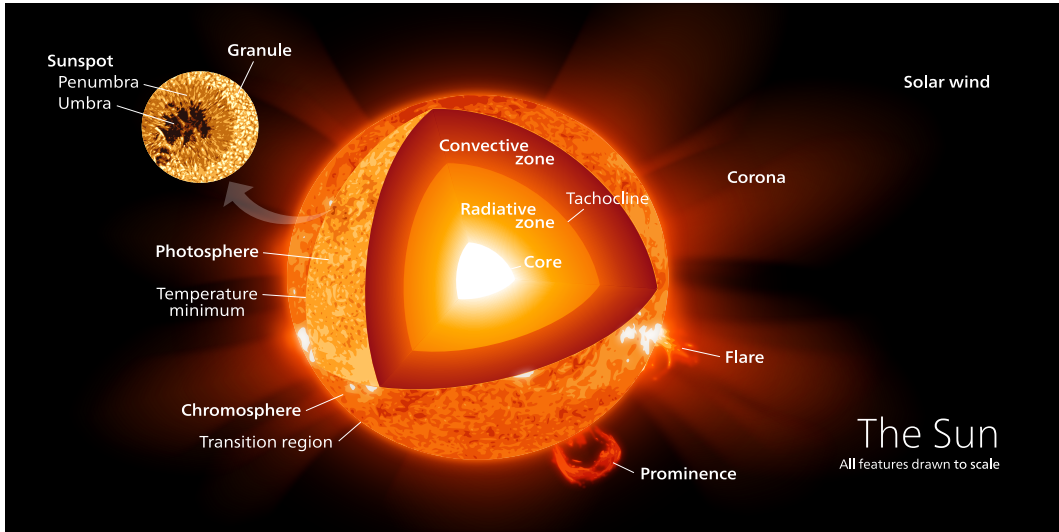


Fig. 1.2 A schematic diagram of the interior and external layers of the Sun. Also shown are several features that occur within the solar atmosphere; sunspots, granulation, flares and prominences. Image credit to Kelvinsong (2015).

1.1.1 The structure of the solar interior

The Sun's internal structure is divided into four sections; the core, the radiative zone, the tachocline and finally the convective zone. While we cannot see these regions directly, the process of helioseismology, much like seismology on Earth, has allowed humanity to come to grips with these layers and processes that occur within the Sun. Figure 1.2 showcases the multi-layered structure of the Sun. The image starts from the core, through the various interior layers until it reaches the solar atmosphere and the interplanetary medium. This picture of the Sun has been built up over time as observations and the mathematical models of the Sun have improved.

1.1.1.1 The Core

The core is the beating heart of the Sun, the largest fusion reactor this side of Centaurus. The core has more than 60% of the total mass of the Sun and extends roughly to 25% of the total radius of the Sun. It has a density of around 150000 kg m^{-3} and a temperature around 16 MK (Basu et al., 2009). The fusion reactions occurs due to the high pressure and temperatures that exist in the core, which are enough to force the hydrogen atoms together. This process which accounts for the vast majority of the energy generated, creates a range of high energy particles such as photons and neutrinos.

1.1.1.2 The Radiative Zone

Due to the intense heat and the large pressure within this region, thermal radiation is the only mechanism able to transfer the heat generated by the core. The process of radiative transfer within the radiative zone happens on very small scales. Photons are emitted and absorbed on very short time-scales. This means that it takes hundreds of thousands years for photons to exit this layer, which extends to about 70% of the solar radius (Cox et al., 1991).

1.1.1.3 The Tachocline

The tachocline is the region that separates the radiative zone and the convective zone. It is very thin, being only 0.04% of the solar radius. It has been long hypothesised that the solar magnetic field is created within this layer via a dynamo process (Soward et al., 2005).

1.1.1.4 The Convection Zone

From the tachocline, the temperature and pressure has decreased enough to allow the fully ionized molecules to retain some electrons and thus the opaqueness of the plasma increases. This traps part of the radiative energy from below setting up a temperature gradient sufficient enough to allow convection to take place. Thermal columns are created, which carry hot plasma to the surface of the Sun and once it cools, it sinks back to the base of the convection zone. This process is believed to cause gravity waves within the solar interior which have yet to be observed. The visible effect of convection is the solar granulation pattern that can be seen in white light images of the Sun. The pattern consists of cells that have a rough hexagonal shape. At the top of the convection zone, the temperature drops to 5700 K and the density to 0.0002 kg m^{-3} (Gai, 2000). A very important factor about the convection zone is the matter of differential rotation. The Sun rotates not as a solid body as the Earth does but as a fluid as the Gas Giants do. The rotation rate decreases from the equator where it is 25 days to around 34 days at the poles.

1.1.2 The solar atmosphere

The solar atmosphere is quite unlike the Earth's. While they both have multiple layers, the characteristics are wildly different (as you would expect). The top of the convection zone is the start of the first layer of the solar atmosphere. Here, the optical depth, the fraction of photons that can pass through the layer is $\lesssim 1$, roughly equating

to a third of all photons will pass into space. This layer is called the photosphere. There are three more layers, the chromosphere, the transition region and the corona (see Figure 1.2). Then the solar atmosphere transitions into the solar wind which fills the interplanetary medium.

1.1.2.1 The photosphere

The photosphere comes from the ancient Greek word “photos” meaning “light”. It is the visible surface of the Sun, that can be seen with the naked eye. The photosphere has an approximate thickness of 500 km with a starting temperature of 5700 K which drops as you move away from the surface, getting to approximately 4500 K. This part is called the temperature minimum and is generally taken to be the top of the photosphere.

The structure of the photosphere is composed of convection cells called granules, which are on average 1 Mm in diameter. Observed flows within these cells show uprising hot plasma in the centre which pushes the cooler plasma to the edges of the cell before flowing downwards. These granules are short-lived, with a lifetime less than 10 minutes, resulting in a repeating pattern at small-scales. These can be seen in the top image of Fig 1.3, within circle A. On larger scales, super-granule structures have been observed with a 30 Mm diameter which can last for a day or longer (Rieutord and Rincon, 2010).

The convective nature of the Sun has allowed us to infer the interior structure. The reason for this is that turbulence within the convection zone creates an entire spectrum of acoustic waves, named *p*-modes, where *p* stands for pressure. *p*-modes penetrate into the solar interior and at certain frequencies, the waves become standing. This sets up many standing modes that can be measured on the photosphere, using line-of-sight Doppler images. The mathematics used as a basis for this research is called spherical harmonics, and has allowed understanding of the many modes that are observed. The mode’s overall properties are affected by the physical conditions where the maximum amplitude for that mode occurs. This allows a building up of the information at each depth of the solar interior.

The dynamics of the photosphere is governed by two processes; convection as discussed above, but also by the solar magnetic field. This makes understanding how the magnetic field is structured within the photosphere important. The most common method employed in solar physics in order to measure the magnetic field is to exploit the Zeeman effect. This is the fact that when atoms are subjected to a magnetic field, their spectral lines split as a function of field strength and polarization. Unfortunately, this effect is only strong enough to be used in the photosphere where the magnetic

field is strongest. However, many solar physicists have attempted measurements in various weak field areas (Kontar et al., 2008; Lin et al., 2004; Metcalf et al., 1995). These images are called solar magnetograms and they have revealed the basic magnetic field structure at the photosphere. The magnetic field is very weak (≤ 300 Gauss) on average and is very sparse. This is referred to as the quiet Sun and is shown in the top image of Figure 1.3. The structuring from convection can be seen clearly as well as several features (which are discussed below). As can be seen, the magnetic field does not clearly dominate as strongly as it does in other regions.

Within the photosphere are small regions of concentrated magnetic field, named Magnetic Bright Points (MBPs). They are small-scale bright dots, as can be seen in Figure 1.3, in the circle labelled B. They are formed in the gaps between granule cells; the plasma flow has dragged the magnetic flux and thus becomes highly concentrated (>1 kG). The most likely reason for the increased brightness is that the flux tube has been evacuated of any plasma. As such, observations of MBPs allow a glimpse into the top of the convection zone, which has a higher temperature than the photosphere and is brighter. One important factor about MBPs was the observation of Alfvén waves (Jess et al., 2009; Taroyan and Erdélyi, 2009). This was able to supply enough energy to the corona to overcome the “Coronal Heating problem” (detailed in section 1.1.2.4).

Active Regions (ARs) are areas of intense magnetic field concentrations on the Sun’s surface. They are catalogued by the National Oceanic and Atmospheric Administration (NOAA) and are given numbers so they can be easily identified. ARs will vary in scale and what magnetic structures are present. Two of the most prevalent features within ARs are sunspots and magnetic pores. There are also many quiet Sun features and a whole raft of magnetic reconnection features. The top image of Figure 1.4 displays one such AR. It consists of 3 sunspots, taken as the AR is about to disappear off-limb. Circle A encloses one of the sunspots, but by being able to use a different wavelength filter we can observe an Ellerman Bomb (B) and a jet event (C). The last two events are associated with magnetic reconnection (Nelson and Doyle, 2013; Nelson et al., 2013a, 2015, 2013b).

When using a wavelength filter that resolves higher temperature plasma (≥ 1 MK), loop structures can be seen that rise several mega-meters in height. These are called coronal loops and they display a wide range of oscillations. Seismology of these loops, has estimated the background quantities such as density and magnetic field strength of these loops (see De Moortel (2005) or Banerjee et al. (2007) for a detailed review). These regions will also be the areas where flares or coronal mass

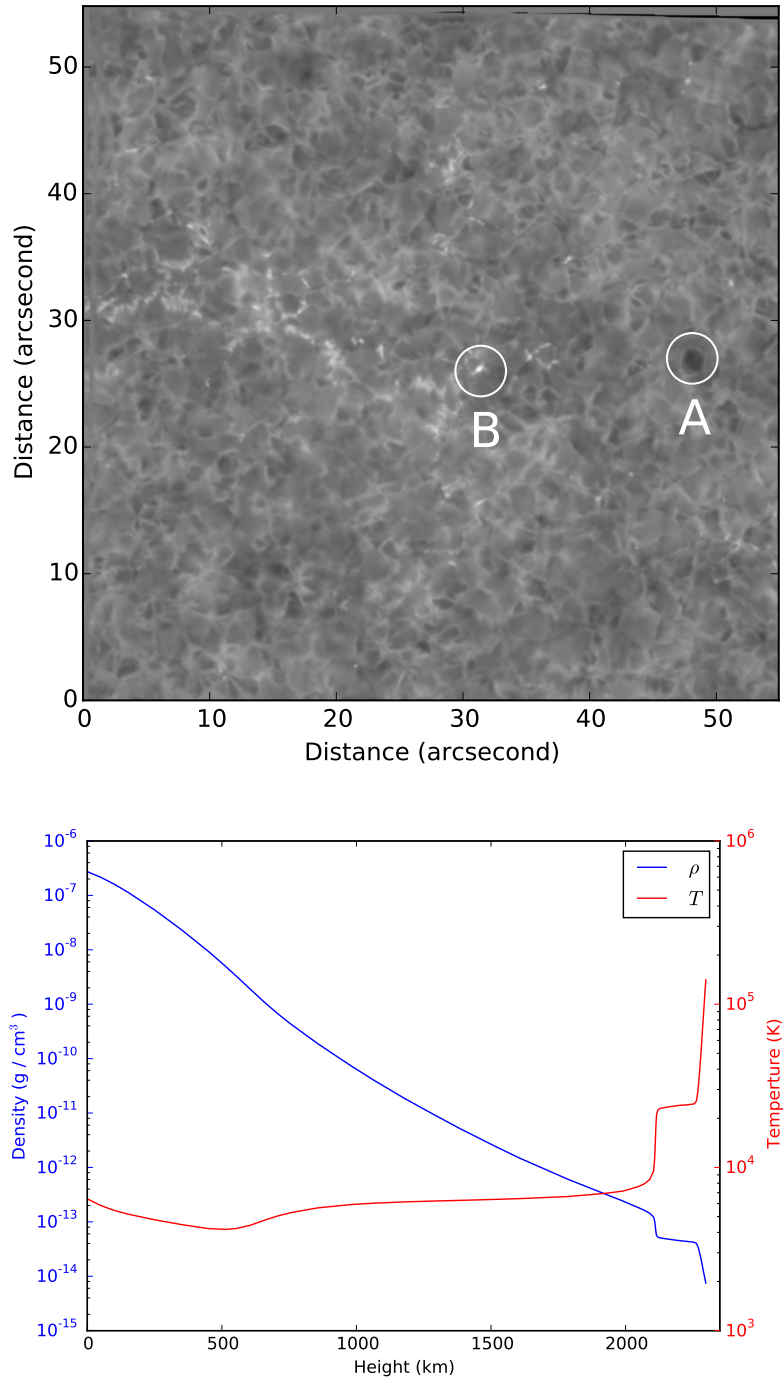


Fig. 1.3 (top) Iron I (630.2 nm) image taken with the Swedish Solar Telescope on the 22nd of July 2012. It shows some of the features that are present in the quiet Sun: a granule cell (A) and a magnetic bright point (B). **(bottom)** The VALIIIc (Vernazza et al., 1981) model of the quiet Sun, density is in blue and temperature is in red. The temperature minimum region and the transition region can be seen clearly with these two parameters.

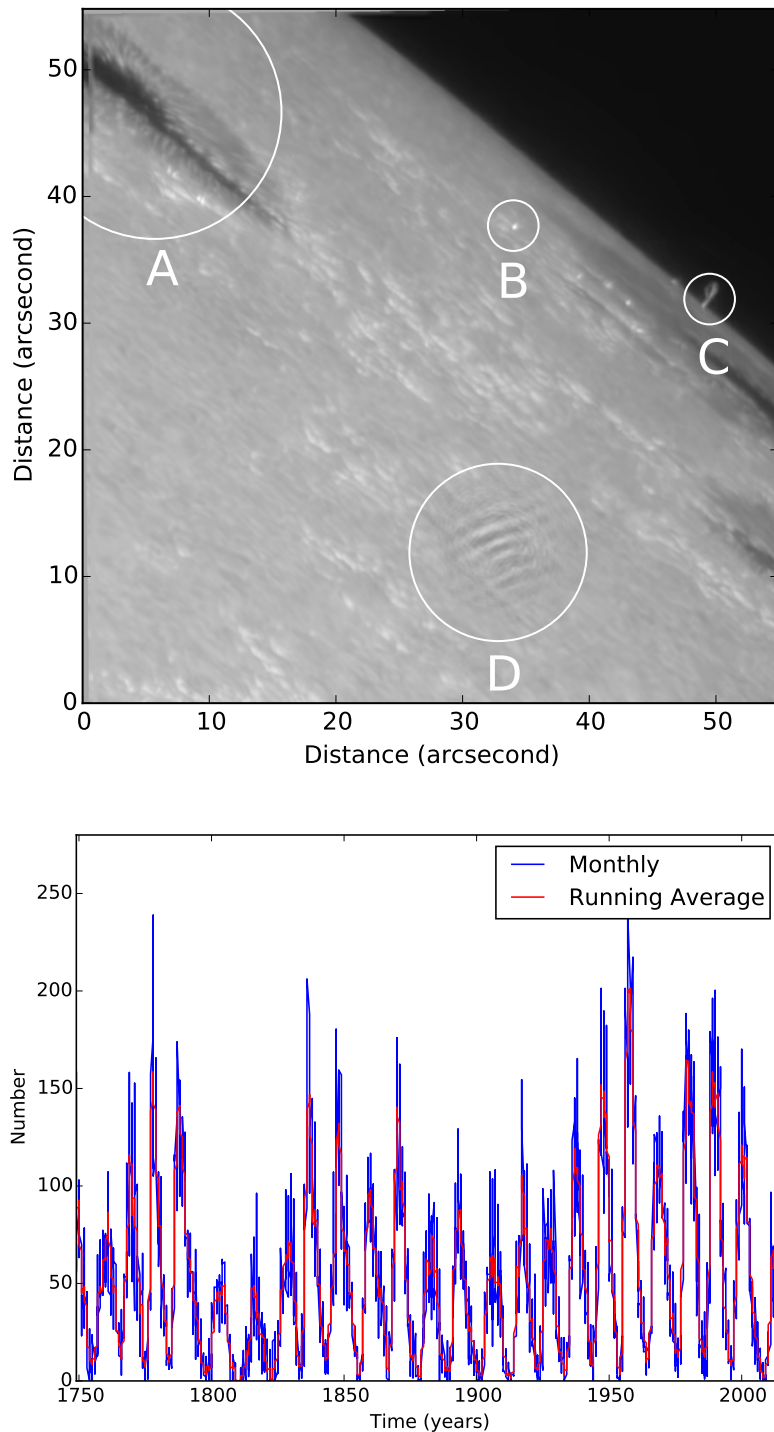


Fig. 1.4 (*top*) An image of an active region (NOAA 11504) sunspot taken at the Swedish Solar Telescope using the Crisp Imaging SpectroPolarimeter on the 21st June. The filter used is H α but into the far wings such that strong photospheric features can be observed. It shows some of the features that are present in Active Regions; sunspot (A), Ellerman Bomb (B), a jet (C) and seeing effects (D). (*bottom*) The sunspot number record as it currently stands since continuous tracking. The eleven year solar cycle is clearly visible.

ejections will originate from, since they contain large amounts of stored magnetic energy.

These are the most spectacular events produced by the Sun. The amount of mass and energetic particles ejected can be considered scary. These events have a direct impact on the Earth if the ejected material reaches Earth, from simply creating the aurora near the poles or in certain situations the disruption of radio transmissions, damage to satellites and electrical transmission lines. So it is important to understand the formation mechanism of these events so we can predict them and take measures to limit their damage. This is partly the realm of space weather research.

Sunspots are the strongest magnetic field concentrations on the solar surface. They have field strengths up to 4 kG, they can span up to 20 Mm in diameter. With the naked eye, they may appear to be dark spots, but with a good telescope, the sunspot structure can be seen to be divided into two parts. The first is the umbra which is the core of the sunspot, it is the coolest region (≈ 4000 K), as it is where the magnetic field is strongest and vertically inclined. The reason for the temperature difference between the sunspot and photosphere is that the magnetic field inhibits convection. This allows the plasma to cool down as no new hot material is being supplied. The second region is the penumbra and is made of elongated structures. Here the magnetic field is very inclined and weaker and fans around the umbra.

Sunspot formation is a hotly debated topic (as much things are in solar physics). One current hypothesis about their formation is as follows. The magnetic field of the Sun is strongly polarised and with differential rotation, these magnetic fields lines become bunched together, increasing the local magnetic field strength. This effect creates a buoyancy force which slowly makes this newly created flux region rise towards the surface until it penetrates into the photosphere. It should be noted, however, that a complete understanding of how sunspots form has not yet been achieved and the mechanism is likely to be more complex than the one described above. In fairness of balance, other hypotheses are available. A more thorough review of the formation, evolution and unanswered questions relating to sunspots can be found in e.g. Solanki (2003).

The solar cycle is an 11 year variation that the Sun undergoes where the polarity of the magnetic field flips. It is generally taken as 22 years since that returns the magnetic field back to its original polarity. The cycle does not have the same pattern or take the same amount of time each cycle. Generally, we have a solar maximum and a solar minimum. As the name suggests, we have a large amount of ARs and magnetic activity at a solar maximum, while this is reduced in a solar minimum. The solar cycle can be seen in the amount of sunspots which are visible (i.e., the

amount of ARs that form). This has been counted since the 17th century and it is called the sunspot number catalogue. The bottom image of Figure 1.4 displays this catalogue with the raw count as the blue line and a running average in red. This shows that the amount of sunspots varies with the cycle and that cycles can vary in length. Associated with the solar cycle is the variation in the number of “extreme” events, (flares and coronal mass ejections) and affects the overall structure of the solar atmosphere.

Closer to home, it also changes the amount of solar radiance and solar UV/EUV that reaches the Earth. Sunspots are directly linked to the Earth’s climate by the solar cycle (Friis-Christensen and Lassen, 1991). This can directly impact the Earth’s climate, as shown by the Maunder Minimum, which was an abnormally low amount of sunspots during the late seventeenth century and was the suspected cause of the “Little Ice Age”.

Sunspots have been under near constant observation. There are three main sunspot phenomena: 3 minute (5 mHz) and 5 minute (3 mHz) oscillations and running penumbral waves (RPWs). The first two are observed with a line-of-sight analysis, i.e, frequency filtering using the Fast Fourier Transform (FFT) (which is covered in Chapter 2). However, there is some evidence to suggest the existence of longer period oscillations (Chorley et al., 2011, 2010; Staude, 1999). The source of the 5-minute oscillations is thought to be a result of forcing by the 5-minute *p*-mode global solar oscillation (Christopoulou et al., 2003; Georgakilas et al., 2002). The 5-minute oscillations are typically seen in lines which form low in the cool umbral photosphere and are moderately suppressed not only in the penumbra, but also in the chromospheric atmosphere above the umbra (Bogdan and Judge, 2006). The cause of the 3-minute oscillations is still unknown but there are two main theories: they are either standing acoustic waves which are linked to the resonant modes of the sunspot, or, they are low- β slow magneto-acoustic waves guided along the ambient magnetic field (Bogdan and Judge, 2006; Christopoulou et al., 2000; Georgakilas et al., 2002; Kobanov et al., 2006). The 3-minute oscillations are seen in elements that form higher up, in the low chromosphere, and these are also moderately suppressed in the penumbra (Bogdan and Judge, 2006). However, it should not be assumed that the period of these waves forms one finite peak in a power spectrum; generally, the immediate spectral area around these periods has several peaks clustered tightly together. A review of sunspot oscillations can be found in (Bogdan and Judge, 2006) and a review of solar oscillations can be found in (Kosovichev, 2009).

Magnetic pores can be considered as smaller scale sunspots without a penumbra, sometimes referred as “naked umbra”. They share many general properties with

sunspots, for example, they display similar line-of-sight oscillations. Due to their small size, magnetic pores have not been under as much observation as sunspots since it took a new generation of solar telescopes to resolve them clearly. One example of a magnetic pore can be seen in Figure 1.5, which is studied in Chapter 5. But this image is in the $H\alpha$ core which samples the chromosphere which is discussed below.

1.1.2.2 The chromosphere

The next layer is visible from Earth during a total eclipse of the Sun as an intense red region giving it the name the chromosphere, from the Greek word “chroma”, meaning colour. It is roughly 2 Mm thick and is a highly complex layer. The temperature of the chromosphere increases with height and reaches around 20,000 K at the boundary where it meets the next layer, the transition region. The chromosphere has many small-scale structures that have been discovered over the past few decades. It is best observed in $H\alpha$ (a Hydrogen electron shell transition), where you can see these features but also another wavelength, Ca II K.

There are various names for these small-scale structures; spicules, fibrils, mottles and straws. The prevailing hypothesis is that there are two spicule types. Type I spicules are mainly seen in ARs but are scattered loosely elsewhere in the solar atmosphere. They can reach speeds up to 50 km s^{-1} and heights of 5 Mm before falling back down, with typical lifetimes of 3 to 10 minutes, diameters of 120 to 700 km and temperatures of 10 to 15 kK. On disc, they are called dynamic fibrils and called mottles in the quiet Sun. Fibrils tend to be more elongated than mottles which are shorter.

Type II spicules are located more often in the quiet Sun. They are faster (up to 150 km s^{-1}), longer (up to 10 Mm) and have a significantly reduced lifespan (up to 150 s) when compared to Type I spicules. On disc, they are referred to as straws or more commonly Rapid Blue-shift Events (RBEs) (Zaqarashvili and Erdélyi, 2009). Finally there is another fibril type that are long and mostly horizontal and longer-lived than dynamic fibrils. Some of these features are highlighted in Figure 1.5. The circle A, has a good example of fibrils, long and fairly static, while circle C, shows dynamic fibrils which continually moved and swayed under our observation.

These structures have been under heavy investigation as a potential source of energy transport in the solar chromosphere. Morton et al. (2012) using ground-based observations discovered incompressible transversal motions for fibrils which match the ones observed for limb spicules which were interpreted as Alfvén waves (De Pontieu et al., 2007). Further, fast compressive MHD waves were also observed. The

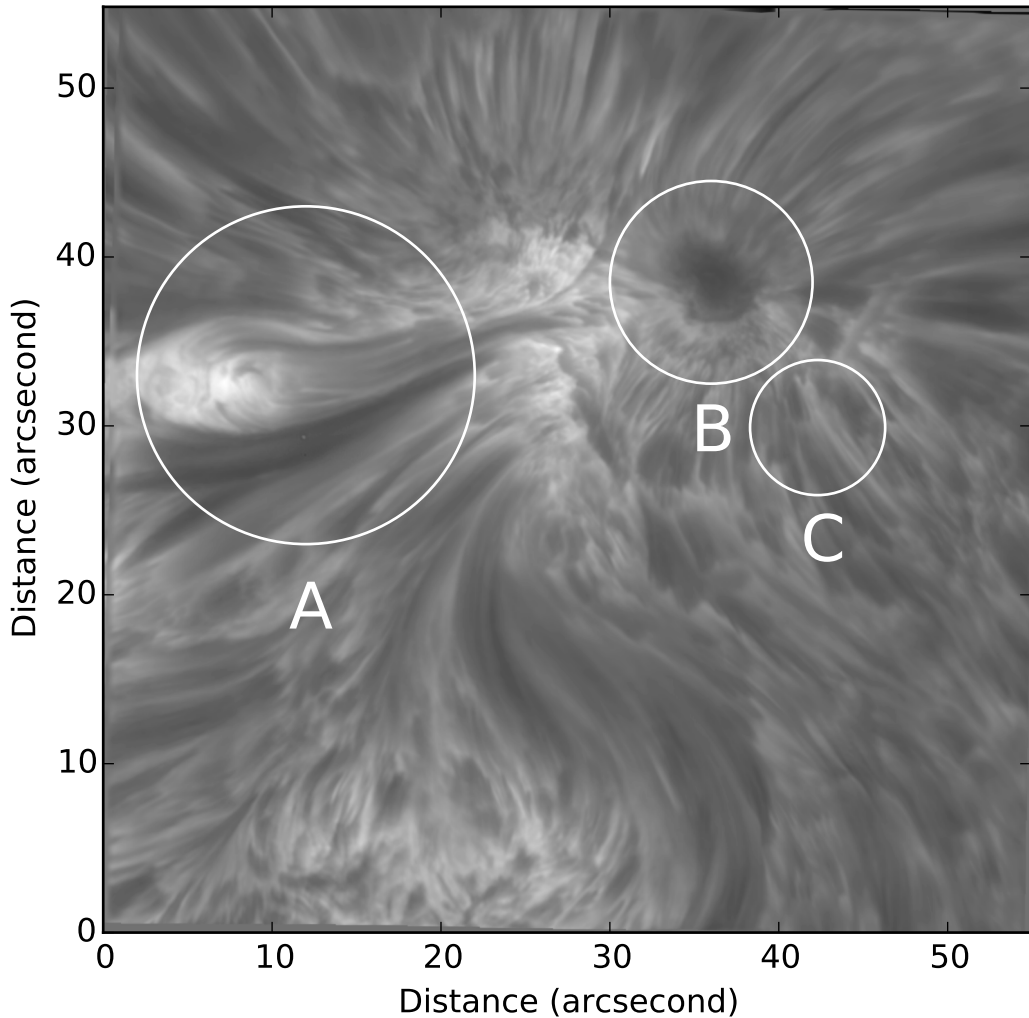


Fig. 1.5 A H α line core image of Active Region NOAA 11510 observed on the 22nd June 2012. Here, this AR has a large pore that displays Running Penumbral waves (the focus of Chapter 5). Highlighted here are fibrils (A), the magnetic pore (B) and dynamic fibrils (C). The complex nature of the chromosphere can be seen in detail and it still needs a full explanation.

estimation of the energy these waves carry is quite large but explaining how they dissipate this energy is unknown at this time. A review of oscillations in spicules can be found by Zaqrashvili and Erdélyi (2009).

Running Penumbral Waves (RPWs), are a phenomenon discovered by Zirin and Stein (1972) and Giovanelli (1972). Observed in H α in sunspot penumbrae, they are seen as a wave train of enhanced darkness that goes from the umbra to the penumbra. They tend to be concentric and cover a large azimuthal angle. On average, they have a speed of 15 to 20 km s $^{-1}$ before slowing to 5 to 7 km s $^{-1}$ at the end of the penumbra. They have a period typically of 200 to 300 seconds. Common interpretation is that much like the 3-minute oscillations, they are slow magneto-acoustic wave propagating upwards along the inclined magnetic field and the radially outwards movement is actually a visual pattern (Bogdan and Judge, 2006; Christopoulou et al., 2000; Kobanov et al., 2006). This is expanded on in Chapter 5.

Finally, we discuss the existence of a Moreton wave (Moreton, 1960). These are seen also in H α wings as a dark and then a bright front. They are observed to travel away from flaring regions and are generally confined to a specific arc. They are more of a pulse than a wave and can travel up to 2000 km s $^{-1}$.

1.1.2.3 The transition region

Above the chromosphere, is a thin (≈ 100 km) layer where the temperature rises rapidly from 20,000 K to 1,000,000 K. This is called the transition region. The rate of the increase is exponential and the density in this region decreases at a similar rate. In the bottom image of Figure 1.3, which displays the temperature and density of a semi-empirical model of the quiet Sun, this behaviour can be seen. This clearly means that the region is very non-uniform and (Tian et al., 2009) suggest that the height varies depending on what is below. It cannot be observed from the surface of Earth, but can be from space-borne instruments sensitive to ultraviolet and extreme ultraviolet light.

Spicules, as discussed above, rise to large heights and it had been hypothesized that the TR would be a boundary. The spicule should hit the TR and create some form of a disturbance. These were discovered and called Transition Region Quakes (TRQs), found using the Extreme-Ultraviolet Imaging Spectrometer (EIS) instrument on-board the Japanese satellite Hinode. Coupled with MHD simulations, the disturbance was identified as a fast magneto-acoustic-gravity wave (Scullion et al., 2011). These events further cement the link between the lower solar atmosphere and the higher regions.

1.1.2.4 The corona

The next layer is the outer atmosphere of the Sun called the corona. It is most easily seen during a total solar eclipse, but also observable using a coronagraph. The average temperature of the corona is about 1-2 MK, however, it reaches as high as 8-10 MK. The sheer scale of the corona is impressive. It is large in volume and it continuously expands into the solar system (i.e the solar wind) and stops far past the orbit of Pluto. The mechanism which accounts for the high temperature of the corona is still unknown, but two main ideas are in contention. Magnetic reconnection; the ability for the magnetic field to change its topology to release energy into the local environment, in order to heat the local plasma, or, MHD waves travelling up from the photosphere and dissipating their energy into the surrounding plasma.

In all likelihood, a combination of these two main ideas will be the source behind coronal heating. This topic has been heavily researched for many decades and you can see reviews by e.g. Erdélyi (2004); Parnell and De Moortel (2012). The most recent development has shifted the question, from “how do you heat the corona?” to “how do you heat the chromosphere?”(Aschwanden et al., 2007). For example, many sources of energy exist for wave heating (Parnell and De Moortel, 2012).

The corona is host to many structures, X-ray bright points, plumes, prominences, streamers, coronal loops and coronal holes. Coronal holes are open magnetic structures which give rise to the fast solar wind, while coronal loops are one of the best examples of large scale magnetic structures within the solar atmosphere. They are typically up to one solar radius long and have a temperature of 2 to 3 MK.

For a long time, it was hypothesised that MHD waves would not be able to go into the corona as the cut-off frequency would stop them. The launch of the Transition Region And Coronal Explorer (TRACE) space solar telescope changed this (Handy et al., 1999; Strong et al., 1994). Numerous MHD oscillations were observed; damped transversal oscillations (Goossens et al., 2002; Ofman and Aschwanden, 2002), standing fast kink waves (Aschwanden et al., 1999; Nakariakov et al., 1999; Schrijver et al., 1999), standing acoustic modes (Wang et al., 2003), fast sausage (Katsiyannis et al., 2003; Williams et al., 2002, 2001), fast kink waves (Verwichte et al., 2005), propagating acoustic modes (De Moortel et al., 2000; Marsh et al., 2002; Ofman et al., 1997) and torsional modes (Erdélyi et al., 1998). This lead to a large focus on coronal seismology; estimating the background properties of coronal loops using observed properties of the waves. See a review on this topic by Nakariakov and Verwichte (2005). Finally, EIT waves discovered using the Extreme Ultraviolet Imaging Telescope (EIT) instrument on the Solar and Heliospheric Observatory (SOHO) space satellite (Thompson et al., 1998). These are large single-pulsed

propagating fronts which appear to move unhindered throughout the corona after a large-scale event (such as a flare). They are believed to be associated with Moreton waves.

Overall, this has been a brief overview of the history of the Sun, its interior and atmosphere. For a more detailed introduction to the Sun, see Priest (1984) or Priest (2014).

1.2 MHD Theory

The mathematical underpinning used in solar physics is called magnetohydrodynamics (MHD). It adds the effects of a magnetic field to the governing equations of fluid mechanics. More accurately, it is the melding of Maxwell's equations to the Navier-Stokes equations. This is credited to Hannes Alfvén, who won a Nobel Prize in Physics for this major contribution to science (Alfvén, 1942; Erdélyi and Fedun, 2007).

1.2.1 MHD Equations

One of the most repetitive parts in any solar physics thesis is what is about to follow. There are several equations that form the core of MHD and are solved in many different magnetic configurations. The ultimate aim is to understand how these configurations will evolve in time or how they react to external factors. Further, they are solved to find out what kind of waves these configurations can support as well as how they disturb the equilibrium. The MHD equations include many physical effects, however, we have taken the ideal assumption; adiabatic, inviscid, radiation, no thermal conduction and no resistivity. This is ideal MHD and the resulting equations are,

$$\frac{\partial \rho}{\partial t} + \nabla \cdot (\rho \mathbf{v}) = 0, \quad \text{(Mass Conservation)}$$

$$\rho \frac{D\mathbf{v}}{Dt} = -\nabla p + \frac{1}{\mu}(\nabla \times \mathbf{B}) \times \mathbf{B} + \rho \mathbf{g}, \quad \text{(Equation of Motion)}$$

$$\frac{D}{Dt} \left(\frac{p}{\rho^\gamma} \right) = 0, \quad \text{(Energy Equation)}$$

$$\frac{\partial \mathbf{B}}{\partial t} = \nabla \times (\mathbf{v} \times \mathbf{B}), \quad \text{(Induction Equation)}$$

subject to

$$\begin{aligned}\nabla \cdot \mathbf{B} &= 0, && \text{(Solenoid Equation)} \\ p &= k_B \frac{\rho}{m} T, && \text{(Ideal Gas Law)} \\ \mathbf{E} &= -\mathbf{v} \times \mathbf{B}, && \text{(Ohm's Law)} \\ \mathbf{j} &= \nabla \times \mathbf{B} / \mu. && \text{(Electric Current)}\end{aligned}$$

Here ρ is the density, \mathbf{v} is the velocity, $\frac{D}{Dt}$ is the convective derivative $(\frac{\partial}{\partial t} + (\mathbf{v} \cdot \nabla))$, p is the pressure, γ is the ratio of specific heats (5/3), \mathbf{B} is the magnetic field, k_B is Boltzmann's constant, m is the mass, T is the temperature, \mathbf{E} is the electric field, \mathbf{j} is the current density and μ is the vacuum permeability.

There are actually eight partial differential equations for eight variables. Both \mathbf{v} and \mathbf{B} have three components each and we have the density and temperature. From this, the typical recourse is to examine the case of small perturbations for the MHD quantities, i.e.,

$$\begin{aligned}\mathbf{B} &= \mathbf{B}_0 + \mathbf{B}_1(\mathbf{r}, t) \\ \mathbf{v} &= \mathbf{0} + \mathbf{v}_1(\mathbf{r}, t) \\ p &= p_0 + p_1(\mathbf{r}, t) \\ \rho &= \rho_0 + \rho_1(\mathbf{r}, t).\end{aligned}$$

Here, subscripts are used to separate out the background (B_0) and perturbation (B_1) quantities. There is assumed to be no background flow and that all perturbations are much smaller than the background value (e.g., $B_0 \gg B_1$). This leads to the linearised ideal MHD equations,

$$\begin{aligned}\frac{\partial \rho_1}{\partial t} + (\mathbf{v}_1 \cdot \nabla) \rho_0 + \rho_0 (\nabla \cdot \mathbf{v}_1) &= 0, && \text{(Mass Conservation)} \\ \rho_0 \frac{\partial \mathbf{v}_1}{\partial t} &= -\nabla p_1 + \frac{1}{\mu} (\nabla \times \mathbf{B}_1) \times \mathbf{B}_0 + \rho_1 \mathbf{g}, && \text{(Equation of Motion)} \\ \frac{\partial p_1}{\partial t} + (\mathbf{v}_1 \cdot \nabla) p_0 - c_s^2 \left(\frac{\partial \rho_1}{\partial t} + (\mathbf{v}_1 \cdot \nabla) \rho_0 \right) &= 0, && \text{(Energy Equation)} \\ \frac{\partial \mathbf{B}_1}{\partial t} &= \nabla \times (\mathbf{v}_1 \times \mathbf{B}_0), && \text{(Induction Equation)} \\ \nabla \cdot \mathbf{B}_1 &= 0, && \text{(Solenoid Equation)}\end{aligned}$$

where we can define the first characteristic speed in MHD; the sound speed, $c_s^2 = \gamma p_0 / \rho_0$. There is another important characteristic speed and that is the Alfvén speed, $c_A^2 = B_0^2 / \sqrt{\rho_0}$. These equations need to then be applied to an equilibrium and, since the focus is sunspots and magnetic pores, a cylindrical flux tube is the ideal choice.

1.2.2 MHD waves in cylindrical flux tubes

To understand the observed oscillations in sunspots and pores, it is important to investigate the nature of oscillations within an idealised model of these structures. The most iconic investigation into this was undertaken by Edwin and Roberts in 1983 (Edwin and Roberts, 1983). Their analysis is based on the non-slender flux tube, where the tube radius is greater or equal to the wavelength of the oscillations. Further it ignores the effects of gravity (i.e. the stratification of the atmosphere), which is important when the wavelength is comparable to the atmospheric scale height and in the photosphere this is the case (Edwin and Roberts, 1982). It is important to note that in thin flux tubes, there are two other characteristic wave speeds. One is a subsonic, sub-Alfvénic speed, c_T (defined later on), and the other is the “mean” Alfvén speed, c_k .

The model is as follows; a cylindrical magnetic flux tube of radius a with its own density (ρ_0), pressure (p_0) and magnetic field ($B_0\hat{z}$) is embedded in a magnetic environment with a similar profile ($B_e\hat{z}$, ρ_e and p_e). The density and pressure are uniform throughout the medium. The top image of Figure 1.6 is a schematic drawing of this model.

This is the starting point for deriving the dispersion relation for MHD waves in a magnetic flux tube. It is assumed that this system is in equilibrium. Perturbations to the equilibrium conditions then add extra terms to the ideal MHD equations (i.e., the equations above). By introducing the Fourier decomposition of the perturbations, they show that the amplitude term is the Bessel equation. When bound on the axis of the cylinder ($r = 0$), two solutions exist for either the body or surface wave. In the external atmosphere, the assumption of no propagation of energy away from or towards the cylinder allows the solution for the amplitude to be found for the external atmosphere. Further, the kinetic and magnetic energy density tend to zero as $r \rightarrow \infty$. Continuity at the boundary ($r = a$) has to be kept (radial velocity component v_r , and the total pressure) which yields the dispersion relations for surface waves and body

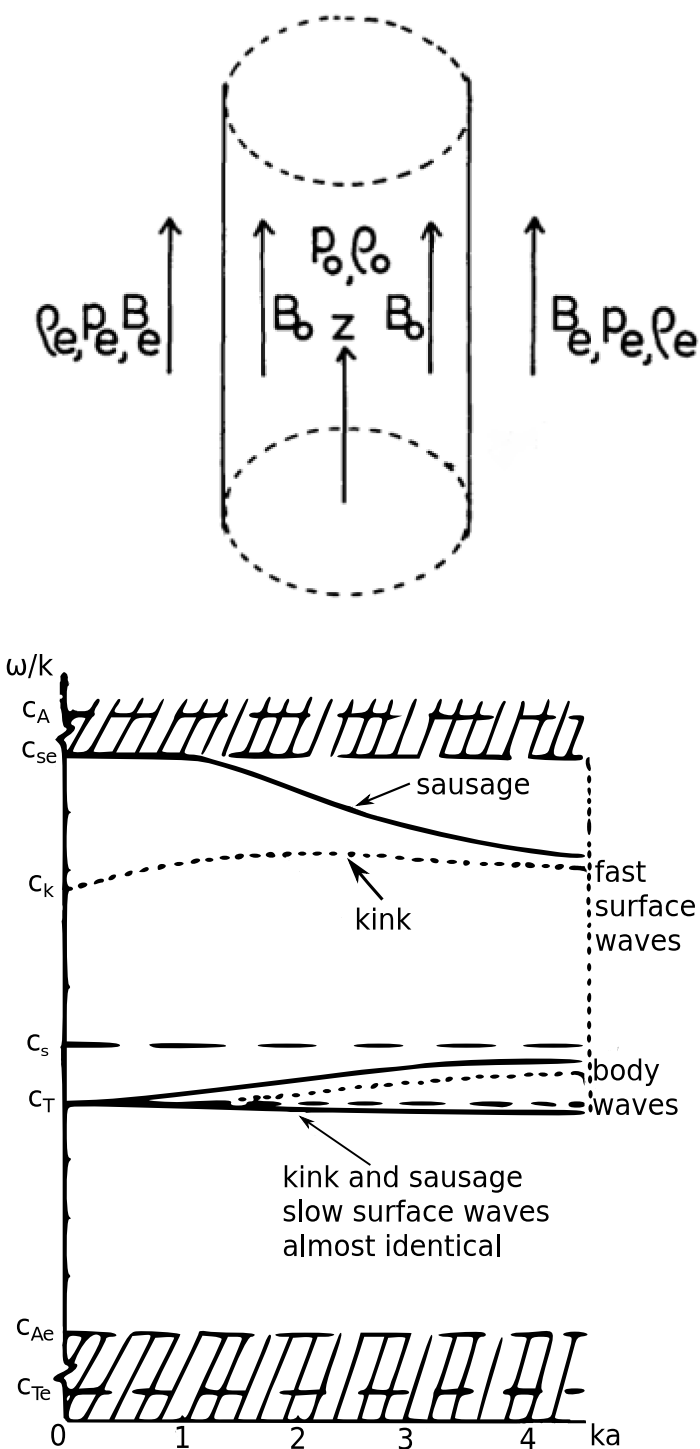


Fig. 1.6 (top) The equilibrium conditions used to model wave behaviour in a magnetic flux tube. Image is a modified version of Figure 1 from Edwin and Roberts (1983). (bottom) The dispersion relationship derived from the MHD equations under photospheric conditions ($c_A > c_{se} > c_k > c_{Ae}$). The hatched areas are the excluded values of ω and ka . Image is a modified version of Figure 2 from Edwin and Roberts (1983).

waves (Edwin and Roberts, 1983). These are,

$$\rho_0(k^2 c_A^2 - \omega) m_e \frac{K'_n(m_e a)}{K_n(m_e a)} = \rho_e(k^2 c_{Ae}^2 - \omega) m_0 \frac{I'_n(m_0 a)}{I_n(m_0 a)} \quad (\text{Surface, } m_0^2 > 0)$$

$$\rho_0(k^2 c_A^2 - \omega) m_e \frac{K'_n(m_e a)}{K_n(m_e a)} = \rho_e(k^2 c_{Ae}^2 - \omega) n_0 \frac{I'_n(n_0 a)}{I_n(n_0 a)} \quad (\text{Body, } m_0^2 = -n_0 < 0)$$

where, K_n and I_n are Bessel functions of order n , K'_n and I'_n are the derivatives of the Bessel functions, m_0 and m_e are the internal and external wavenumber, defined as,

$$\frac{(k^2 c_s^2 - \omega^2)(k^2 c_A^2 - \omega^2)}{(c_s^2 + c_A^2)(k^2 c_T^2 - \omega^2)},$$

and c_T is the tube speed,

$$c_T = \frac{c_s^2 c_A^2}{c_s^2 + c_A^2}.$$

Finally, these dispersion relations are solved under photospheric conditions and the solutions are plotted at the bottom of Figure 1.6.

These dispersion relations are important as they detail the way in which waves propagate through numerous flux tube sizes. It shows the limits of the wave solutions indicating in what regimes they cannot exist. Surface waves are dispersive as their phase speed depends on the wavenumber. There are slow body waves which are both sausage, kink and fluting modes; these modes have a phase speed between the tube and sound speeds. Slow surface waves have phase speeds close to the tube speed. There is also a surface wave with a phase speed close to the kink speed and another surface wave near the sound speed. If one can measure the phase speed of an observed wave and the ka of the flux tube, one can also likely identify the observed waves.

One factor that has been neglected is the mode number (n), its value governs the way in which the wave disturbs the flux tube. This gives us the name; sausage ($n = 0$), kink ($n = 1$) and fluting ($n > 1$). These different wave modes cause characteristic physical effects which can be used to identify each different wave mode.

Figure 1.7 shows the physical changes to the flux tube, caused by each different wave. The first diagram (a) shows how the slow wave affects the flux tube. The velocity perturbation is longitudinal. When the flux tube contracts the density decreases indicating a phase difference of π , but also the same phase difference for the cross-sectional area and intensity. The second diagram (b) shows the fast sausage mode. Here the velocity perturbations are radial, as such when the flux tube contracts the density actually increases unlike the slow sausage mode. The

cross-sectional area and intensity are in-phase, as well as the magnetic field. These diagrams have been improved over time and movies have been created which can be found within several papers (Jess et al., 2015; Morton et al., 2012) and online sources (<http://www2.warwick.ac.uk/fac/sci/physics/research/cfsa/research/wpc/vis/> or <http://swat.group.shef.ac.uk/fluxtube.html>). The main conclusion of Moreels et al. (2013) is that fast and slow modes have a different phase behaviour, namely that slow modes have an in-phase behaviour (i.e. 0 degrees phase difference between the area and the Lagrangian intensity oscillations), while fast modes have an anti-phase behaviour (i.e. 180 degrees phase difference between the area and the Lagrangian intensity oscillations). Throughout most of this Thesis we use the Lagrangian intensity variations, i.e. the intensity variations when following the motion of the plasma. Finally, the kink wave is non-compressible (to first order linear limit, long wavelength approximation) and perturbs the flux tube axis, as such, it is very difficult to measure directly unless it is possible to isolate the central axis of the flux tube, which is difficult for a sunspot or magnetic pore. This has been done for spicules and fibrils and as such, kink and Alfvén waves have been observed (see section 1.1.2.2).

While these are toy arguments and descriptions, these phase relations have been derived by several authors (Fujimura and Tsuneta, 2009; Moreels et al., 2015, 2013; Moreels and Van Doorsselaere, 2013). They have taken complex models of embedded flux tubes to derive an almost full set of phase relations for many of the MHD wave modes and whether they are standing or propagating. Table 1.1 displays the phase relations between the intensity, Doppler velocity, magnetic field and for the cross-sectional area and intensity for each wave type and whether it is a standing or propagating wave. This table will be used later on in this Thesis in order to identify the observed oscillations which occur within the numerous magnetic structures analysed. Since the focus has been on compressive perturbations, kink waves are neglected from this point onwards, as are Alfvén waves. However, see these recent review of both of these waves with regards to theory and observations (Jess et al., 2015; Mathioudakis et al., 2013). It is important to note that the focus has been exclusively on MHD sausage waves within this Thesis.

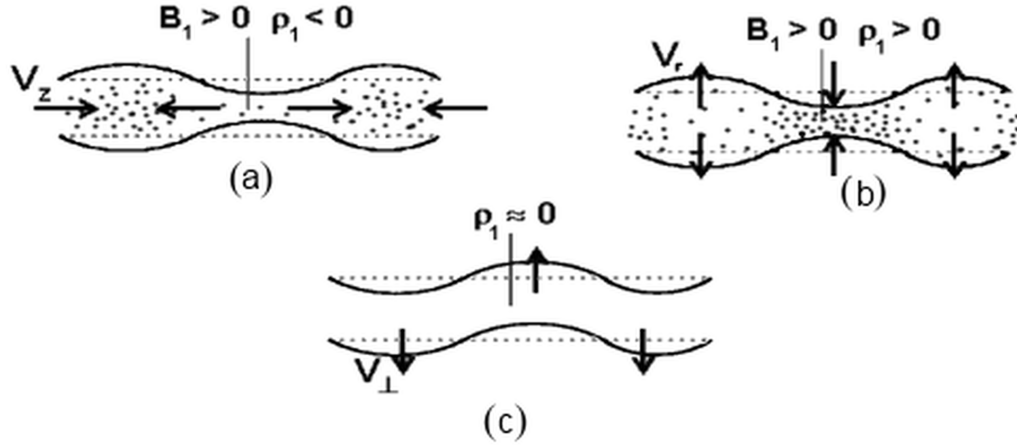


Fig. 1.7 The physical effects that each type of wave has on the flux tube. (a) The slow magneto-acoustic waves (slow sausage mode) which cause anti-phase behaviour between the intensity and the magnetic field. (b) The fast magneto-acoustic waves (fast sausage mode) which cause in-phase behaviour between the intensity and the magnetic field. (c) The fast magneto-acoustic waves (fast kink mode) which cause no magnetic field perturbations but cause $\pi/2$ phase behaviour between the intensity and velocity perturbation. Image is a modified version of Figure 1 from Wang (2004).

	$\phi_B - \phi_v$	$\phi_v - \phi_I$	$\phi_I - \phi_B$	$\phi_S - \phi_I$
Slow sausage propagating	π	0	π	0
Slow sausage standing	$\pm\pi/2$	$\pm\pi/2$	π	0
Fast sausage propagating ⁶	$[0,\pi]$	$[-\pi/2,0]$	$[-\pi/2,0]$	π
Fast sausage standing ⁶	$\pm\pi/2$	$\pm\pi/2$	$[0,\pi]$	π
Fast kink propagating	$\pm\pi/2^3$	N/A^4	N/A^4	N/A^4
Fast kink standing	$[\pi/2^1, \pi^2]$	N/A^4	N/A^4	N/A^4

Table 1.1 Shows the phase differences between three observables: the intensity, Doppler velocity and the magnetic field for each type of MHD wave and whether the wave is standing (S) or propagating (P). 1 - Wave propagating anti-parallel to the magnetic field. 2 - Wave propagating parallel to the magnetic field. 3 - Depending on the distance to the reflection boundary. 4 - Kink modes are incompressible and thus have zero intensity fluctuations. 5 - Fast sausage mode has zero LOS velocity fluctuations. 6 - Surface mode only. Collated from these authors, Fujimura and Tsuneta (2009); Moreels et al. (2015, 2013); Moreels and Van Doorsselaere (2013); Wang (2004)

Chapter 2

Data Collection and Analysis

2.1 Overview

The current solar observation scene has never been more ideal. There is near constant space-based monitoring of the Sun but also a myriad of ground-based solar telescopes in existence. This is coupled with a few small space-based telescopes and sounding rocket experiments. Further within the next decade, the largest ground-based solar telescope will open called the Daniel K. Inouye Solar Telescope (DKIST, formerly the Advanced Technology Solar Telescope, ATST) and several highly-advanced satellites will be launched (two of which will move in to very close orbits to the Sun). This is an important era for solar physics going forward.

Within this Thesis, numerous sources of solar data were used. Two telescopes will be the primary focus of this chapter: the Swedish Solar Telescope (SST) and Solar Dynamics Observatory (SDO). While other ground-based telescopes have their data utilized here, I was able to spend 10 days at the SST and thus it gets a larger focus here. These two telescopes offer some of the highest quality data available to a solar physicist. However, all data must be processed and reduced since no telescope or instrument is perfect. There are always small issues with any telescope or instrument and these can cause imaging artefacts that have to be accounted for before any analysis can begin. Once these are taken care of, the method of analysis will need to be considered and it will vary depending on the overall aims. Here, the aim was to measure two properties of the observed magnetic waveguides. These are the cross-sectional area and total intensity through time. Once these two properties have been measured, extracting any periods within these signals and the phase difference between them is required. There have been numerous methods created that aim to analyse signals and measure these properties. Within this thesis, three methods are employed which are the fast Fourier transform (FFT), Wavelet Transform (WT) and Empirical Mode Decomposition (EMD). These methods will be discussed later in this chapter once the instrumentation is detailed.

2.2 Data Sources

The work detailed within this thesis uses data from five telescopes: Swedish Solar Telescope (SST), Solar Dynamics Observatory (SDO), Dunn Solar Telescope (DST), Dutch Open Telescope (DOT) and the Swedish Solar Telescope (SVST). They are outlined below.

2.2.1 Swedish Solar Telescope

The Swedish Solar Telescope is a one metre vacuum solar telescope located at the Roque de los Muchachos Observatory on La Palma in the Canary Islands. The SST was the replacement for the Swedish Vacuum Solar Telescope which used to occupy the same site and will be talked about later in this Chapter. The SST has a 1.1 m lens, of which only 1 m is usable, which is connected to a several storey vacuum tower. The light collected travels down the vacuum tower into a corrector system and then to the optics bench. The usage of a vacuum tower means that the collected light does not pass through any air. This reduces any distortion that comes from the air being heated by the beam of light which improves image quality. The scale of the SST can be seen in Figure 2.1.

Further to this, the SST is equipped with an adaptive optics (A.O.) system. A.O. is a term used for a process that will adjust the optics of the instrument in order to reduce the effects of turbulence from the Earth's atmosphere. At a basic level, the A.O. at the SST has a sensor that monitors the wavefront of the incoming light wave and analyses how the wavefront is distorted. This distortion is counteracted by deforming a lens, by using a voltage since the lens is made of a piezoelectric material. This is not the same method used by larger and newer optical telescopes used for astrophysics that have a deformable primary mirror in conjugation with a powerful laser.

The SST has two instruments, the *CRisp Imaging SpectroPolarimeter* (CRISP) and the *TRI-Port Polarimetric Echelle-Littrow* (TRIPPEL). TRIPPEL is a spectrograph with a constant diffraction grating spacing but has a shape that is similar to a sawtooth-shaped step function. See Kiselman et al. (2011) for a full overview of this instrument.

CRISP is a tunable dual Fabry-Perot filter system. The wavelength range is in the red wing (510-860 nm) and the light firstly goes through a selectable filter dependent on the aims of the observation objectives. This allows many wavelengths to be chosen with one instrument, which is required in order to observe the large height variance of the solar atmosphere. The Fabry-Perot is made from a pair of partly reflective mirrors that are separated by a small distance. By varying the distance between the two mirrors, a specific wavelength can escape the mirror system and go to the cameras. With the ability to vary the distance between the mirrors, the Fabry-Perot system is able to investigate the line profile, of many elements. Table 2.1 has approximately a third of the available wavelengths on CRISP. The selection here is the more commonly used wavelengths that often appear in published papers.

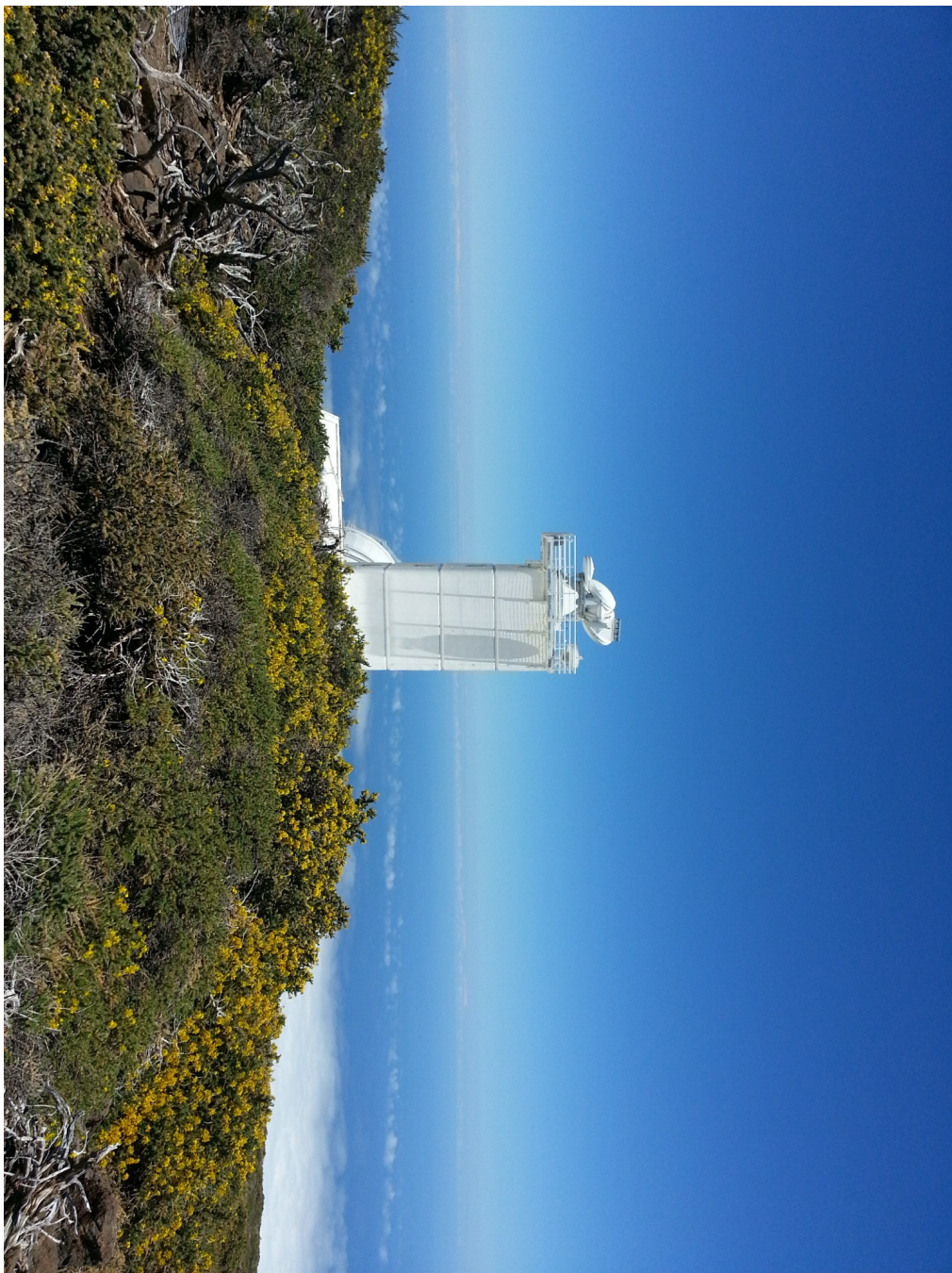


Fig. 2.1 An image of the Swedish Solar Telescope taken from a ledge near the caldera on the island of La Palma that is part of the Canary Islands. The Primary mirror housing can be seen at the top of the image, while the tower that conceals the vacuum tower can be seen beneath it. Copyright goes to the author.

Pre-filter	Wavelength (nm)	FWHM (nm)	Line Core Height (km)
Mg b	517.33	.3	≤ 1000
Na D	589.7	.38	≤ 500
Fe I	630.26	.44	≤ 250
Ca II k	854.16	.93	≤ 1300
H α	656.2	.49	≤ 1500

Table 2.1 Summary of the more commonly used wavelengths that are observable with CRISP. Each filter has a name, wavelength at the line-core and the Full Width at Half Maximum (FWHM) and an average formation height of the line-core, which are soured from Jess et al. (2010).

Further to this, the light beam at the SST is spilt into two parts when CRISP is in use. The red wing goes to CRISP, while the blue part goes to a series of broad band cameras. These wavelengths are G-band and Ca K which sample the photosphere. These do offer some of the highest resolution images of the solar photosphere to date and are only used when the seeing is excellent.

An important wavelength is 656.3nm and is commonly referred to as H α . It is when an electron drops energy level from the third shell to the second in a Hydrogen atom. This transition is the easiest method to observe the chromosphere and occurs approximately 1.5 Mm from the base of the photosphere. Understanding the chromosphere has become a topic of heavy interest as the “coronal heating problem” shifted from the corona to the chromosphere over the past decade (Aschwanden et al., 2007). Since the line core of H α samples the chromosphere, understanding how this line is formed within the solar atmosphere has become a very important topic.

However, H α line formation is a difficult topic. The line is highly complex, most likely it is dependant on numerous physical effects such as ionization or non-LTE effects. Currently, the standard understanding of H α comes from radiative MHD simulations, for example by Leenaarts et al. (2007) or Leenaarts et al. (2012). From these sources, we can summarize a few properties and observations of the H α line core.

Current research suggests that structures that appear darker, such as fibrils, in the line-core are formed higher compared to other features. Further, the opacity of H α that is formed in the upper chromosphere is temperature insensitive. This means that the opacity of the line is mainly determined by the mass density at these regions.

The results suggest that fibrils are mainly located within magnetically dominated (i.e., low plasma-beta) regions between photospheric field concentrations of opposite polarity. These fibrils are aligned with the local magnetic field direction. Further, fibrils are located in regions where the local density is larger compared to the

background chromosphere. This effects the average formation height for H α by making it higher and thus the intensity is lower. So, fibrils can be used to trace out regions of enhanced chromospheric mass density.

2.2.2 Solar Dynamics Observatory

Solar Dynamics Observatory (SDO) is one of the latest space-based telescopes launched by National Aeronautics and Space Administration (NASA) (Lemen et al., 2012). It can be considered as the replacement for the Solar and Heliospheric Observatory (SOHO) (Domingo et al., 1995) and the Transition Region and Coronal Explorer (TRACE) (Strong et al., 1994). Since 2010, it has been observing the Sun constantly, beaming large quantities of data back to Earth. Without Earth's atmosphere in the way, it offers some of the clearest observations of the entire Sun to date. The spacecraft houses three instruments: the *Extreme Ultraviolet Variability Experiment* (EVE) (Woods et al., 2012), the *Helioseismic and Magnetic Imager* (HMI) (Schou et al., 2012) and the *Atmospheric Imaging Assembly* (AIA) (Lemen et al., 2012).

EVE is designed to measure a wide range of extreme ultraviolet spectral lines with a Sun-as-a-Star method. HMI measures LOS velocities as well as the LOS and vector magnetic field of the photosphere. AIA is a multi-wavelength instrument and is able to take images of the solar surface to the outer reaches of the solar atmosphere. This has offered an unprecedented view of the many layers of the solar atmosphere at the same time. This view can be seen in Figure 2.2, which shows the full wavelength range of AIA as well as an HMI image. The figure showcases almost every wavelength that can be observed using AIA, from the low temperature lines such as 170 nm to the hotter lines that reveal the corona like 13.1 nm. Further, there is a LOS magnetogram from HMI.

2.2.3 Other Ground Telescopes

Data from three other ground-based telescopes are used within this thesis. This is a brief summary and more detail is given within the chapters where the data from these telescopes and instruments are used.

Firstly, the Swedish Vacuum Solar Telescope (SVST) which was the predecessor to the current SST. It had a 47.5 cm mirror with several wavelength narrow band filters with no A.O. The narrow band filters were not too dissimilar to the wavelengths in Table. 2.1. See Scharmer and Lofdahl (1991) for a full overview of the SVST.

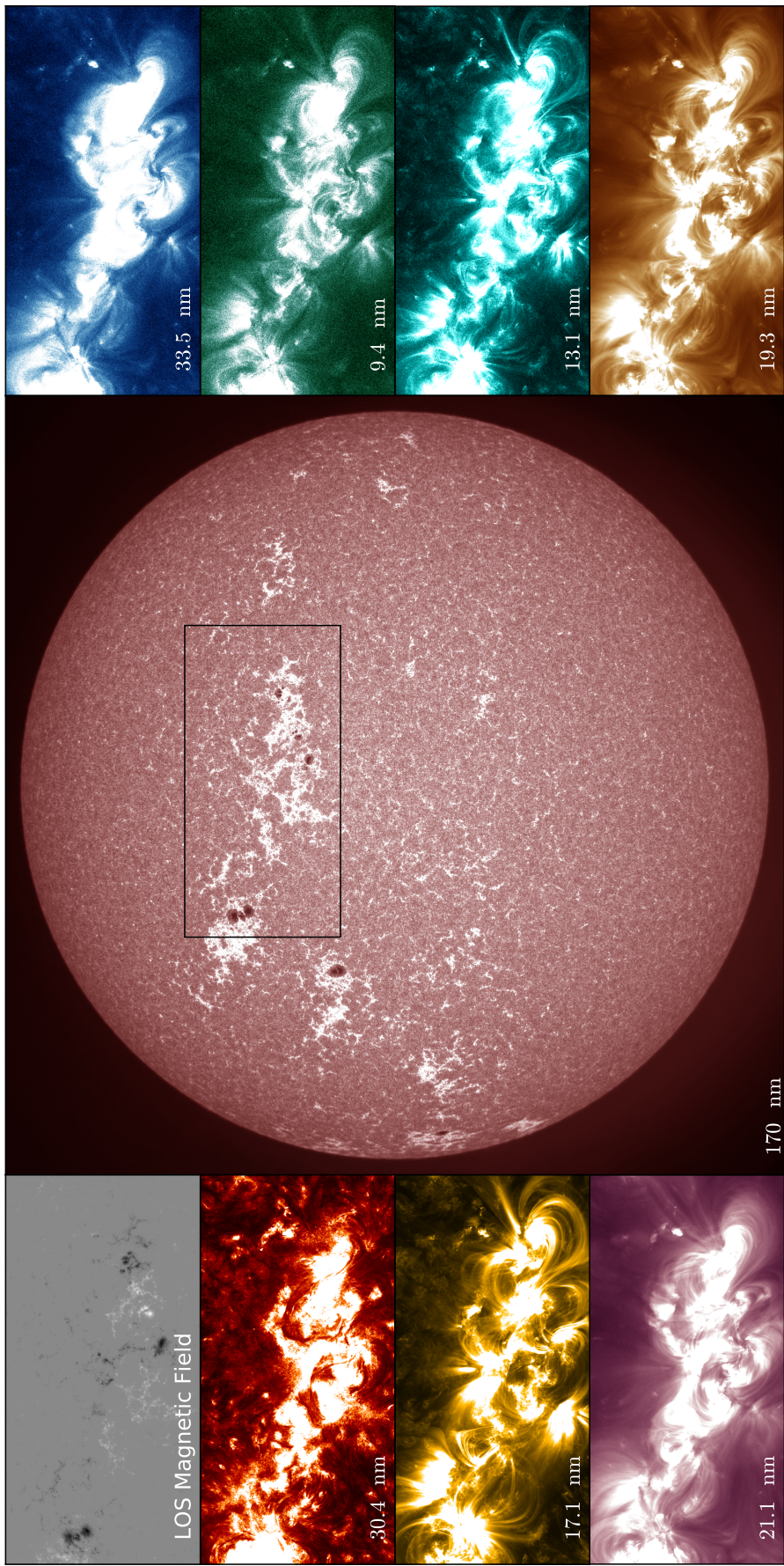


Fig. 2.2 The field of view of the Solar Dynamics Observatory (SDO). Each image shows a different wavelength that is captured by two of the instruments on SDO, the Atmospheric Imaging Assembly (AIA) and Helioseismic and Magnetic Imager (HMI). The images are taken on the 17th of April 2015 focusing on AR 12326. The columns on the side go downwards in increasing temperature response. The 160 nm and 450 nm filter of AIA is missing from the image.

Secondly, the Dutch Open Telescope (DOT) is an open-air solar telescope that is retired. The DOT is located next to the SST on La Palma. It had a very compact design that is quite different to the SST. It had a mirror that is slightly smaller than the previous SVST, at only 45 cm. The full instrumental setup consisted of 6 cameras each with a different narrow band filter. With no A.O., it used a more unconventional method to lessen seeing effects. The telescope was on a mount several meters high, which was open to the atmosphere. As such, the strong winds blew across the mirror reducing seeing effects from temperature gradients that are caused by the ground, which reduced image distortion. Further, it used high frequency cameras that allowed speckle reconstruction. See Rutten et al. (2004) for a full overview of the DOT.

Finally, the Richard B. Dunn Solar Telescope, located at Sacramento Peak in New Mexico and is run by the National Solar Observatory (NSO). It has a 76 cm mirror and is a vacuum telescope similar to the SST but its design is unique. It has several instruments but the focus here is on two of them: *Rapid Oscillations in the Solar Atmosphere* (ROSA) and *Interferometric Bidimensional Spectrometer* (IBIS). ROSA is a synchronised 6 camera system similar in principle to the system on the DOT. It captures images at high frequency rates and uses narrow band wavelength filters that sample the photosphere and chromosphere. Much like the DOT, it uses speckle reconstruction to improve the quality of the images, while IBIS is similar to CRISP at the SST. It consists of two Fabry-Perot interferometers that operates in the red wing (550-860 nm) and allows in-depth line scans for specific wavelengths as well as measuring polarized light in spectropolarimetric mode. See Jess et al. (2010) and Cavallini (2006) for a full overview of ROSA and IBIS respectively.

2.3 Data Analysis

Once the process of data acquisition is finished and the reduction is undertaken using methods that are specific for that telescope/instrument, analysis of the data can begin. The method used will vary depending on the overall science goal or aim. For example, statistical studies require crunching through large quantities of data in order to categorize the general properties of the phenomenon that is under investigation. Other studies will focus on single events, either due to the lack of a large selection of data or if the event under investigation is rare. The analysis undertaken within this thesis is focused on measuring properties of waves in several sunspots and magnetic pores as well as a single RPW event.

From Chapter 1, to observe MHD sausage waves in cylindrical structures, the phase relations between specific observational quantities such as cross-sectional area

and total intensity are required. While further phase relations are available, the two quantities used were the ones only possible with the ground-based data available at the time, so the focus has been on the cross-sectional area and total intensity perturbations. Once these signals have been extracted from the datasets used, the periods and phase of these signals must be found. The method used to extract these signals will be detailed below. Finally, signal analysis is required to calculate the periods within the obtained signals as well as the phase difference between these two signals. The methods used are the Fast Fourier Transform (FFT), wavelets and Empirical Mode Decomposition (EMD) and are discussed now.

2.3.1 FFT

The first method is the Fast Fourier Transform (FFT). Its name is a reference to the fact that the FFT is very fast computational algorithm of the Discrete Fourier Transform (DFT). It was first introduced by Cooley and Tukey (1965). The Fourier Transform is a mathematical method to decompose a signal which is assumed to be periodic into its constituent frequencies. Generally, it is common to have a real-valued signal input into the FFT and the output is a complex number. The absolute value of this output is the amount (or power if squared) of each frequency in the original signal and the complex part is the phase shift of the sinusoidal function at that frequency.

An example of this can be seen in Figure 2.3. The top left image is of an artificial signal, of the form,

$$\sin\left(2\pi\frac{x}{5}\right) + \cos\left(2\pi\frac{x}{10}\right) + 5 \times \text{random noise}$$

with the noise that is Gaussian distributed. The top right image is the output after this signal is passed into the FFT. It is a frequency spectrum, where we have power as a function of frequency. The largest two peaks that can be seen correspond to the frequencies of the artificial signal. The small peaks will correspond to the noise that was added to the signal.

All signal analysis methods have downsides. Firstly, the input signal having a finite length introduces artefacts, however, this is not unique to the FFT and all signal analysis algorithms suffer from this issue. The FFT has an effect known as frequency leakage. It is where, if the input signal is non-periodic or the input signal has no closed form transform, there is smearing in the frequency spectrum. This means that the power is not confined to the correct frequency and spreads, so other frequencies close to the strongest frequencies will be masked if the difference in power between

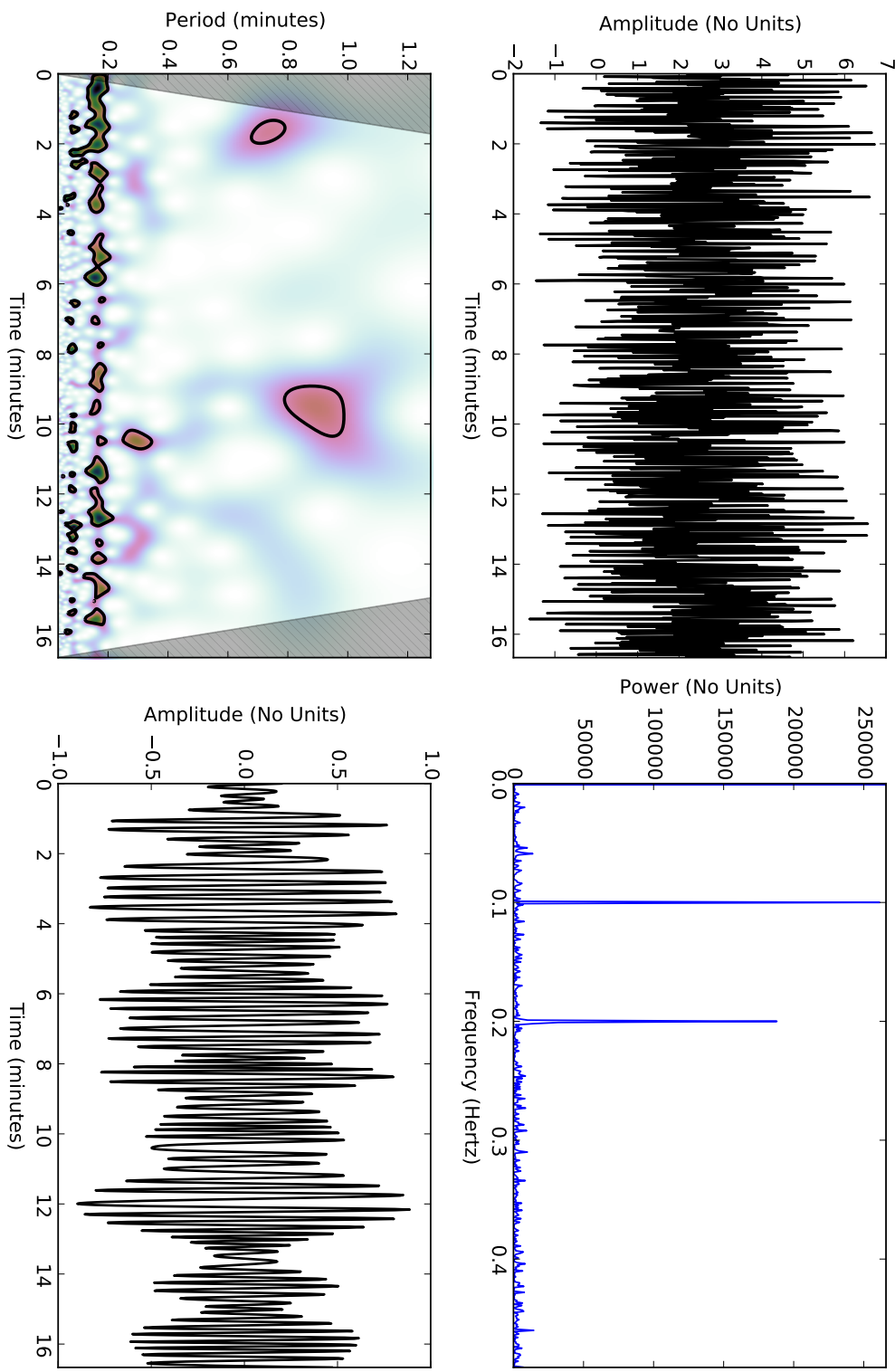


Fig. 2.3 An example of signal analysis of the three main methods used in this thesis. The upper left plot is of an artificial signal with noise. The upper right plot is a frequency spectrum from the FFT. The largest two peaks shows the frequencies within the artificial signal. The bottom left plot is a wavelet power spectrum. It expands on the FFT by offering a 2D view of the frequency spectrum with time. So it is possible to see what period is within the signal but also at what time it occurred at and for how long. The bottom right plot shows an IMF output from a EMD algorithm. The IMF shows one of the periods from the artificial signal used. This plot shows the first frequency of the artificial signal.

two frequencies is large. This can be overcome by using a window function on the original signal which alters the outcome of the FFT in order to reduce these effects. Finally, another important part of the FFT is the output can be reversed. It is possible to recover the original signal using the Inverse FFT (IFFT). This fact means that one can create a frequency window and apply it to the frequency spectrum. This can be used to filter parts of the frequency spectrum that contain information that is unnecessary or return a new signal to see the behaviour at specific frequencies. It is commonly used method in signal analysis and is used within Chapter 5.

2.3.2 Wavelet Transform

The second method employed is called the Wavelet Transform. A wavelet is a function that is constrained in time and frequency space i.e., localised within these specific domains. The base function used is called the mother wavelet and variations of this function are called daughters. This factor is important, as the FFT will, when given a 1D signal, output a 1D frequency spectrum. The wavelet algorithm will return a 2D spectrum where the extra dimension is time. This means you can also know what frequency is within the signal but also at what time in the signal that frequency exists and for how long. This is a more powerful method due to this fact, but also, each mother wavelet have different properties, so depending on the goal of the signal analysis, by changing the mother wavelet, different information can be extracted. For example, the wavelet chosen within this thesis is the Morlet Wavelet. It is defined as,

$$\Psi_0(\eta) = \pi^{-1/4} \exp(iw_0\eta) \exp(-\eta^2/2). \quad (2.1)$$

which can be summarized as a plane wave modulated by a Gaussian. It has good frequency resolution but it comes at a cost of its time resolution, while another wavelet called the Paul wavelet has a poorer frequency resolution but it has an increased time resolution. This allows the method to be highly variable.

The top right image of Figure 2.3 shows the output of a wavelet algorithm on the artificial signal. The dark regions show an increase in the power, which shows where the periods of the signal are. The wavelet algorithm has the ability to calculate the significance of any regions of power and the black contour lines show this. The contour lines shown are for 95% significance. Further, much like the FFT, the finite length of a signal creates edge effects for the wavelet. This can be seen as the cross-hatched regions, these mark the region where the finite length of the signal affects the wavelet transform. The hatching properties are different for each mother wavelet.

Finally, the wavelet transform allows for direct comparison of two signals. It is possible to calculate the cross-wavelet of two signals as well as correlation and the phase difference using the wavelet transform. This fact allows the wavelet transform to be used to measure the phase difference of the cross-sectional area and total intensity signals, which is the main method used to find the phase difference within this thesis. See Christopoulou et al. (2003) for an overview of the wavelet transform and its applications.

2.3.3 Empirical Mode Decomposition

Finally, we have Empirical Mode Decomposition (EMD). As the name suggests, this method is not based off a mathematical theorem or transformation. The algorithm will output several signals, the residual and Intrinsic Mode Functions (IMFs). The residual is the left over signal from the algorithm and tends to contain any slow varying background trend. An IMF will generally be a simple oscillatory mode, ideally it should be only one of the frequencies within the original signal. There are two requirements in order to be considered as an IMF. Firstly, the number of extrema and zero crossings must either be equal or differ by one. Secondly, the mean value of the envelope defined by the local maxima and the envelope defined by the local minima equals zero.

The steps of the algorithm are as follows.

1. The minima and maxima of the input signal are found.
2. A spline fit of the minima and maxima points is computed.
3. The resulting minima and maxima curves create an envelope that encompasses the signal.
4. This envelope is subtracted from the input signal and this process is repeated again until a specific criterion is met. This is termed sifting.
5. The resulting signal is called an IMF and is subtracted from the original signal. The leftover signal is termed the residual.
6. This process repeats itself again on the residual signal until a set number of IMFs are obtained leaving nothing but the final residual signal.

There are two comments to be made here. Firstly, the stopping criterion for the sifting varies and there are two common ones. The first one is, if the standard deviation of the sifted signals is lower than a given limit, the process stops. The second one

is called the S number which, if the same signal is returned by the sifting process more than S times, causes the process to stop. Secondly, the overall algorithm has no method of deciding when enough IMFs have been found, so the number picked is arbitrary, but generally the algorithm will stop before this limit is reached. As the residual becomes linear with each IMF removal, the fitting algorithm will stop naturally since there are no more extrema points. The resulting set of IMFs, contain the periods within the original signal, while the residual should contain any background trend. Much like the FFT, you can reverse the method as the sum of all of the IMFs and residual will return the original input signal.

The EMD allows, much like the cross wavelet, the ability to find the phase difference between two signals containing the same periods. With a direct comparison of the IMFs of one signal to another, you can measure the phase difference between them. For example, this was carried out by Morton et al. (2011). The EMD algorithm is also very good at separating noise from a signal, which is what the first IMF generally contains.

The drawbacks for the EMD are most focused on the method, since it has no mathematical foundation like the FFT or wavelet. The most important issue for the EMD is the spline fit that creates the envelopes. The envelope fit with each iteration, starts to become very large at the edges since there is nothing to constrain it. As such, when these are subtracted from the signal, the resulting IMFs display large swings at the start and end, so these edge effects will easily affect the output. To counter-act this effect, several methods have been suggested to lessen this issue and it will generally involve adding extra extrema points on both sides to constrict the spline fit. See Huang et al. (1998) or Terradas et al. (2004) for an overview of this method.

2.4 Area Analysis

The core work presented in this thesis is analysing the cross-sectional area of magnetic pores and sunspots. So it is important to be able to confidently measure the cross-sectional area. The base idea is to contour the structure and use that as a measure of its cross-sectional area. The issue is how various methods have been used in published research. While many never state exactly how they contoured a sunspot or a magnetic pore. Morton et al. (2011) used a 2.5σ threshold of the mean background intensity for G-band data. Sigma (or σ) refers to the standard deviation of the background intensity. More recently, Grant et al. (2015) used 2.2σ of the mean background intensity for their data. This was to account for the change in

contrast between several different wavelength filters. Since their aim was to measure the cross-sectional area of a pore from the photosphere to the lower chromosphere.

What will occur here, is an analysis on what effect changing the value of sigma has on the resultant cross-sectional area signal. The value of sigma can appear to be arbitrary and there is an assumption that the intensity of the background photosphere is a normal distribution and as such sigma can be used to contour these magnetic structures. To be more precise, whether different sigma values will give different periods after signal analysis or if the value of sigma once set within a certain range does not change the output is of interest, especially since the current selection of ground-based solar telescopes have resolutions similar to each other and this could be the limiting factor in detecting these oscillations.

This analysis is only for ground-based data and for elemental lines that sample the photosphere directly. The chromosphere lines used traditionally (Ca II and H α line core) make resolving the fine boundaries of a sunspot or a magnetic pore very difficult. This is an area for future investigation.

2.4.1 Data Source

The data for this investigation comes from two instruments on the DST: IBIS and ROSA.

The IBIS dataset consists of an image series of a H α line scan. The DST was centred on a sunspot in AR 11579. The observation run was on the 30th of September 2012 at 15:00 UT until 15:16 UT with a cadence of 6.8 seconds. The full field of view (FOV) was 96'' by 96'' with a pixel size of 0.097''. The part of the line scan used here is -0.7 nm, which falls into the blue wing of the H α line profile. This part of the line profile samples the photosphere strongly and will show Ellerman Bombs as well as Type II spicules. See Nelson and Doyle (2013) on the reduction methods for this IBIS data.

The ROSA dataset consists of an image series of G-band narrowband filter images. The DST was centred on a small magnetic pore cluster in AR 11683. The observation run was on the 6th of March 2013 at 19:27 UT till 20:02 UT with a cadence of 2.11 seconds. The full FOV was 115'' by 115'' with a pixel size of 0.12''. The narrow band filter means that only the line core was sampled and this corresponds to the low photosphere for G-band. See Grant et al. (2015) for the reduction methods for this ROSA data.

Both magnetic structures can be seen in Figure 2.4. The image on the left showcases the IBIS sunspot while on the right, the ROSA pore is displayed. Both images are context images and do not show the full FOV of each instrument during that

observation run. Both structures are stable throughout their respective observation run.

The method used to contour these structures is as follows. The starting point is to find a large area of quiet-Sun photosphere, where there is no strong magnetic features. This area is used to calculate the mean intensity and a histogram of this area should form an approximate normal distribution. The normal distribution means that the standard deviation (σ) can be used to select specific pixels within the image. As the number of standard deviations is increased, more of the data will be covered by the distribution; By limiting the pixels of interest by having a limit that is lower than say two standard deviations or higher, the pixels left over will be the darkest 5% of pixels, or the other way round would return the brightest 5% of pixels. Theoretically, the lower limit should return the pixels for sunspots and magnetic pores which are substantially darker than other features in the photosphere. By counting these pixels, this should correspond to the cross-sectional area of these magnetic structures.

Figure 2.5 shows this method applied on the example datasets. The left column shows the two context images of these datasets shown in Figure 2.4. However, added to these images are four contours coloured as follows: blue, green, purple and orange. Each colour represents a different multiplier for the standard deviation. The sunspot and magnetic pore do not share the same range of multipliers. For the sunspot the multipliers are 3, 3.5, 4, 4.5 and for the pore they are 2, 2.5, 3, 3.5.

Firstly, the sunspot observed with IBIS will be investigated. The contouring for the sunspot at the lower sigma multipliers does capture small parts of the penumbra. For example at 2.5σ (which is not shown), the contour was the entire sunspot, i.e., the umbra and penumbra. The jump to 3σ (blue) curtails most of the penumbra. Once sigma is at 3.5 and 4, which correspond to the green and purple contours, the penumbra that is contoured has shrunk nearly to zero. However, it is not until we reach the largest sigma value (4.5) that the penumbral area disappears completely. The reason for this can be seen in the right column of Figure 2.5. The top figure is of a histogram of both the background which is in yellow and the context image on the left which is in red. The background here is not in a normal distribution and the reason for this is that the full FOV does not have a good area of quiet-Sun photosphere. The wings of H α show a variety of features, including Ellerman Bombs and Type II spicules, so finding an isolated region becomes harder. Further, the full FOV is more limited in IBIS than ROSA or CRISP. This means that the sigma value is skewed and thus the multiplier will have to be higher to counter act this. Finally, the sunspot histogram shows a clear difference between the penumbra and umbra. The histogram can be split into two parts, the left part contains the umbra and the

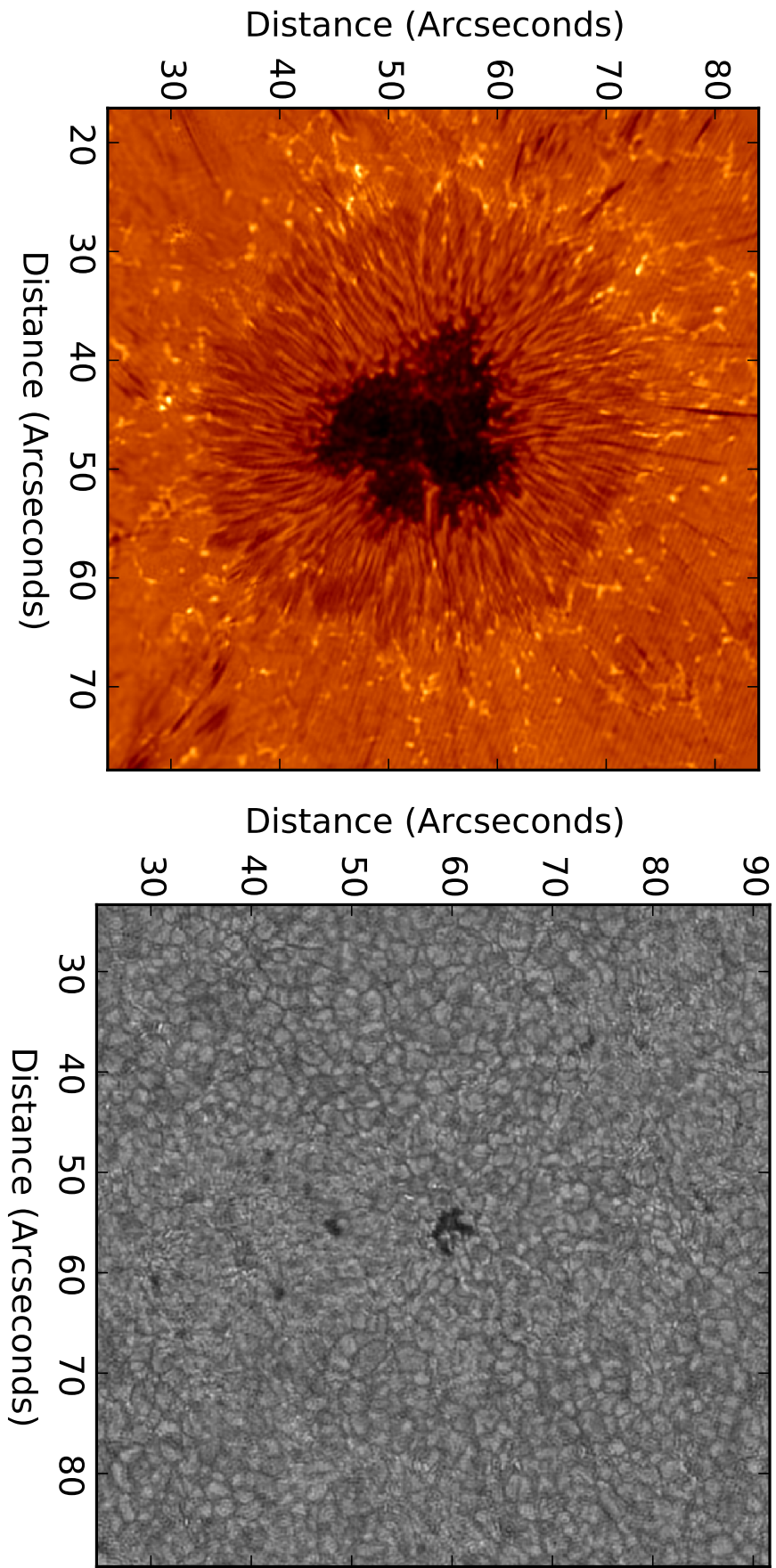


Fig. 2.4 The left figure is the cropped field of view (FOV) for IBIS. It is in the blue wing of the $H\alpha$ line profile which samples the photosphere and not the chromosphere that the line core samples. The sunspot is in AR 11579 and was taken on the 30th of September 2012 at 15:00 UT until 15:16 UT. The right figure is of a cropped FOV for ROSA. It is the G-band narrow band filter which samples the lower photosphere. The focus is on a small magnetic pore cluster, in AR 11683 and was taken on the 6th of March 2013 at 19:27 UT till 20:02 UT. The magnetic pore investigated here is the larger one at the top.

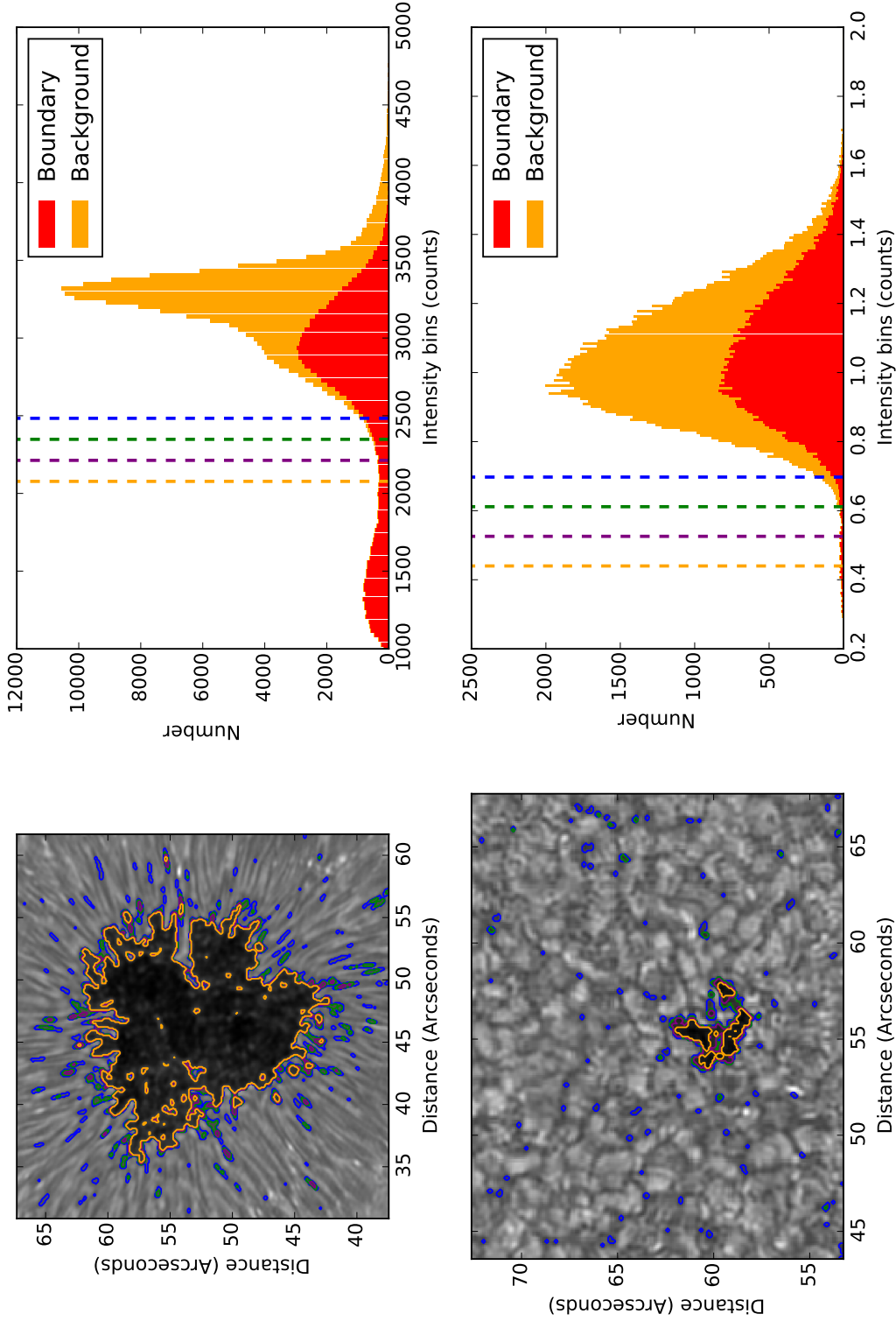


Fig. 2.5 An overview of the method used to contour the magnetic structures in this thesis. The left column shows context images of the datasets shown in Figure 2.4. They have the contours of the various sigma multipliers shown. The contour colours of blue, green, purple and orange correspond to 3 , 3.5 , 4 and 4.5σ and 2 , 2.5 , 3 and 3.5σ for the sunspot and magnetic pore respectively. The right column shows histograms of the background photosphere in yellow and of the context image of the magnetic structures shown on the left in red. The vertical lines shown display where the σ values end up on the histogram. These are coloured in the same vein as the left column contours.

right part contains the penumbra. The penumbra for this sunspot occupies a larger portion of the context image which explains why the right part of the histogram is taller. At the intensity values between 1800 to 2300, the histogram plateaus and within this region is where the range of sigma multipliers lie. The vertical coloured lines correspond to the same colour contour lines in the context image. It is possible to claim that, as long as the sigma multiplier is between this range, we have isolated the penumbra from the umbra. Using this as guide, it makes it easy to show that the sigma multiplier of 4.5 would be an ideal value since it gives the values in the middle of the plateau.

Secondly, the magnetic pore observed with ROSA will be investigated. The overall picture is quite different and the main reason for this is the lack of a penumbra. While there was a plateau that separated the penumbra and umbra for the sunspot, this is missing for the magnetic pore and the sigma multiplier is harder to directly choose. The sigma multipliers are lower for the magnetic pore and are 2, 2.5, 3 and 3.5. Each of these are shown on the bottom left image of Figure 2.5. These values again correspond to blue, green, purple and orange. The lowest multiplier contours large amounts of the background photosphere. However, all the larger multipliers contour only the magnetic pore. There are clear parts of the magnetic pore that are ignored with these higher multipliers. By looking at the histogram, a different picture emerges when compared to the sunspot. Since the magnetic pore is very small, the behaviour of the previous histogram for the sunspot does not emerge. There is no clear separation between the background and the magnetic pore, so picking a direct sigma value is more difficult when using the histogram. The background histogram also has a normal distribution unlike the previous example. The lower limit (the blue vertical line) shows that at this value, there is still large amounts of the background quiet-Sun. But, as the limit is increased, that amount drops to near zero and as such, we have very little quiet-Sun within the cross-sectional area contour. Here, instead of a plateau, the histogram reveals that there is a tail. This tail corresponds to the pixel values that correspond to the magnetic pore. For a magnetic pore, this tail can be used to pick a sigma multiplier since it tails off to much lower values than the quiet-Sun histogram. The start of this tail is around 2.5σ and this gives a very good contour of the magnetic pore. That is why taking values of the threshold above 2.5σ cuts off pixels that are clearly part of the magnetic pore. The different sigma multipliers used for the sunspot and magnetic pore are most likely due to the lack of a good background region for the sunspot in IBIS. A direct comparison of intensity counts for a sunspot and magnetic pore is difficult since the ROSA pipeline normalizes the intensity counts.

Finally, it is important to see whether these different sigma multipliers give different periods within the resultant cross-sectional area signals. Figure 2.6 and 2.7 show the wavelet transform of the signals that correspond to the smallest and largest sigma multipliers used for the sunspot (3 and 4.5) and magnetic pore (2 and 3.5). The top row show the cross-sectional signals of these sigma multipliers and the bottom row is the resultant wavelet transforms.

The IBIS sunspot shows little change between the sigma multipliers. Since the range of sigma multipliers correspond to the plateau region, the returned cross-sectional area does not catch the penumbra, so the signal that corresponds to either one is focused heavily on the umbra and detects the periods found in the umbra. Thus, for this range of sigma multipliers, the same periods are found within this dataset. The short length of this data series means that it is impossible to find larger period oscillations, so the only periods found in this sunspot are 1 and 2 minute oscillations.

Now, for the magnetic pore observed in ROSA and with a longer signal. The most obvious difference here is the variation of power at periods that are 3 minutes and less for the lower sigma multiplier i.e., 2. This power has basically disappeared for the larger multiplier (3.5) but still lingers on. The other difference is minor, but it is for the larger periods seen at 5 and 9 minutes. While they are under the cone of influence, they are seen clearer and are more powerful for the smaller sigma multiplier. However, both multipliers still have the same oscillation periods regardless. The cause of this difference would be that the larger multiplier under samples the magnetic pore and this has caused a large difference as expected. However, this reveals that the difference here is still small, it would matter most if the wavelet power was used to measure the amplitude of these oscillations. Overall, the conclusion for this analysis is that the value of sigma will not vary the result as long as the range of sigma multipliers is sane.

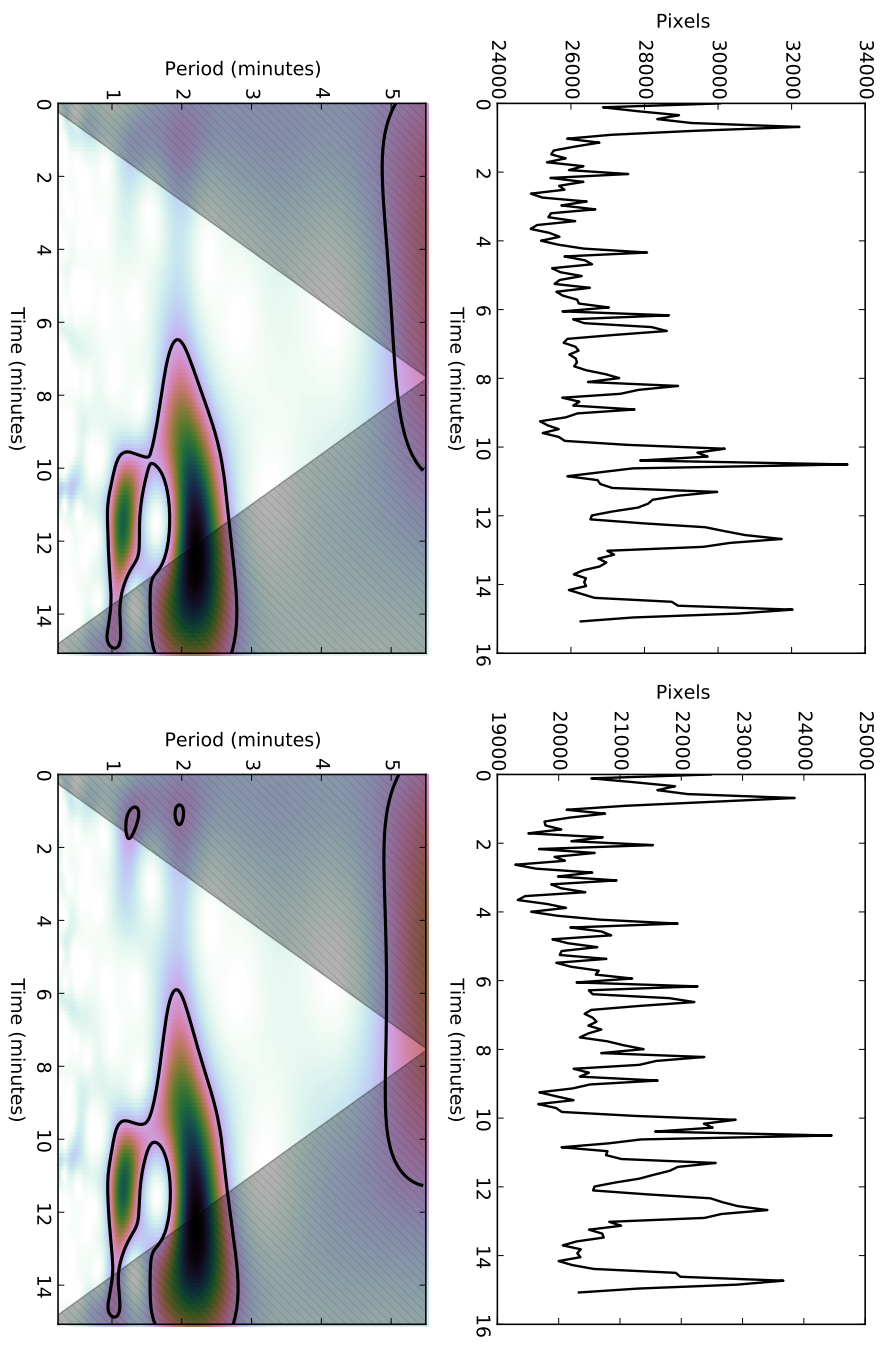


Fig. 2.6 The top row shows the cross-sectional area signals returned from a sigma multiplier of 3 and 4.5 for the sunspot observed in IBIS. These correspond to the blue and orange contours in Figure 2.5. The bottom row shows the resultant wavelet transforms of these two signals. The cross-hatch region is the cone of influence, while the black contour line is the 95% significance level. The returned wavelet transforms images show that for the IBIS sunspot, the different in sigma multipliers causes no difference in the detected area oscillations.

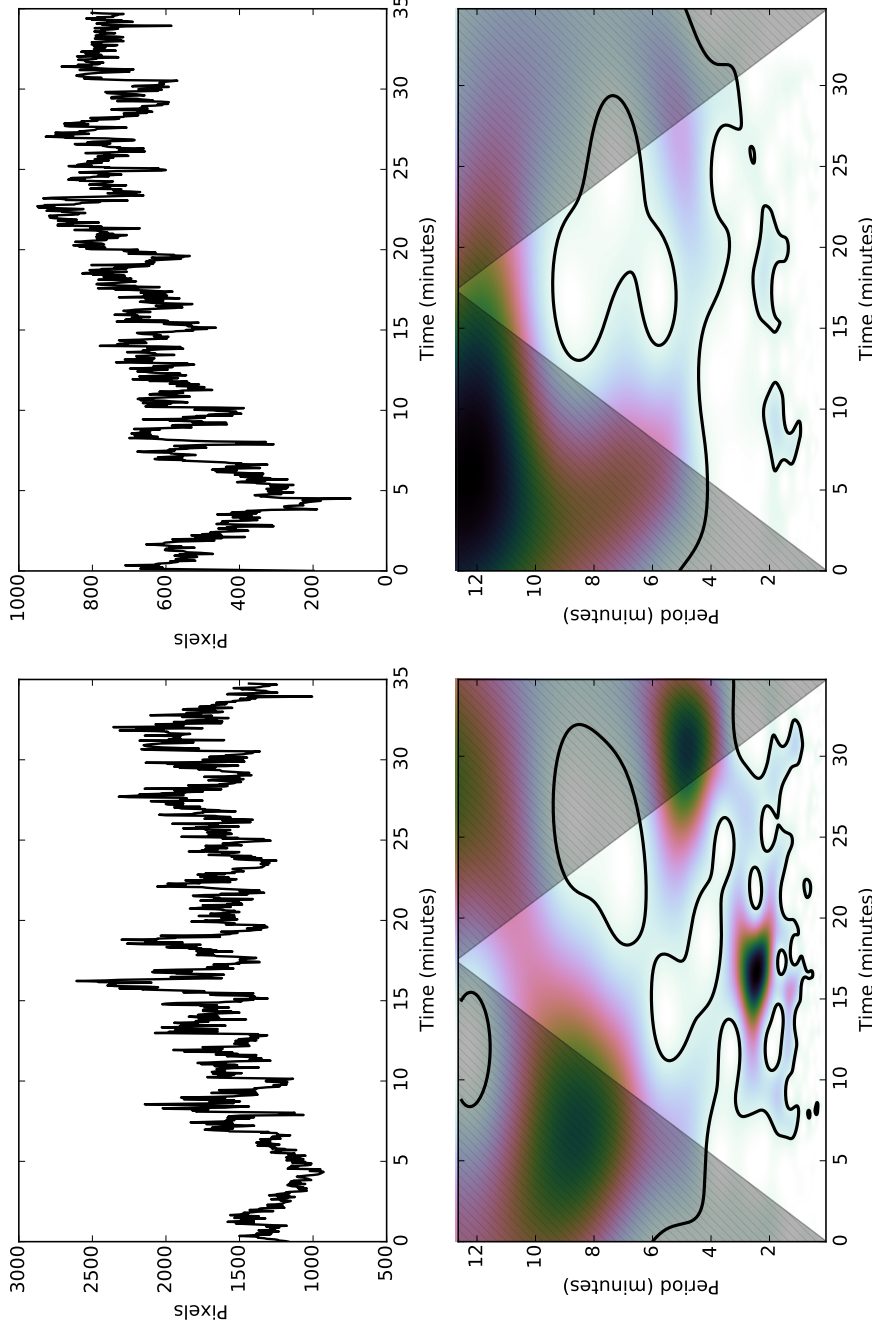


Fig. 2.7 Same as Figure 2.6 but for the magnetic pore observed in ROSA. The lowest sigma multiplier is 2 and the largest is 3.5. These correspond to the blue and orange contours in Figure 2.5. Unlike the sunspot, there is a clear difference between the different sigma multipliers. The periods at 2 and 3 minutes are not shown in the largest case and this showcases that for smaller magnetic structures, the sigma multiplier is very important.

Chapter 3

Analysis of Area Oscillations¹

¹This chapter is based on Dorotovič, I., Erdélyi, R., Freij, N., Karlovský, V., and Márquez, I. (2014). Standing sausage waves in photospheric magnetic waveguides. *Astronomy & Astrophysics*, 563. Reproduced with permission from Astronomy & Astrophysics, © ESO

3.1 Overview

The commonly studied oscillatory periods in sunspots are three and five minutes. These oscillations are seen in intensity, line-of-sight (LOS) velocity, and LOS magnetic field.

The MHD sausage modes are of interest here, because the sausage mode is a compressible, symmetric perturbation around the axis of a flux tube that causes density perturbations that can be identified in intensity images (Fujimura and Tsuneta, 2009). Furthermore, because the wave will either compress or expand the flux tube, the magnetic field will also show signs of oscillations. This mode may come in two forms in terms of phase speed classification: a slow mode (often also called the longitudinal mode), which generally has a phase speed close to the characteristic tube speed; and fast mode, which has a phase speed close to the external sound speed. A main difference between the two modes is the phase relationship between appropriate MHD quantities, which allows them to be identified. In this case, the fast sausage mode has an out-of-phase relationship between the area and intensity, while the slow sausage mode has an in-phase relationship. The technique that was applied to obtaining these phase relationships are covered by, say Fujimura and Tsuneta (2009), Moreels and Van Doorsselaere (2013), and Moreels et al. (2013).

Sausage modes have been observed in solar pores. Dorotovič et al. (2008) observed a pore for 11 hours and reported periodicities in the range of 20-70 minutes. These oscillations were consequently interpreted as linear low-frequency slow sausage waves. Morton et al. (2011) used the Rapid Oscillations in the Solar Atmosphere (ROSA) instrument to also identify linear sausage oscillations in a magnetic pore. However, determining whether the oscillations were slow or fast proved to be difficult.

The source and driving mechanism(s) of these MHD sausage modes have been very difficult to identify. Numerical simulations of a flux tube rooted in the photosphere, which is buffeted by a wide range of coherent sub-photospheric drivers, is one method for identifying the potential source of MHD sausage waves. These drivers can either be horizontal or vertical, single, or paired or else a power spectrum, with varying phase differences (see e.g. Fedun et al., 2011a,b; Khomenko et al., 2008; Malins and Erdélyi, 2007; Vigeesh et al., 2012). To understand these MHD sausage oscillations, it is necessary to firstly see if it is possible to identify the signature within solar magnetic waveguides.

3.2 Data collection and method of analysis

Three time series of images with high angular resolution have been chosen here in order to demonstrate the identification of MHD sausage waves. The images were taken in the G-band (430.5 nm), which samples the low photosphere. This line forms deep in the photosphere and has a line intensity defined as $\rho^2 \times$ line-of-sight column depth.

The images were acquired using:

1. The Swedish Vacuum Solar Telescope (SVST) situated on La Palma in the Canary Islands. Scharmer et al. (1985) provides a detailed description of the features of the SVST. The images were taken on 7 July 1999. The sunspot is in the active region (AR) NOAA 8620. The observing duration is 133 minutes with a cadence time of 25 seconds. The field of view (FOV) covers an area of 33,600 km by 54,600 km (1 pixel \approx 60 km). Bonet et al. (2005) gives a detailed analysis of this sunspot. A context image is the left-handed image of Figure 3.1.
2. The Dutch Open Telescope (DOT) is also situated on La Palma in the Canary Islands. Two series of imaging data sequences were taken using this telescope. A detailed guide of the features of the DOT is provided by Rutten et al. (2004). The first series of data were taken on 13 July 2005, and the sunspot is in the AR NOAA 10789. The region slowly decayed, and this sunspot led a small group of other magnetic structures. The observing length is 165 minutes and has a cadence time of 30 seconds. The second set of data, taken on 15 October 2008, is of one large pore with a light bridge which is about 15 pixels (750 km) wide in the AR NOAA 11005. The duration of the observing run is 66 minutes and has a cadence time of 20 seconds. Both DOT image sequences cover an area of 50,000 km by 45,000 km, where the maximum spatial resolution is 0.2" (\approx 140 km). Typical context images are the middle and right-handed panels of Figure 3.1.

To obtain information relating to the cross-sectional area of these waveguides, a strict and consistent definition of the area is required. This definition is that each pixel with a value of less than 3σ of the median background intensity is counted as part of the waveguide. The background is defined as an area of the image where there are no formed magnetic structures. This may appear to be an arbitrary definition; however, a histogram of the background intensity reveals a Gaussian distribution, and when adding the area around and including the waveguide, there is significant

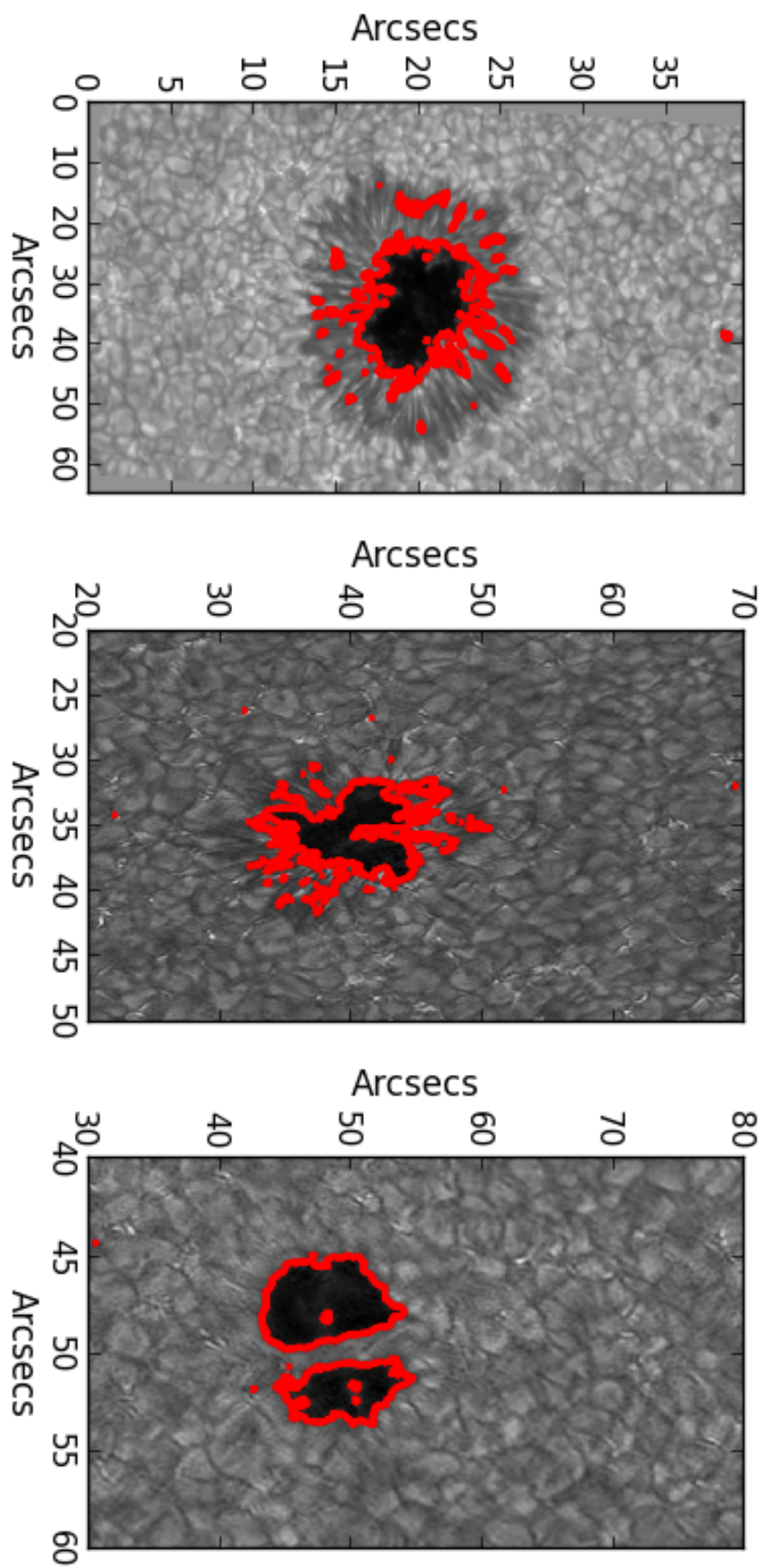


Fig. 3.1 An overview of the magnetic waveguides observed for this analysis. (*left*) The 1999 sunspot observed with the SVST with an average umbral area of 19,650 pixels (50 Mkm^2). (*middle*) The 2005 sunspot observed with the DOT with an average umbral area of 12,943 pixels (32 Mkm^2). (*right*) The 2008 pore observed with the DOT with an average area of 10971 pixels (27 Mkm^2), the light bridge that separates the pore can be seen. Furthermore, these structures were seen near the disk centre, so there is little to no LOS effect. The red line shows the thresholding technique applied to each waveguide at the start of the data series.

peak on the lower end of the Gaussian distribution curve around 3σ or higher. Thus, we have a 99% confidence that the area is of the structure and not of the background.

Figure 3.1 shows each waveguide at the start of the time series, where the red contour line represents the area found. The definition is accurate, but, it does include some non-waveguide pixels. The total intensity was determined by summing over the intensity of each pixel found in the waveguide. These waveguides are not static structures because, they slowly changed in size during the observing period. This background trend has to be removed for it not to mask any weak oscillation signatures. The detrending was accomplished by a non-linear regression fit and the consistency of the results was compared to subtracting the residue from an empirical mode decomposition (EMD) analysis (explained below). The residue is the data that remains after the EMD procedure has extracted as many signals as possible and it provides a very good approximation of the background trend.

The resulting reduced data series were then analysed with a wavelet tool in order to extract any periods of oscillation present within the data. The algorithm used is an adapted version of the IDL wavelet routine developed by Torrence and Compo (1998). The standard Morlet-wavelet, which is a plane sine wave with an amplitude modulated by a Gaussian function, was chosen for its suitable frequency resolution. The white cross-hatched area marks the cone of influence (COI), where edge effects of the wavelet structure affect the wavelet transform, and anything inside the COI is discarded. The white dashed line contour shows the confidence level of 95%. The wavelet method is very susceptible to noise at short periods and at times may not identify the true power of short periods.

Beyond this, the data representing the size and intensity has also been analysed using EMD, which decomposes the time series into a finite number of intrinsic mode functions (IMFs). IMFs are essentially narrowband-filtered time series, with each IMF containing one or two periods that exist in the original data series. The EMD technique was first proposed by Huang et al. (1998) and offers some benefits over more traditional methods of analysis, such as wavelets or Fourier transforms. However, one drawback is that it is very prone to error with regards to long periods. The problems associated with both the wavelet and EMD process means that the two complement each other. Furthermore, periods that appear in the wavelet *just* below the confidence level, but appear strongly in the EMD process, is a good indication that a period is not spurious. Generally, the next step after EMD analysis is to construct a Hilbert power spectrum that has a better time and spatial resolution than either wavelet or FFT routines. However, this has not been carried out owing to a

lack of a robust code base at this time. At this stage, we rely on wavelet and EMD analyses, as is customary in solar physics.

3.3 Results and discussion

3.3.1 LOS, circularity, and evolution of the waveguide

Several points need to be clarified for the data presented here before the full analysis. Firstly, there are LOS issues: Cooper et al. (2003a,b) have investigated how the LOS angle affects various aspects of observing coronal loops in a 2D model. Overall they found that for the slow sausage MHD wave, for a range of angles from $\pi/6$ to $\pi/3$, the observed intensity decreases as the LOS angle increases. Secondly, the larger angles lengthened the *observed period* of the wave. While the objects here are not coronal loops, the LOS angle still matters and should behave similarly. The LOS angles in all three cases were less than 30° thereby limiting any relevant effects of LOS.

Sunspots or pores are not fully circular and can have arbitrary shapes. The effects of a non-circular shape have been studied by, for example, Ruderman (2003), Morton and Erdélyi (2009), and Morton and Ruderman (2011). While they do not account for the very complicated and real structure of the sunspots and pores observed here, they still offer adequate insight. Current theory suggests the shape will have a minor effect on the oscillations unless it has a significant deviation from circularity. Likewise, the structure of each waveguide undergoes a minor change during the observation campaign, limiting any effects from large-scale structural change, as can be seen in Figure 3.2.

3.3.2 MHD theory for phase relations

Treatment of the MHD equations makes it possible to determine phase relations between various physical quantities for propagating and standing MHD waves. This has been summarised briefly by Goedbloed and Poedts (2004) and also applied by Fujimura and Tsuneta (2009). The latter find that the phase relation for the slow MHD wave with regards to cross-sectional area and density is in phase regardless of whether the wave is propagating or standing. More recently, Moreels and Van Doorsselaere (2013) have expanded on this idea, taking factors into account such as LOS, which were neglected earlier, but also expanding the theory to cover fast MHD sausage waves. The phase relation for the magnetic field to the cross-sectional area is in phase when assuming that the plasma is frozen in to the magnetic field.

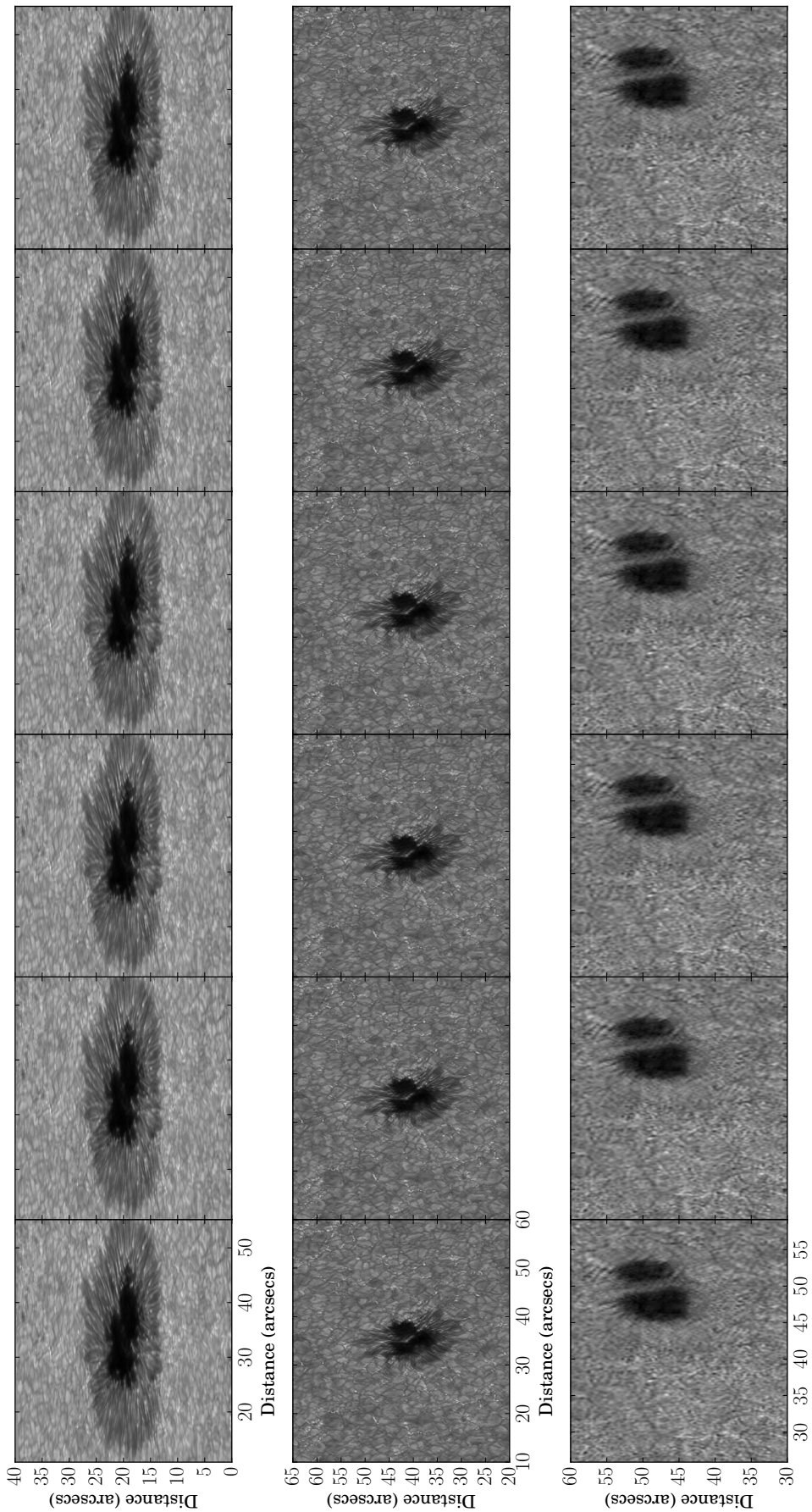


Fig. 3.2 Waveguides seen through six different parts of the observation sequence. The image sequence has time increasing from left to right. The first row is the 1999 sunspot, the middle row the 2005 sunspot, and the last row the 2008 pore.

Supplementary information from other perturbation phase relations, such as velocity and the magnetic field, allows one to determine whether the observed MHD wave is slow or fast. In summary, the slow MHD sausage mode shows in-phase behaviour between intensity and area perturbations, while the fast sausage mode shows out-of-phase behaviour. Before progressing, we need to address the opacity effect on MHD wave perturbations. This is relevant, since intensity fluctuations can be due to the change of the optical depth along the LOS, which has the same phase difference as the fast MHD sausage wave and as a result is indistinguishable without further information (Fujimura and Tsuneta, 2009).

Recently, Moreels et al. (2013) have analytically determined the phase difference between the cross-sectional area and the total intensity perturbations for both the slow and fast MHD sausage modes. They find that, for both the slow body and surface MHD wave, the behaviour is in phase, while for the fast surface wave, the behaviour is out of phase. This result means that it is possible to approximately separate slow and fast sausage waves without the use of other observable variables. Their results will be used here to distinguish between slow and fast MHD sausage modes.

3.3.3 Sunspot, 7 July 1999 , AR 8620

Figure 3.3 shows the wavelet analysis of the 1999 sunspot area and intensity data. There are four confidently identified periods that exist in the area wavelet with 95% certainty; 4, 7, 16, and 32 minutes. The 32-minute period is found over a wide range of the time series, with some of its power inside the COI. However, most is confidently outside the COI. The 16-minute period is strongly localised at 50 to 120 minutes of the data series, starts at 18 minutes, and slowly increases and stabilises at 14 minutes. There is a third and fourth period at four and seven minutes that just reach the significance level and appear sporadically during the time series.

The intensity wavelet shows three distinct periods of oscillations above the confidence level: 4, 16, and 36.5 minutes. The 36.5-minute period has a corresponding area wavelet oscillation at 32 minutes. While the 16-minute oscillation corresponds to the 16-minute oscillation found in the area. Furthermore, the 16-minute period starts with very concentrated power and does not display the same period change as the area oscillation does. Finally, the four-minute period also corresponds to an oscillation found in the area but is also sporadic in its appearance.

It is safe to say that these oscillations are caused by sausage waves. The reason is that in linear ideal MHD theory, the sausage wave is the only MHD wave capable of changing the area of the flux tube that is observed on disk (see e.g. Cooper et al.,

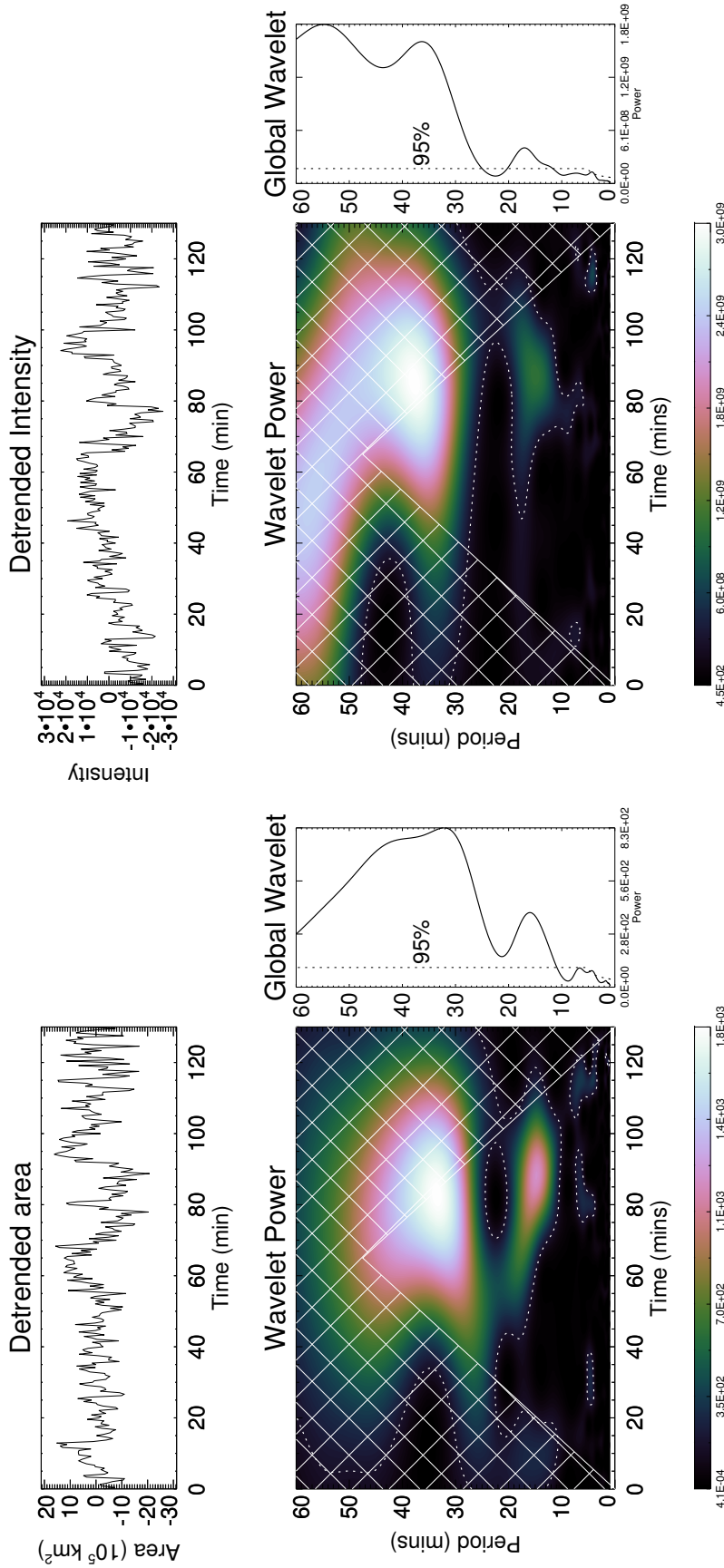


Fig. 3.3 (*left image*) Evolution of the area of the 1999 sunspot (*upper panel*); the wavelet power spectrum for a white noise background, the cone of influence is marked as a cross-hatched area where edge effects become important and the contour lines show the 95% confidence level (*lower left panel*). Global (integrated in time) wavelet power spectrum, where the dashed line shows the 95% confidence limit (*lower right panel*). (*right image*) The same as the left image but for the mean intensity of the 1999 sunspot.

2003a; Wang, 2004). Without the ability to directly compare the phase difference of the area to the intensity, great caution needs to be exercised to determine with confidence whether the perturbations are fast or slow. A wavelet phase diagram reveals regions (where the wavelet coherence is high and the period is ≤ 20 minutes) to be either out of phase or in phase, but a clear image of constant phase difference does not appear. This might be due to mode conversion occurring in the sunspot, since the G-band samples a region where the plasma- $\beta \approx 1$ in a magnetic structure (Gary, 2001). When the period is ≥ 20 minutes, the only area of high coherence is located around 30 minutes and found to be nearly out-of-phase, which hints that there might be a fast surface sausage wave. However, only two full wave periods are outside the COI, which is due to the total length of the data series. This behaviour indicates that for short periods, a mixture of fast surface and slow MHD sausage waves are present while for the long period, it is purely a fast surface MHD sausage wave.

Figure 3.4 shows the computed IMFs for the 1999 sunspot data set. The IMFs show the periods of oscillations identified using the EMD routine. IMFs which show irrelevant periods, or the additional residue are ignored. In general, the higher order IMFs tend to show longer periods and, as such, contain fewer wave periods, which makes phase identification less reliable. Four IMF overlays are shown, and IMFs with similar periods to the wavelet plots have been overlaid in order to aid comparison for each dataset.

Four IMFs directly coincide with the wavelet period that reveal both area and intensity perturbations. IMF c_3 displays the four-minute period where major regions of in-phase behaviour can be seen; however, either side shows one or two wave periods of out-of-phase behaviour. IMF c_4 exhibits a period of seven minutes. The picture here is more muddled as an extra period is present in the intensity, namely 11 minutes, making phase identification harder for the seven-minute period. Where the IMFs coincide with the same period, namely at the start of the time series, the phase difference is approximately 45 degrees, which the authors have no theoretical explanation for. IMF c_5 displays a 16-minute period, with in-phase behaviour. Finally, IMF c_6 contains the 32-minute period. This period does not fully match the period seen in the intensity, but also one of the edge effects of the EMD process can be seen in the intensity signal. Near the end of the time series, the two IMFs overlap with the same period with an in-phase behaviour. In summary, the EMD process shows that the major behaviour is in phase, indicating the existence of a slow sausage mode. Also the regions of changing phase difference at lower periods

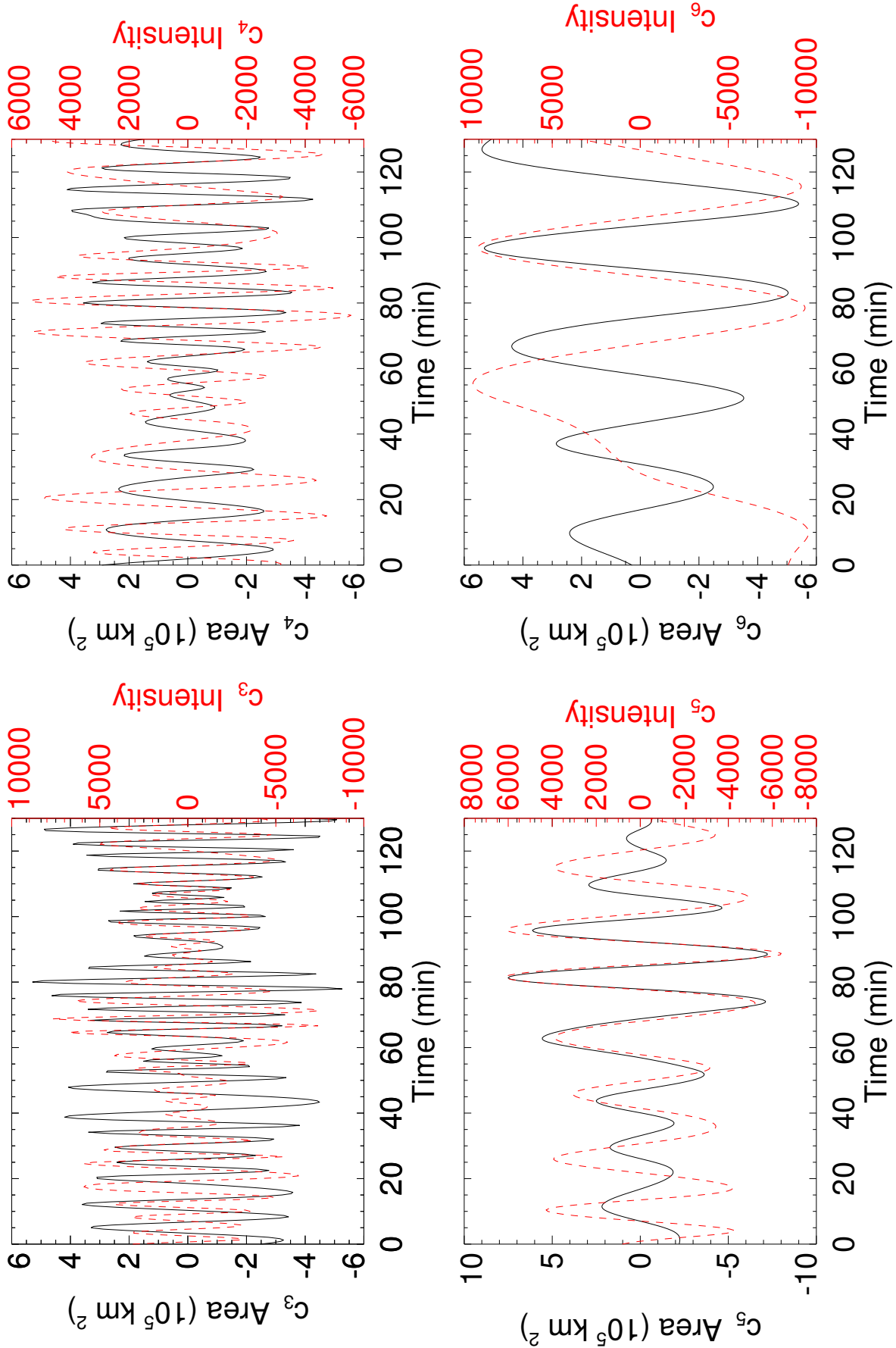


Fig. 3.4 The IMFs of the evolution of the area (red) and intensity (black) for the 1999 sunspot, over-plotted to aid comparison. Generally after the 6th IMF, higher IMFs lack a sufficient number of wave periods, which makes it difficult and less reliable to obtain an accurate period.

indicates the potential existence of a fast surface mode. However, the last IMF does not agree with the wavelet phase due to the artefact from the EMD process.

It was possible to approximately separate the penumbra from the umbra and investigate its area for oscillations. However, the penumbra is a highly dynamic object and this makes the area estimation reasonably uncertain. There seem to be four periods that exist at 95 % certainty: 5, 9, 15, and 25. The three shorter periods (5, 9, and 15 minutes) closely correspond to the 4-, 7-, and 16-minute oscillations in the umbra; they could be a continuation of these umbral periods that became up-shifted as they enter the less compact structure of the penumbra. While the 25-minute period does not directly correspond to an observed area oscillation. The wavelet phase analysis shows large regions of out-of-phase behaviour where the period is either below ten minutes or above 20 minutes. This behaviour is a mixed collection of fast surface and slow sausage modes, with regions moving from one phase difference to another after three or more wave periods.

3.3.4 Sunspot, 13 July 2005, AR 10789

Figure 3.5 shows the wavelet analysis of the 2005 sunspot area and intensity in AR 10789. There are four periods that exist at 95% confidence level: 4, 7.5, 11, and 16.5 minutes. Each period has a region of high power in the wavelet, with the lower periods appearing nearer the end of the time series. The corresponding intensity wavelet reveals that there are three periods of 4, 7.5, and 10.5 minute oscillations; however, the 16.5-minute oscillation is present but is a very weak signal. The cross-wavelet phase indicates that these oscillations are in phase. There are no major regions of out-of-phase behaviour.

Figure 3.6 shows the IMFs for the area and the intensity of the sunspot data in AR 10789. In this case, each period is found by the EMD process. IMF c_2 , IMF c_3 , IMF c_4 , and IMF c_5 correspond to the 4, 7.5, 11, and 16.5-minute oscillation periods, respectively. IMF c_2 displays extensive in-phase behaviour throughout the time series, which is a strong indication of the slow sausage MHD wave at a period not too dissimilar to the global p -mode oscillation. The region of interest is within the time interval of 90 to 130 minutes for IMF c_4 , where the wavelet has these oscillations. The IMF shows clear in-phase behaviour in this time interval. The overall phase relation between the area and intensity indicates the presence of slow sausage waves.

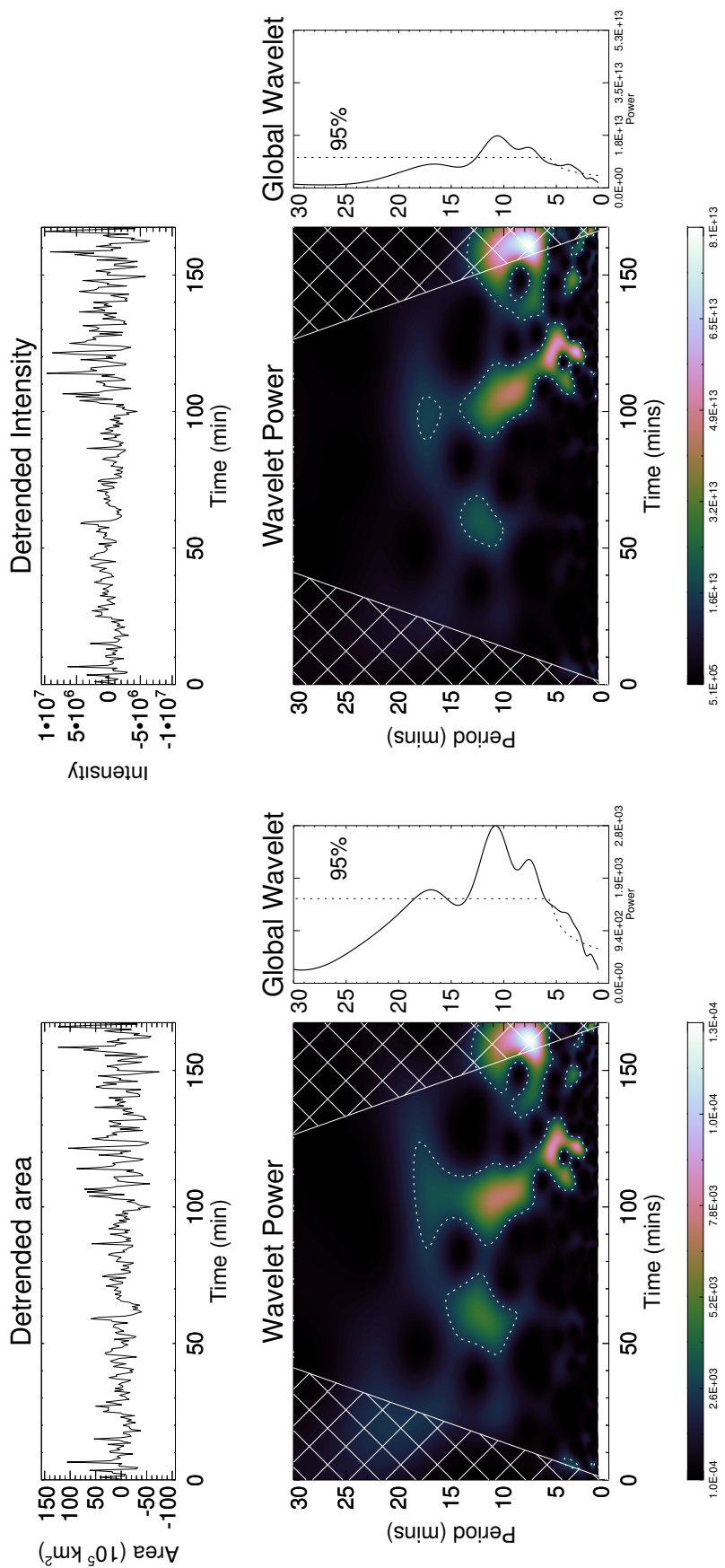


Fig. 3.5 Same as Figure 3.3 but for the sunspot in AR 10789 in 2005.

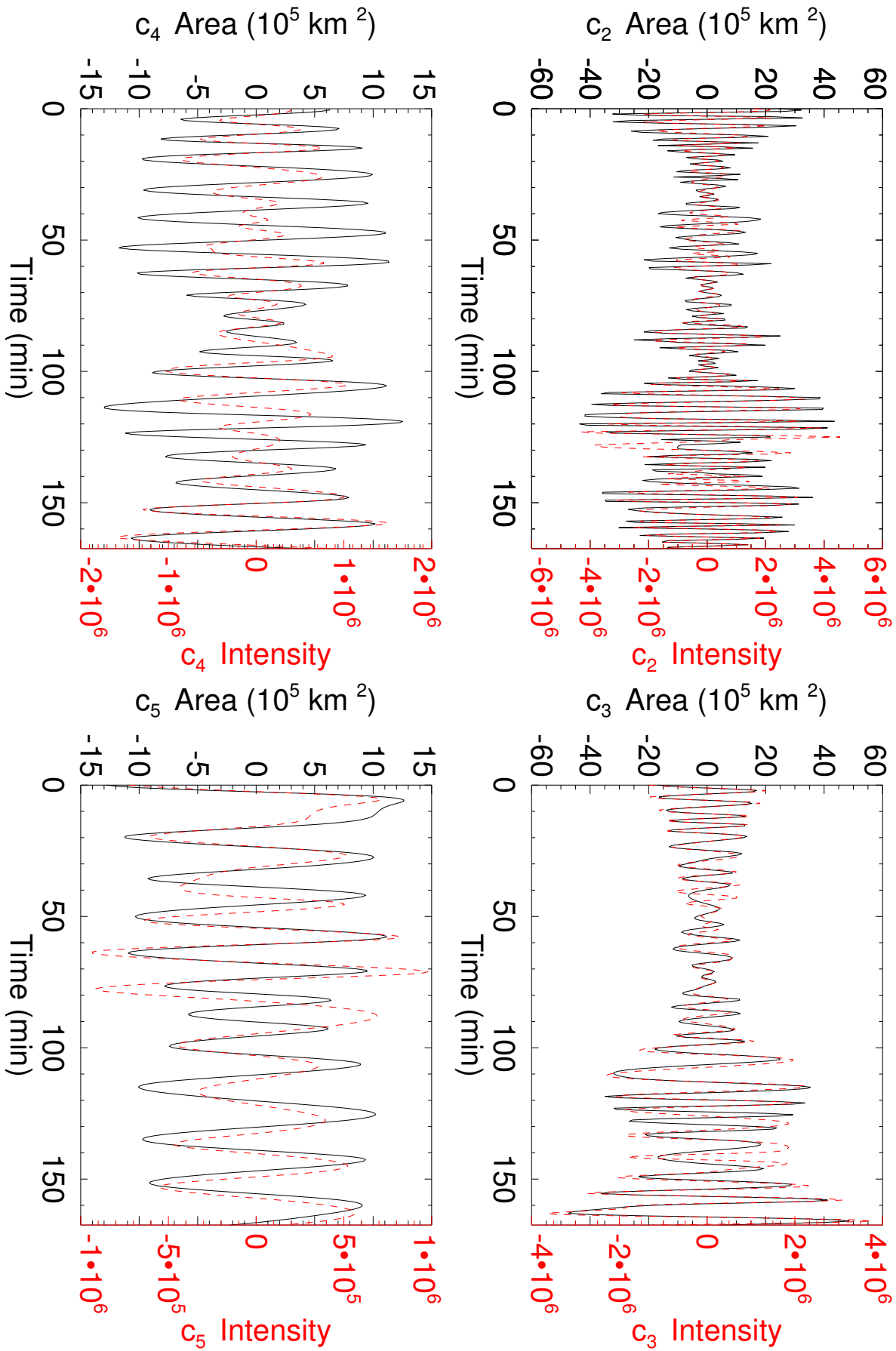


Fig. 3.6 Same as Figure 3.4 but for the sunspot in AR 10789 in 2005.

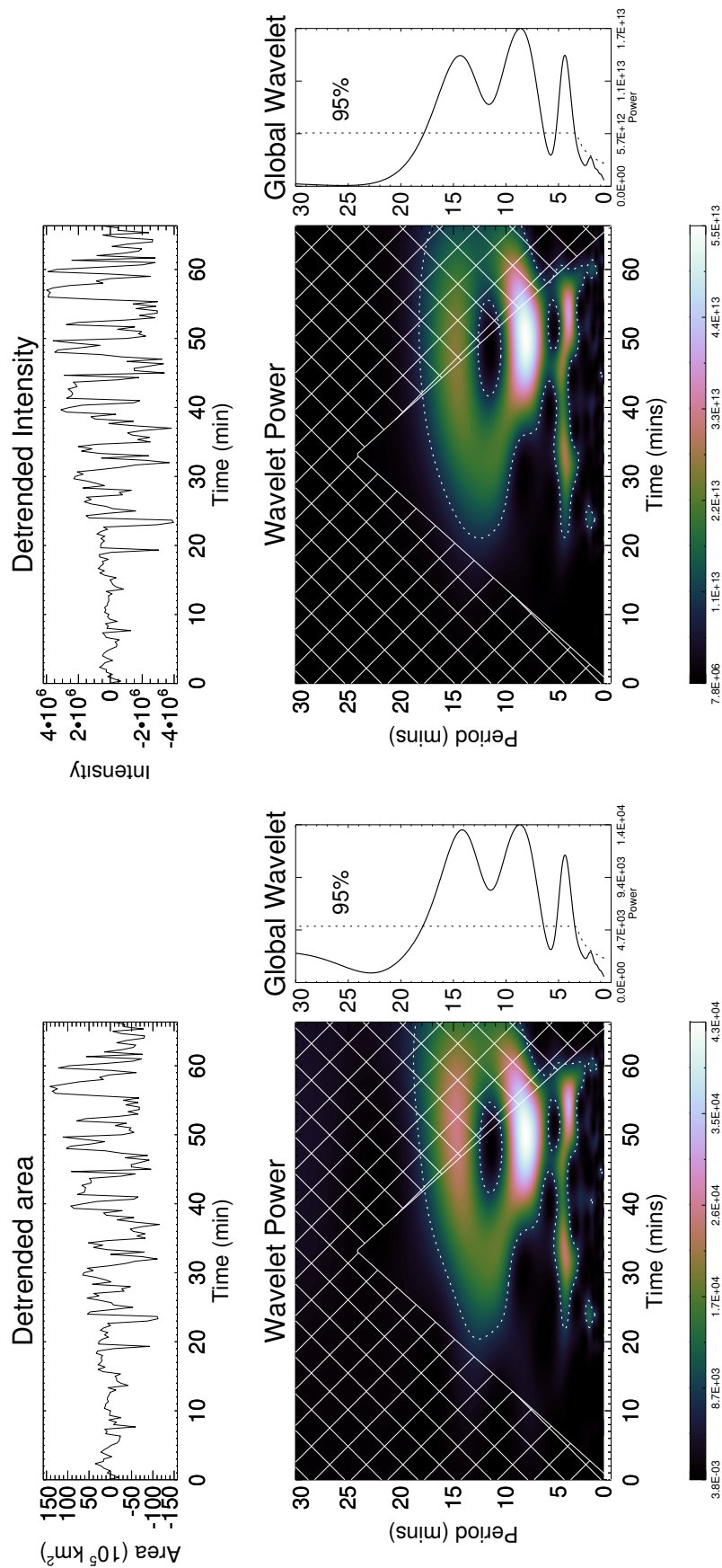


Fig. 3.7 Same as Figure 3.3 but for the pore in AR 11005 in 2008.

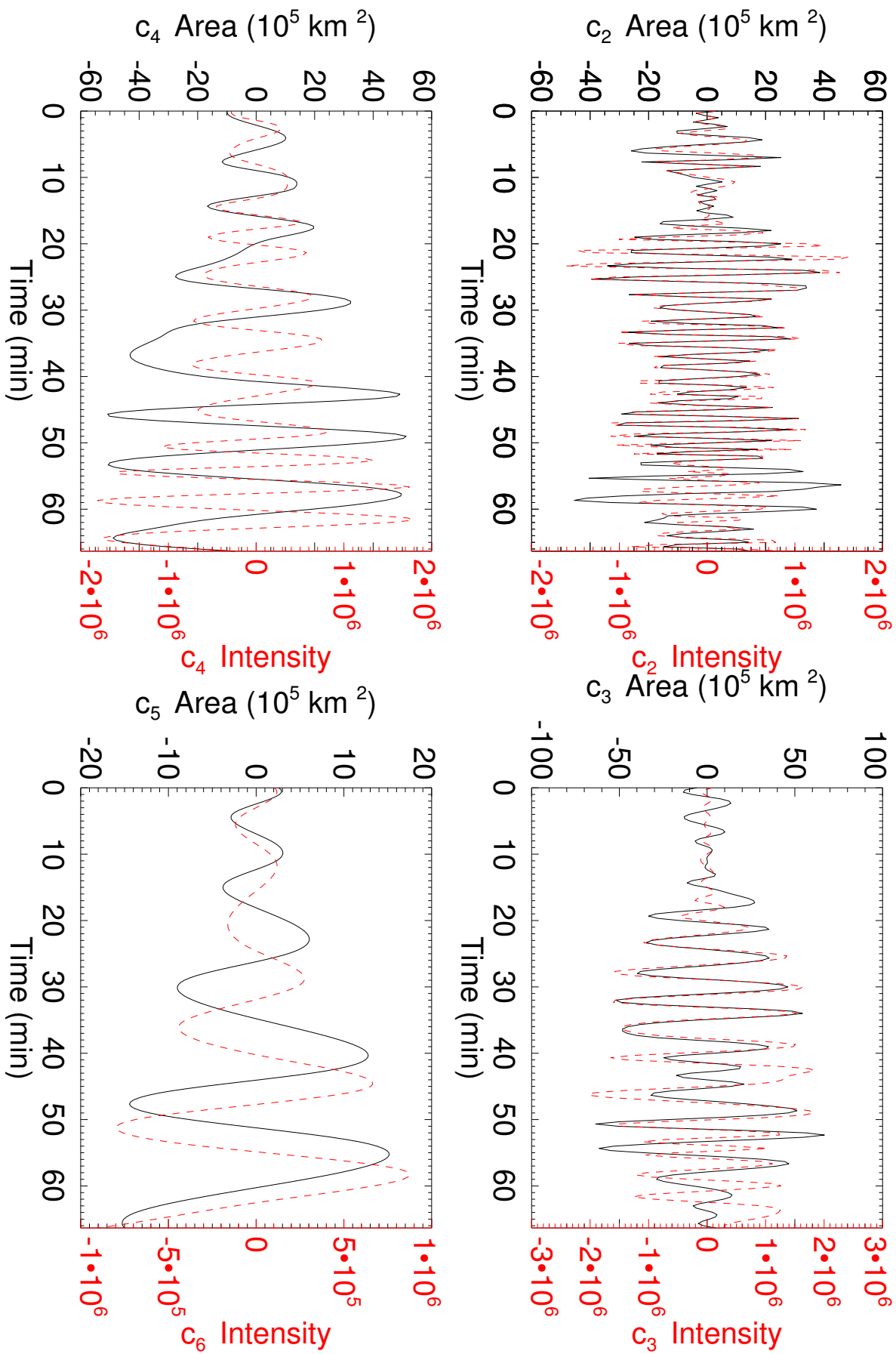


Fig. 3.8 Same as Figure 3.4 but for the pore in AR 11005 in 2008.

3.3.5 Pore, 15 October 2008

Figure 3.7 shows the wavelet analysis of the pore with a light bridge. There are three periods that exist at 95 % confidence level: 4.5, 8.5, and 14.5 minutes. The large part of the power of the period of 14-15 minutes is inside the COI; however, the period appears in the EMD analysis and has a large portion of power outside the COI and thus has not been ignored for this analysis. The three periods are seen in both area and intensity data when the wavelet analyses are cross-correlated. The power for these two periods is concentrated in the time interval of 20 to 60 minutes. The cross-wavelet analysis shows that the overlapping time span is somewhat smaller, at about 30 to 50 minutes. Furthermore, the wavelet power for each period runs parallel to each other throughout the time series, and they appear at the same time and seem to fade away at a similar time as well.

Figure 3.8 shows the IMFs for the area with intensity over-plotted. In this case, IMF c_3 indicates a period of 4.5 minutes and IMF c_4 has a characteristic period of 8.5 minutes, and this applies to both the area and intensity IMFs. IMF c_3 reveals that the phase relation is in-phase for the majority of the time series. IMF c_4 reveals large regions of roughly in-phase behaviour but with, again, a 45-degree phase difference. Not shown is the comparison of IMF c_4 and IMF c_5 for the area and intensity, respectively. At the end of the time series for both, there is a mixture of in-phase behaviour but also with the intensity signal leading the area signal for the 8.5 minute oscillation. IMF c_5 and IMF c_6 for the area and intensity, respectively, show a period of 14.5 minutes. There is a region of near out-of-phase behaviour before this then turns into 45-degree phase difference with the area leading the intensity perturbations. Consistently, there are occurrences of unexplainable phase differences that require a theory to be developed to explain.

The easiest way to confirm the linearity of waves is to compare the amplitude of the oscillations to the characteristic scale of the structure. In all three cases studied here, the oscillation amplitudes are around 10% or less of the total area, which indicates that these oscillations are linear. Furthermore, the amplitude of the oscillation in the last two cases is by and large the same, so the amplitude has scaled with the size of the structure. However, for the 1999 sunspot, the amplitude of the oscillation is an order of a magnitude less. Whether this is due to the large size of the sunspot or the very stable nature during the observation window needs to be investigated in future work.

Data set	Period (Mins)	Ratio (P_1/P_i)
Sunspot 1999	$P_1 - 32 \pm 2.5$	-
	$P_2 - 16 \pm 1.5$	2 ± 0.2
	$P_3 - 7 \pm 0.5$	4.6 ± 0.3
	$P_4 - 4 \pm 0.5$	8 ± 0.5
Sunspot 2005	$P_1 - 16.5 \pm 1.5$	-
	$P_2 - 11 \pm 0.5$	1.5 ± 0.2
	$P_3 - 7.5 \pm 0.5$	2.2 ± 0.2
	$P_4 - 4 \pm 0.5$	4.2 ± 0.6
Pore 2008	$P_1 - 14.5 \pm 0.5$	-
	$P_2 - 8.5 \pm 0.5$	1.7 ± 0.1
	$P_3 - 4.5 \pm 0.5$	3.2 ± 0.2

Table 3.1 The periods of oscillations that are found in the area of the waveguides that exist at 95% confidence level.

3.4 Standing harmonics

Basic MHD theory interpretation allows sunspots and pores to be described as vertical cylindrical flux tubes, with the base bounded in the photosphere and the top bounded at the transition region due to the sharp gradients in the plasma properties at these locations. Taking this further, an ideal flux tube is assumed here. The plasma density and magnetic field are homogeneous within the flux tube. This means that the standing harmonics of such flux tubes are the MHD equivalent to the harmonics in an open-ended compressible air pipe, where the ratio of the harmonic periods is given by $P_1/P_2 = 2$, $P_1/P_3 = 3$, and so forth. This only applies in the long-wavelength or thin-tube approximation. Using harmonic ratios to carry out magneto-seismology has been used, for example, by Andries et al. (2005a,b) who researched the effects of longitudinal density stratification on kink oscillations and resonantly damped kink oscillations, while Luna-Cardozo et al. (2012) studied longitudinal density effects and loop expansion on the slow sausage MHD wave. Luna-Cardozo et al. (2012) found that specific density profiles in lower atmospheric flux tubes could increase or decrease the value of the period ratio. The authors are unaware of any work that gives the changes to further harmonic ratios, so the assumption that the amount of deviation from the canonical value for the period ratio (P_1/P_2) is the same for other period ratios; e.g., P_1/P_3 or higher is used.

We now summarise the observed findings. Table 3.1 contains the periods of oscillations found in all three magnetic waveguides. There are four periods found for the 1999 sunspot. The second period of 16 minutes gives a period ratio (P_1/P_2) of 2 ± 0.2 , which is exactly the same as the expected value of a uniform waveguide

with a canonical value of 2. The next period ratio is 4.6 ± 0.3 . Here, the change from canonical value is substantial if this is indeed the third period, which should be around 10.6 minutes, unless the effect on the harmonic ratio increases with each successive ratio. The last period is difficult to incorporate into the harmonic standpoint, and it is most likely that the four-minute period is due the global *p*-mode.

For the 2005 sunspot in AR 10789, there is a clearer picture of potential harmonics. The first period is 16.5 minutes and the second period is 11 minutes, which gives a ratio of 1.5 ± 0.2 , and the third period of 7.5 minutes gives a ratio of 2.2 ± 0.3 . The period ratio is modified downwards in a consistent manner as the harmonic number increases. These ratios are strong evidence of standing waves in this magnetic waveguide. As was the case for the 1999 sunspot, the period at four minutes has a period ratio that does not fit into this harmonic viewpoint and is most likely due to the global *p*-mode instead.

For the 2008 pore of AR 11005, the picture is more muddled by the short available time series. Taking the 15-minute period to be the first harmonic, the ratio is 1.7 ± 0.1 for the 8.5-minute period, very similar to both first-period ratios of the previous sunspots. The third period is again very close to the period of the global *p*-mode.

The main conclusion to take away from this data analysis at this point is that the simple homogeneous flux tube model cannot fully account for these ratios. However, this simple model seems to be robust enough to give a good first insight. The most likely reasons for deviation from the canonical period ratio value are, firstly, that sunspots and pores (just like most lower atmospheric magnetic structures) expand with height, causing magnetic stratification (Luna-Cardozo et al., 2012; Verth and Erdélyi, 2008), and secondly, that the Sun's gravity causes density stratification (Andries et al., 2009). These two effects will either increase or decrease the period ratio of the harmonics depending on the chosen density or magnetic profile (see Luna-Cardozo et al. (2012) for a detailed analysis in the context of slow sausage oscillations or see Erdélyi et al. (2013) for kink modes). In addition, these magnetic structures are rarely purely cylindrical, but can be elliptical (or arbitrary) in shape (see Morton and Erdélyi, 2009; Ruderman and Erdélyi, 2009) and in most cases are non-axially symmetric. Also, in some cases the flux tube is more suitably described as closed-ended at the photosphere and open-ended at the transition region, which would remove the even harmonics.

3.5 Conclusion

In this chapter we have investigated three magnetic waveguides with the objective of detecting MHD sausage waves and determining whether they are slow or fast, propagating or standing. Based on the results presented here, we confidently interpreted the observed periodic changes in the area cross section of flux tubes, which are manifested as a pore and two sunspot waveguide structures, as proof of the existence of linear slow and fast surface sausage MHD oscillations. Using wavelet analysis, we found standing waves in the photosphere with periods ranging from 4 to 32 minutes. Employing complementary EMD analysis has allowed the detected MHD modes to be identified as a combination of *fast surface sausage* and *slow sausage* modes, thanks to the phase difference of the area and intensity. It is very likely that these oscillations are *standing harmonics* supported in a flux tube. The period ratio ($P_1/P_{i=2,3}$) of these oscillations indicates strongly that they are part of a group of standing harmonics in a flux tube that is non-homogeneous and bound by the photosphere and the transition region. Furthermore, there is possible indirect evidence of mode conversion occurring in one of these magnetic waveguides.

Chapter 4

Slow MHD sausage waves within small-scale photospheric magnetic structures.¹

¹Accepted for publication in The Astrophysical Journal.

4.1 Introduction

Improvements in space- and ground-based solar observations have permitted the detection and analysis of small-scale waveguide structures in the Sun's lower atmosphere. One such structure is a magnetic pore: a magnetic concentration with a diameter that ranges from 0.5 to 6 Mm with magnetic fields of 1 to 3 kG that typically last for less than a day (Simon and Weiss, 1970). Magnetic pores are highly dynamic objects due to e.g., constant buffeting from the surrounding granulation in the photosphere. A collection of flows and oscillations have been observed within and around magnetic pores (Balthasar, 1999; Dorotović et al., 2014; Dorotović et al., 2002; Freij et al., 2014; Hirzberger et al., 2002; Jess et al., 2015; Moreels et al., 2015; Roudier et al., 2002; Solanki, 2003). The major apparent difference between a sunspot and a magnetic pore is the lack of a penumbra: a region of strong and often very inclined magnetic field that surrounds the umbra.

It is important to understand which magnetohydrodynamic (MHD) waves or oscillatory modes can be supported in magnetic flux tubes in the present context. The reason for this is two-fold: it clarifies the observational signatures of each mode; and, whether that mode will manifest given the conditions of the local plasma. Furthermore, absorption of the global acoustic *p*-mode, and flux tube expansion will induce a myriad of MHD waves. Roberts (2006) investigated how the slow mode may be extracted elegantly from the governing MHD equations, considering the special case of a vertical uniform magnetic field in a vertically stratified medium. The approach may, in principle, be generalized with non-uniform magnetic fields (Luna-Cardozo et al., 2012) and, by taking into account non-linearity, background flows and dissipative effects. However, as we will show below, a first useful insight still can be made within the framework of ideal linear MHD applied to a static background.

It is very difficult to directly (or often even indirectly) measure the background physical parameters (plasma- β or density, for example) of localised solar structures. For the magnetic field, the most common method is to measure the Stokes profiles of element lines in the lower solar atmosphere and then perform Stokes inversion in order to determine the magnetic field vectors. More recently, the development of solar magneto-seismology (SMS) has allowed the estimation of the local plasma properties which are generally impossible to measure directly (Andries et al., 2009; Ruderman and Erdélyi, 2009). While, this technique has been used for many years in the solar corona, only recently has it been applied to the lower solar atmosphere. For example, Fujimura and Tsuneta (2009) accomplished this by observing and identifying wave behaviour in lower solar structures and interpreting the observed waves as standing

MHD waves. A recent review on lower solar atmospheric application of MHD waves is given by e.g. Banerjee et al. (2007) and partially by Mathioudakis et al. (2013) in the context of Alfvén waves.

Extensive numerical modelling of wave propagation in small-scale flux tubes has been undertaken by Fedun et al. (2011a,b); Hasan and Van Ballegooijen (2008); Kato et al. (2011); Khomenko et al. (2008); Mumford et al. (2015); Shelyag et al. (2011); Vigeesh et al. (2012); Wedemeyer-Böhm et al. (2012). These models are of localised magnetic flux tubes and the effect of vertical, horizontal or torsional coherent (sub) photospheric drivers mimicking plasma motion at (beneath) the solar surface on these flux tubes. It was found that extensive mode conversion may take place within flux tubes as well as the generation of slow and fast MHD modes or the Alfvén mode that depended on the exact driver used.

Vögler et al. (2005) and Cameron et al. (2007), using the MURaM code, simulated larger scale magnetic structures, including pores, to build up a detailed picture of the physical parameters (density, pressure and temperature) as well as flows in and around these structures, which has good observational agreement.

Dorotovič et al. (2008) observed the evolution of a magnetic pore's area for 11 hours in the sunspot group NOAA 7519 (see Dorotovič et al., 2002; Sobotka et al., 1997). They reported that the periodicities of the detected perturbations were in the range of 12–97 minutes and were interpreted as slow magneto-acoustic-gravity sausage MHD waves. Morton et al. (2011), using the Rapid Oscillations in the Solar Atmosphere (ROSA) instrument installed on the Dunn Solar Telescope (DST), also detected sausage oscillations in a solar pore. The lack of Doppler velocity data made it difficult to conclude whether the waves were propagating or standing. The oscillatory phenomena were identified using a relatively new technique (at least to the solar community), known as Empirical Mode Decomposition (EMD). The EMD process decomposes a time series into Intrinsic Mode Functions (IMFs) which contain the intrinsic periods of the time series. Each IMF contains a different time-scale that exists in the original time series (see Terradas et al., 2004). This technique was first proposed by Huang et al. (1998) and offers certain benefits over more traditional methods of period analysis, such as wavelets or Fourier transforms.

Dorotovič et al. (2014) observed several large magnetic structures and analysed the change in time of the cross-sectional area and total intensity of these structures. Phase relations between the cross-sectional area and total intensity have been investigated by Moreels et al. (e.g., 2013); Moreels and Van Doorsselaere (e.g., 2013). The phase difference found observationally was 0° , i.e., in-phase, which matches the phase relation for slow MHD sausage waves. Further, these magnetic structures were

able to support several oscillations with periods not to dissimilar to standing mode harmonics in an ideal case. Grant et al. (2015) observed a magnetic pore within Active Region NOAA 11683, using high-resolution scans of multiple heights of the solar atmosphere using ROSA and Interferometric Bidimensional Spectrometer (IBIS) on the DST. They showed that sausage modes were present in all the observed layers which were damped whilst they propagated into the higher levels of solar atmosphere. The estimated energy flux that suggests the could contribute to the heating of the chromosphere.

Standing waves are expected to exist in the lower solar atmosphere bounded by the photosphere and transition region (Leibacher et al., 1982; Mein and Mein, 1976). Numerical models also predict this behaviour (Erdélyi et al., 2007; Malins and Erdélyi, 2007; Zhugzhda and Dzhailov, 1982). Standing waves have been potentially seen in the lower solar atmosphere; using the Hinode space-borne instrument suite, Fujimura and Tsuneta (2009) observed pores and inter-granular magnetic structures, finding perturbations in the magnetic field, velocity and intensity. The phase difference between these quantities gave an unclear picture as to what form of standing waves these oscillations were. Standing slow MHD waves have been detected in coronal loops with SoHO and TRACE (for reviews see, e.g., De Moortel and Nakariakov, 2012; Wang, 2011) and transverse (kink) oscillations have been detected in coronal loops (e.g Aschwanden et al., 1999; O’Shea et al., 2007; Taroyan et al., 2005; Verth et al., 2008, for a review see Andries et al., 2009; Ruderman and Erdélyi, 2009). Harmonics of a standing wave have potentially been seen in flare loops using ULTRACAM (e.g., Mathioudakis et al., 2006). Fleck and Deubner (1989) also reported the observation of standing waves in the lower solar chromosphere, by measuring the brightness and velocity oscillations in Ca II lines.

In this article, we exploit phase relations between the area and intensity of two magnetic pores, in order to identify the wave mode of the observed oscillations. This information combined with the methods of solar magneto-seismology, allows us to determine several key properties of these oscillations and of the magnetic structures themselves. Section 4.2 details the observational data, its reduction and the analysis method. Section 4.3 discusses the theory of the applicable MHD wave identification as well as the solar magneto-seismology equations used to estimate properties of the observed oscillations. Section 4.4 contains the results of the data analysis while Sect. 4.5 summarises.

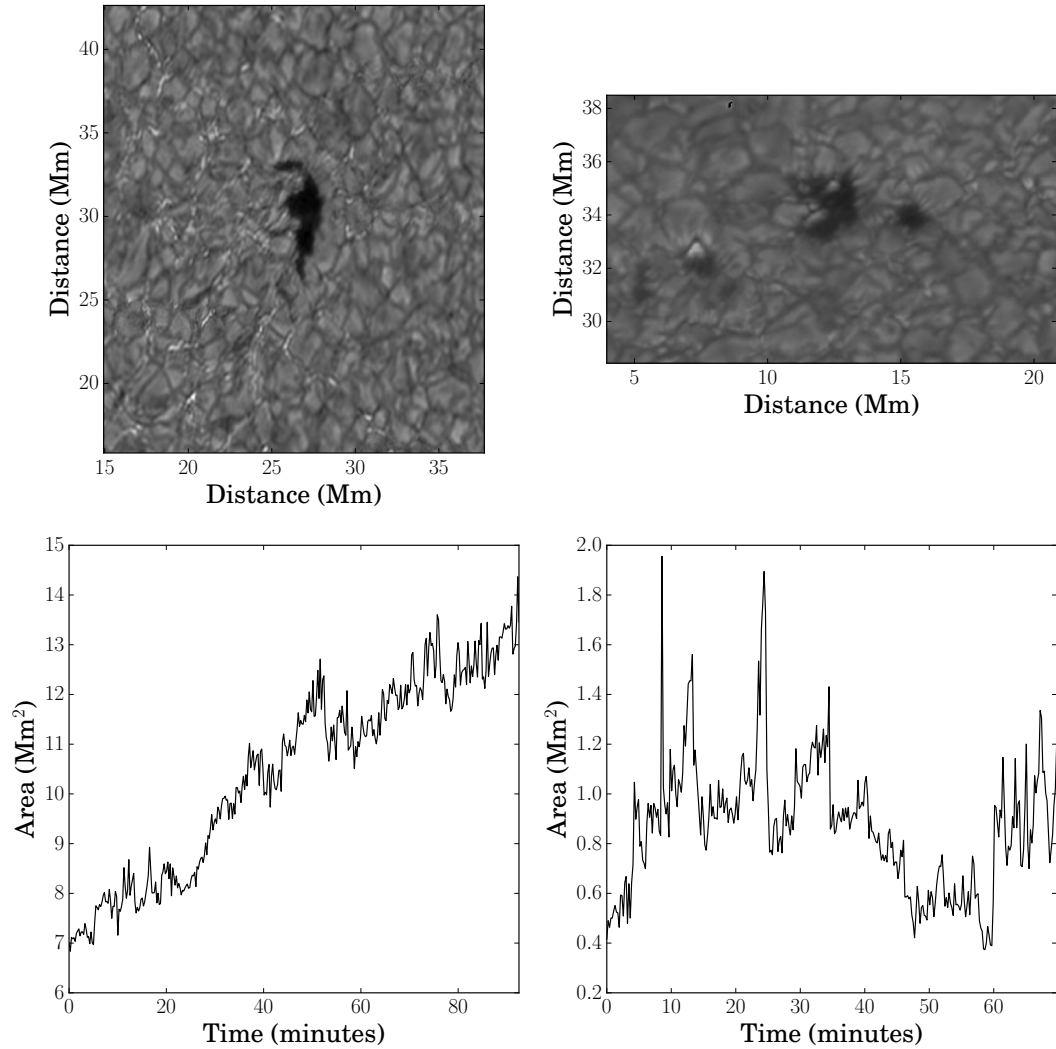


Fig. 4.1 The left column displays the magnetic pore observed by the DOT while the right column is the magnetic pore observed by the DST/ROSA. The magnetic pores at the start of the observation sequence (*Upper panels*). The original (trended) cross-sectional time series for each pore throughout the observation sequence. (*Lower panels*).

4.2 Data and Method of Analysis

Two high-resolution datasets are investigated within this article. The first dataset was acquired using the Dutch Open Telescope (DOT) (Rutten et al., 2004), located at La Palma in the Canary Islands. The data were taken on 12th August 2007 with a G-band (430.5 nm) filter which samples the low photosphere and has a formation height of around 250 km above the solar surface. The observation started at 08:12 UTC and lasted for 92 minutes with a cadence of 15 seconds with a total field-of-view (FOV) of 60 Mm by 40.75 Mm. The DOT is able to achieve high spatial ($0.071''$ per pixel) resolution, due to the DOT reduction pipeline. It comes at a cost of temporal cadence which is decreased to 30 seconds as data reduction uses speckle reconstruction (Keller and von der Luehe, 1992). Note, that the DOT does not have an adaptive optics system.

The second dataset was obtained on the 22nd August 2008 with the Rapid Oscillations in the Solar Atmosphere (ROSA) imaging system situated at the Dunn Solar Telescope (see Jess et al. 2010 for details on experimental setup and data reduction techniques). Observation started at 15:24 UTC, and data were taken using a 417 nm bandpass filter with a width of 0.5 nm. The 417 nm spectral line corresponds to the blue continuum which samples the lower photosphere and the formation height of the filter wavelength corresponds to around 250 km above the solar surface. It should be noted that this is an average formation height. This is because the contributions to the line are from a wide range of heights and the lines also form at different heights depending on the plasma properties (Uitenbroek and Tritschler, 2006).

ROSA has the ability for high spatial ($0.069''$ per pixel) and temporal (0.2 s) resolutions. After processing through the ROSA pipeline the cadence was reduced to 12.8 s to improve image quality via speckle reconstruction (Wöger et al., 2008). To ensure alignment between frames, the broadband time series was Fourier co-registered and de-stretched (Jess et al., 2007). Count rates for intensity are normalised by the ROSA pipeline.

The methodology of this analysis follows the one also applied by Morton et al. (2011) and Dorotovič et al. (2014). The area of the pore is determined by summing the pixels that have intensity values less than 3σ of the median background intensity, which is a large quiet-Sun region. This method contours the pore area well, but not perfectly, as the intensity between the pore and the background granulation is not a hard boundary. The top row of Figure 4.1 shows the magnetic pores at the start of the observation sequence, by DOT and ROSA, respectively. Further, the output from the area analysis is shown in the bottom row for both magnetic pores. A

strong linear trend can be observed for the DOT pore. The intensity time series was determined by total intensity of all the pixels within the pore. To search for periodic phenomena in the time series, two data analysis methods were used: wavelets and EMD. The wavelet analysis employs an algorithm that is a modified version of the tool developed by Torrence and Compo (1998). The standard Morlet wavelet, which is a plane sine wave with the amplitude modulated by a Gaussian function, was chosen due to its high resolution in the frequency domain. The EMD code employed here is the one of Terradas et al. (2004). First, we de-trended each time series by linear regression followed by wavelet analysis to determine the periodicity of the oscillations as a function of time. Secondly, cross-wavelet is applied to calculate the phase difference between the area and intensity series as a function of time. Although it is possible to obtain a better visual picture of the phase relation between the two signals by using EMD, the results agreed with the cross-wavelet analysis when checked.

4.3 MHD wave theory

4.3.1 The sausage mode

We aim to identify MHD sausage modes and as such, it is important to have a theoretical understanding of these modes. Assume, that a magnetic pore is modelled adequately by a cylindrical waveguide with a straight background magnetic field, i.e., $\mathbf{B}_0 = B_0 \hat{\mathbf{z}}$. We note that, for reasons of clarity, in the following discussion the theory does not take into account gravitational effects on wave propagation. However, the influence of gravity may be important for wave propagation in magnetic pores, especially at the photospheric level where the predicted scale height is comparable to the wavelengths of observed oscillations. Therefore we should be cautious with the interpretations. The velocity perturbation is denoted as $\mathbf{v}_1 = (v_r, v_\theta, v_z)$. From the theory of ideal linear MHD waves in cylindrical wave-guides, for the $m = 0$ modes (here, m is the azimuthal wave number) i.e., for axis-symmetric perturbations, the equations determining v_r and v_z decouple from the governing equation of v_θ . Hence, we will have magneto-acoustic modes described by v_r and v_z and the torsional Alfvén mode is described by v_θ . We are interested in the slow magneto-acoustic mode in this paper, so we neglect the v_θ component. The same applies to the component of the magnetic field in the θ -direction. The linear magneto-acoustic wave motion is

then governed by the following ideal MHD equations,

$$\rho_0 \frac{\partial v_r}{\partial t} = -\frac{\partial}{\partial r} \left(p_1 + \frac{B_0 b_z}{\mu_0} \right) + \frac{B_0}{\mu_0} \frac{\partial b_r}{\partial z}, \quad (4.1)$$

$$\rho_0 \frac{\partial v_z}{\partial t} = -\frac{\partial p_1}{\partial z}, \quad (4.2)$$

$$\frac{\partial b_r}{\partial t} = B_0 \frac{\partial v_r}{\partial z}, \quad (4.3)$$

$$\frac{\partial b_z}{\partial t} = -B_0 \frac{1}{r} \frac{\partial (rv_r)}{\partial r}, \quad (4.4)$$

$$\frac{\partial p_1}{\partial t} = -\rho_0 c_s^2 \left(\frac{1}{r} \frac{\partial (rv_r)}{\partial r} + \frac{\partial v_z}{\partial z} \right), \quad (4.5)$$

$$\frac{\partial \rho_1}{\partial t} = -\rho_0 \left(\frac{1}{r} \frac{\partial (rv_r)}{\partial r} + \frac{\partial v_z}{\partial z} \right). \quad (4.6)$$

Here, p is the gas pressure, ρ is the density and $\mathbf{b} = (b_r, b_\theta, b_z)$ is the perturbed magnetic field. We have assumed that the plasma motion is adiabatic. The subscripts 0 and 1 refer to unperturbed and perturbed states, respectively.

Now, assume that the wave is harmonic and propagating and let $v_r = A(r) \cos(kz - \omega t)$. We then obtain the following equations for the perturbed variables,

$$\omega b_r = -B_0 k v_r, \quad (4.7)$$

$$\rho_0 \left(\frac{v_A^2 k^2}{\omega} - \omega \right) A(r) \sin(kz - \omega t) = \frac{\partial}{\partial r} \left(p_1 + \frac{B_0 b_z}{\mu_0} \right) \quad (4.8)$$

$$\rho_0 \frac{\partial v_z}{\partial t} = -\frac{\partial p_1}{\partial z}, \quad (4.9)$$

$$b_z = \frac{B_0}{\omega} \frac{1}{r} \frac{\partial (rA(r))}{\partial r} \sin(kz - \omega t), \quad (4.10)$$

$$\frac{\partial p_1}{\partial t} = c_s^2 \frac{\partial \rho_1}{\partial t} = -\rho_0 c_s^2 \left(\frac{1}{r} \frac{\partial (rv_r)}{\partial r} + \frac{\partial v_z}{\partial z} \right) \quad (4.11)$$

Integrating Equation 4.11 with respect to t and using Equation 4.9 (which is also integrated with respect to t) gives

$$p_1 = c_s^2 \rho_1 = -\frac{\omega \rho_0 c_s^2}{(c_s^2 k^2 - \omega^2)} \frac{1}{r} \frac{\partial (rA(r))}{\partial r} \sin(kz - \omega t). \quad (4.12)$$

The full derivation can be found in Appendix 1. Comparing Equation 4.10 to Equation 4.12 it can be noted that the magnetic field, b_z , and the pressure (density) are 180 degrees out of phase. This depends on the sign of $c_s^2 k^2 - \omega^2$, which is assumed to be positive. Consideration of Equations 4.8, 4.10 and 4.12 leads to the conclusion that v_r is 90° out of phase with b_z and -90° out of phase with p_1 .

The flux conservation equation for the perturbed variables gives the following relation,

$$B_0 S_1 = -b_{1z} S_0, \quad (4.13)$$

where S refers to the cross-sectional area of the flux tube. We conclude that the perturbation of the area is out of phase with the perturbation of the z-component of the magnetic field, hence, the area is in-phase with the fluctuations of the thermodynamic quantities. Perhaps more importantly, we re-write Equation 4.13 as

$$\frac{S_1}{S_0} = -\frac{b_{1z}}{B_0}. \quad (4.14)$$

Hence, if we are able to measure oscillations of a pore's area, we can calculate the percentage change in the magnetic field due to these oscillations (assuming conservation of flux in the pore). This was previously suggested by Grant et al. (2015). Exploiting this relation will allow a comparison to be made between the observed changes in pore area and the magnetic oscillations found from Stokes profiles (e.g. Balthasar et al., 2000). Further, as there are known difficulties with using the Stokes profiles, observing changes in pore area could provide a novel way of validating or refuting the observed magnetic oscillations derived from Stokes profiles. These simplified phase relations were confirmed in a more complicated case by e.g., Moreels and Van Doorselaere (2013) and Moreels et al. (2013), who also derived the phase relations for other linear MHD waves.

By measuring the change in pore area with time, we will also be able to estimate the amplitude of the radial velocity perturbation. The changes in area are related to changes in radius of the flux tube by

$$\frac{S_1}{S_0} = \frac{2r_1}{r_0}, \quad (4.15)$$

where r_0 and r_1 are the unperturbed radius and perturbation of the radius, respectively, assuming the flux tube has a cylindrical geometry. Once a periodic change in radius is identified, the radial velocity of the perturbation can then be calculated using the following relation

$$v_r = \frac{\partial r}{\partial t} = \frac{2\pi r_1}{P}. \quad (4.16)$$

Note, the term “sausage mode” was introduced for waves in magnetic tubes with a circular cross-section. The main property of these waves that distinguishes

them from other wave modes is that they change the cross-sectional area. The cross sectional area of observed pores are typically non-circular. However, it seems to be reasonable to use the term sausage mode for any wave mode that changes the cross-sectional area. Several preceding papers have looked into non-circular, e.g., elliptic shapes, and found the effects to be marginal on the MHD waves within these tubes (see Erdélyi and Morton 2009 and Morton and Ruderman 2011).

4.3.2 Period ratio of standing slow MHD wave

The period of a standing wave in a uniform and homogeneous flux tube is given by $P \approx 2L/nc_{ph}$, where L is the tube length, n is a integer determining the wave mode harmonics and c_{ph} is the phase speed of the wave. This ratio is for ideal homogeneous tubes, however, this is not the case for the solar atmosphere from the photosphere to the transition region. Luna-Cardozo et al. (2012) modelled the effect of density stratification and expansion with height of the fluxtube on the ratio of the fundamental and first overtone periods for a vertical flux tube sandwiched between the photosphere and transition region. Their analysis studied the slow standing MHD sausage mode and assumed a thin flux tube with a small radial expansion with height. They investigated two cases; case one is where the flux tube undergoes weak magnetic expansion with constant density, finding,

$$\frac{\omega_2}{\omega_1} = 2 - \frac{15}{2} \frac{\beta_f}{(6 + 5\beta_f)\pi^2} (\Gamma - 1), \quad (4.17)$$

where ω_i is the period of specific harmonic or overtone (i.e., 1, 2), β_f is the plasma- β at the base of the flux tube and Γ is the ratio of the radial size of the flux tube at the apex to the foot-point. Here, Equation (4.17) is Equation (43) from Luna-Cardozo et al. (2012). Case two is where the flux tube has density stratification but a constant vertical magnetic field, finding,

$$\frac{\omega_2}{\omega_1} = \left[\frac{16\pi^2 + \left(\ln \frac{1 - \sqrt{1 - \kappa_1}}{1 + \sqrt{1 - \kappa_1}} \right)^2}{4\pi^2 + \left(\ln \frac{1 - \sqrt{1 - \kappa_1}}{1 + \sqrt{1 - \kappa_1}} \right)^2} \right]^{1/2}, \quad (4.18)$$

where κ_1 is the square root of the ratio of the density at the top of the fluxtube to the density at the footpoint ($\kappa_1 = (\rho_{apex}/\rho_{footpoint})^{0.5}$). Here, Equation (4.18) is Equation (40) from Luna-Cardozo et al. (2012). Here, the upper end of the flux tube may well be the transition region while the footpoint is in the photosphere. It should be noted

that the form of Equation 4.18 depends on the longitudinal density profile; here,a density profile where the tube speed increased linearly with height was used.

This may or may not model a realistic pore and given the uncertainty of the equilibrium quantities this must be kept in mind in order to avoid over-interpretation. Both Equations 4.17 and 4.18 modelling the frequency ratio of standing oscillations indicate that the ratio of the first harmonic to the fundamental will always be less than two for fluxtube expansion while the density stratification could increase this value. Further, the thin fluxtube approximation is used to derive these equations. Obviously, in a real flux tube, both the density and magnetic stratification would be present at the same time and would alter the ratio. This is not accounted for at the moment. Further, Equations 4.17 and 4.18 are independent of height which may limit the results as it has been suggested that the height to the transition region varies (Tian et al., 2009).

4.4 Results and Discussion

Figures 4.2 and 4.3 show the results of wavelet analysis of the area and intensity time series for the DOT and DST telescopes, respectively. The original signal is displayed above the wavelet power spectrum, the shaded region marks the cone of influence (COI), where edge effects of the finite length of the data affect the wavelet transform results. The contours show the confidence level of 95%.

4.4.1 DOT Pore

There are four distinct periods found in the area time series of the pore; 4.7, 8.5, 20 and 32.6 minutes. The last period is outside the COI due to the duration of the time series, so it has been disregarded. It should be noted that periods of 8, 14 and 35 minutes have been observed in sunspots by Kobanov and Makarchik (2004). This is important as pores and sunspots share a number of common features. The intensity wavelet shows 4 periods of oscillations; 4.7, 8.6, 19.7 and 35 minutes. These periods are similar, if not the same as the period of the area oscillations, which enables a direct comparison of the two quantities. There is significant power that is co-temporal which can be observed in both the intensity and area wavelets.

Using cross-wavelet in conjunction with the EMD allows the verification of the phase difference between the area and intensity signals for each period. These methods show that the phase difference is very close to 0° , *i.e.*, the oscillations are in-phase meaning that they are slow sausage MHD waves. Further, the percentage

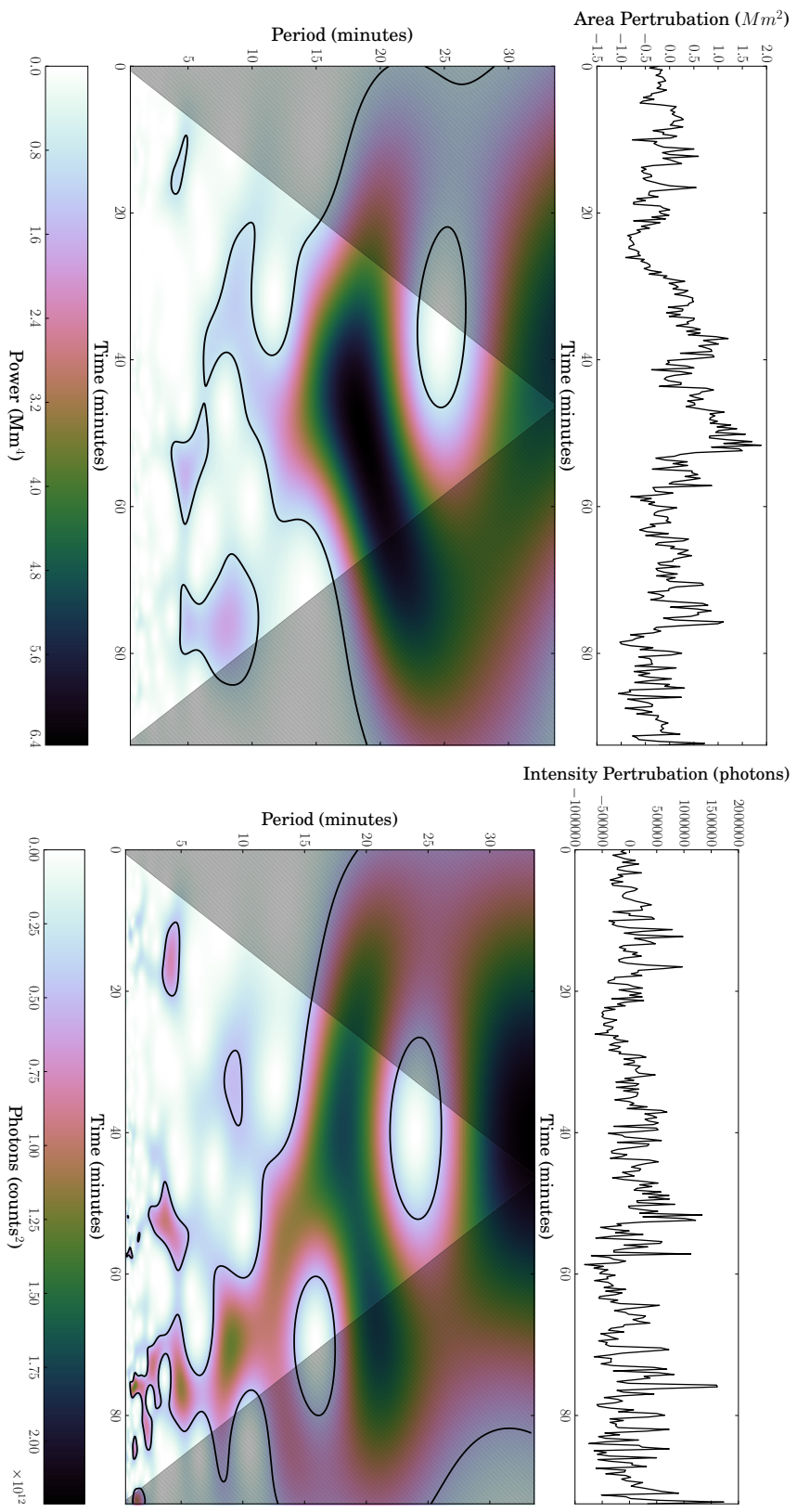


Fig. 4.2 Evolution of the area of the pore observed with DOT (*Upper panels*). The corresponding wavelet power spectrum for a white noise background. The cone of influence is marked as the shaded region and the contour lines show the 95% confidence level (*Lower panels*).

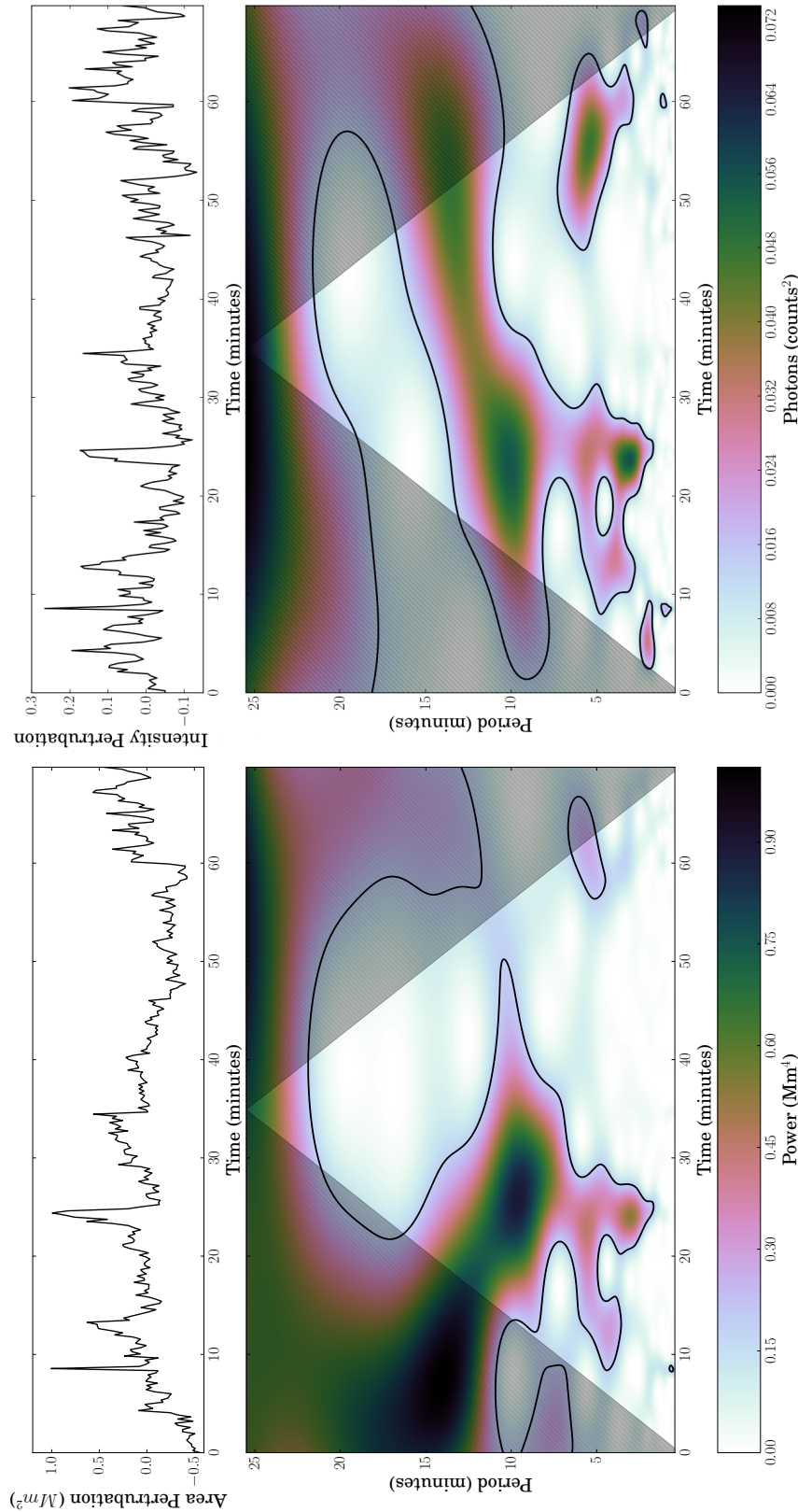


Fig. 4.3 Same as Figure 4.2 but for the pore observed with ROSA. Note that the intensity counts are normalised by the ROSA reduction pipeline (Jess et al., 2010).

change in intensity is also of the same order as reported in Balthasar et al. (2000) and Fujimura and Tsuneta (2009). This suggests, we are most likely observing the same oscillatory phenomena as these previous authors.

We also have to be certain that any change in area we observe is due to the magneto-acoustic wave rather than a change in the optical depth of the plasma. Fujimura and Tsuneta (2009) provide an insight into the expected differences between the phase of magnetic field and intensity oscillations due to waves or the opacity effect. They demonstrate that the magnetic field (pore area) should be in-phase (out-of-phase) with the intensity if the oscillations are due to changes in optical depth. We note that this is the same relationship expected for the fast magneto-acoustic sausage mode. Hence, the identification of the fast magneto-acoustic mode in pores may prove difficult with only limited datasets.

The application of Equations 4.15 and 4.16 require information about the amplitude of the area perturbation. This can be achieved using either an FFT power spectrum or the IMF's amplitude from the EMD analysis. Here, we use EMD for the amplitudes (which are time-average values) and they are $3.87 \times 10^5 \text{ km}^2$, $3.61 \times 10^5 \text{ km}^2$ and $5.90 \times 10^5 \text{ km}^2$ for the oscillations with periods of 4.7, 8.5 and 20 minutes, respectively. It was not possible to find the amplitude of the largest period, as it did not appear in the EMD output. The values of area perturbation translate (using Equation 4.15) to 37, 34 and 56 km respectively for the amplitude of the radial perturbation. Note that the increase in radius is about 100 km meaning the perturbation is only of the order of 1 pixel (at the DOT's resolution).

Using the values above, allows us to calculate the radial velocity perturbation for each period (by means of Equation 4.16). For the periods of 4.7, 8.5 and 20 minutes, we determine the radial velocity perturbation as 0.82 , 0.42 and 0.29 km s^{-1} , respectively. The obtained radial speeds are very sub-sonic as the sound speed is $\approx 10 \text{ km s}^{-1}$ in the photosphere. They are, however, of order of observed horizontal flows around pores.

Further, it is also possible to estimate the percentage change in magnetic field expected from the identified linear slow MHD sausage modes. The percentage change in pore area, hence magnetic field, is found to be

$$\frac{A_1}{A_0} = \frac{b_1}{B_0} \rightarrow 4 - 7\%.$$

For another magnetic pore, the percentage change was found to be similar at 6% (Grant et al., 2015). Let us now assume that the equilibrium magnetic field strength of the pore takes typical values of 1000-2000 G. Then, the amplitude of the magnetic

field oscillations should be 40-140 G. The lower end of this estimated range of percentage change in magnetic field agrees well with percentage changes in the magnetic field obtained using Stokes profiles by, for example, Balthasar et al. (2000) and Fujimura and Tsuneta (2009). However, the upper end of the range, i.e. ~ 140 G, appears twice as large as any of the previously reported periodic variations in magnetic field. This apparent difference could be due to the spatial resolution of the magnetograms averaging out the magnetic field fluctuations. A summary of our findings can be found in Table 4.1.

Now, we estimate the wavelength (wavenumber) for each mode. An important fact needs to be remembered, *i.e.*, the velocity perturbation determined is radial, not vertical. Further, since the waveguide is strongly stratified, we define the wavelength as the distance between the first two nodes, which is the half wavelength of the wave. However, in this regime, the vertical phase speed of the slow sausage MHD wave is the tube speed, which is $c_T \approx 4.5 \text{ km s}^{-1}$ using typical values for the photospheric plasma (Edwin and Roberts, 1983; Evans and Roberts, 1990). For the periods of 4.7, 8.5 and 20 minutes we obtain estimates of the wavelength (wavenumber) as 1269 km ($4.95 \times 10^{-6} \text{ m}^{-1}$), 2268 km ($2.77 \times 10^{-6} \text{ m}^{-1}$) and 5319 km ($1.18 \times 10^{-6} \text{ m}^{-1}$), respectively. Note that these wavelengths are larger than the scale height in the photosphere (≈ 160 km) or the lower chromosphere. For the observed pore, it had an average radius, $a = 1.5 \text{ Mm}$, where $ka = 8, 5, 2$. See Table 4.2 for a summary.

4.4.2 ROSA Pore

There are four distinct periods found in the area time series of the pore observed by ROSA; 2-3, 5.5, 10 and 27 minutes. All of these reported periods are at least at 95% confidence level (or over). A few words about two of the periods have to be mentioned. Firstly, the power of the 2-3 minute period is spread broadly and, as such, it is hard to differentiate the exact period. Secondly, the 10-minute period slowly migrates to 13.5 minutes as the time series comes to its end. The intensity wavelet shows four periods of oscillations; 2-3, 5.5, 10 and 27 minutes. For the pore observed by DOT, the oscillations found in the area and intensity data share similar periods. Also, there is another period that is below the 95% confidence level for white noise at 1-2 minutes at the start of the time series. This is a similar behaviour as found for the DOT pore.

We found that the phase difference between the area and intensity periods is 0° . This means, as before, that these oscillations are in-phase and are interpreted as signatures of slow sausage MHD waves. While we have chosen not to discuss the out-of-phase behaviour, there are small regions of 45° phase difference that has been

DOT	r_1	v_{r1}	$\frac{b_{z1}}{B_0}$	ROSA	r_1	v_{r1}	$\frac{b_{z1}}{B_0}$
Period 1 4.7 mins	37 km	0.82 km s ⁻¹	4.34%	Period 1 2-3 mins	69.1 km	3.03 km s ⁻¹	26.3%
Period 2 8.4 mins	34 km	0.42 km s ⁻¹	4.04%	Period 2 5.5 mins	74.2 km	1.41 km s ⁻¹	28.2%
Period 3 19.7 mins	56 km	0.29 km s ⁻¹	6.60%	Period 3 10 mins	117 km	1.23 km s ⁻¹	44.5%

Table 4.1 The properties of each observed period for the DOT and ROSA data respectively. r_1 is the radial perturbation, v_{r1} is the velocity perturbation and $\frac{b_{z1}}{B_0}$ is the magnetic field perturbation. These quantities are determined by using Equations 4.15 and 4.16.

DOT	λ_z	k_z	$k_z a$	ROSA	λ_z	k_z	$k_z a$
Period 1 4.7 mins	1269 km	$4.95 \times 10^{-6} \text{ m}^{-1}$	8	Period 1 2-3 mins	540-810 km	$7.76-12 \times 10^{-6} \text{ m}^{-1}$	4-6
Period 2 8.4 mins	2268 km	$2.77 \times 10^{-6} \text{ m}^{-1}$	5	Period 2 5.5 mins	1485 km	$4.2 \times 10^{-6} \text{ m}^{-1}$	2
Period 3 19.7 mins	5319 km	$1.18 \times 10^{-6} \text{ m}^{-1}$	2	Period 3 10 mins	2700 km	$2.33 \times 10^{-6} \text{ m}^{-1}$	1

Table 4.2 The wavelength (wavenumber) for each observed period for the DOT and ROSA data respectively. Here, $k = 2\pi/\lambda$ and $\lambda = v/f$, where k is the wavenumber, λ is the wavelength, v is the velocity and f is the frequency.

previously reported (Dorotovič et al., 2014). This needs to be investigated in the future, as the authors are unaware of which MHD mode would cause this behaviour, however, it has been suggested that is due to noise within the dataset (Moreels et al., 2015). As for the DOT pore, the same properties can be obtained for each period observed as within the ROSA pore and is summarized in Table 4.1 and 4.2.

The amplitudes for the area oscillations are $2.29 \times 10^5 \text{ km}^2$, $2.45 \times 10^5 \text{ km}^2$ and $3.87 \times 10^5 \text{ km}^2$ for periods of 2-3, 5.5 and 10 minutes, respectively. The 13.5-minute period is found by the EMD process as well and has an amplitude which is the same as that of the 10-minute period. Again, it was not possible to find the amplitude of the largest period. These then, lead to the radial perturbation amplitude of 69.1, 74.2 and 117 km and the radial velocity perturbation as 3.03 , 1.41 and 1.23 km s^{-1} , respectively. The increase in radius is around 100 km meaning the perturbation is only of the order of 2 pixels (at ROSA's resolution). This means that for each part of the structure, its radius increases by 2 pixels. Once again, the radial velocity perturbations are found to be sub-sonic.

The percentage change in the pore's area, and, thus the magnetic field is given by

$$\frac{A_1}{A_0} = \frac{b_1}{B_0} \rightarrow 25 - 45\%.$$

From the above relations we conclude that the size of the magnetic field oscillation is in the region of 200-400 G. This is a substantial increase when compared to the measurements of the pore detected by DOT, as the amplitudes for these oscillations are of the same order but the cross-sectional area of the pore is an order of magnitude smaller. This suggests that the oscillation strength might be independent of the scale of the structure (Dorotovič et al., 2014).

Once again, we determine the wavelength (wavenumber) for each period, using the tube speed as defined in the previous section. For the periods of 2 – 3, 5.5 and 10 minutes we obtain estimates of the wavelength (wavenumber) as 540-810 km ($7.76 \times 10^{-6} \text{ m}^{-1}$), 1485 km ($3.58 \times 10^{-6} \text{ m}^{-1}$) and 2.2 Mm ($2.85 \times 10^{-6} \text{ m}^{-1}$), respectively. For the observed pore radius, $a = 0.5 \text{ Mm}$, we obtain values of $ka = 2, 1.8, 1.5$ and 1.5 .

4.4.3 Standing Oscillations

With the important understanding that the observed waves are trapped, there is a possibility of them being standing ones. Assuming that the pore can be modelled as a straight homogeneous magnetic flux tube which does not expand with height, the sharp gradients (often modelled as discontinuities) of the temperature/density at the

DOT Period (Mins)	Ratio (P_1/P_i)	Rosa Period (Mins)	Ratio (P_1/P_i)
8.5 mins	-	10 mins	-
4.7 mins	1.81	5.5 mins	1.81
		2-3 mins	3.3-5

Table 4.3 The periods of oscillations as well as the harmonic ratios for the DOT and ROSA magnetic pore respectively. The periods listed here exist at 95% confidence level and are within the COI. Periods greater than 10 minutes have been neglected.

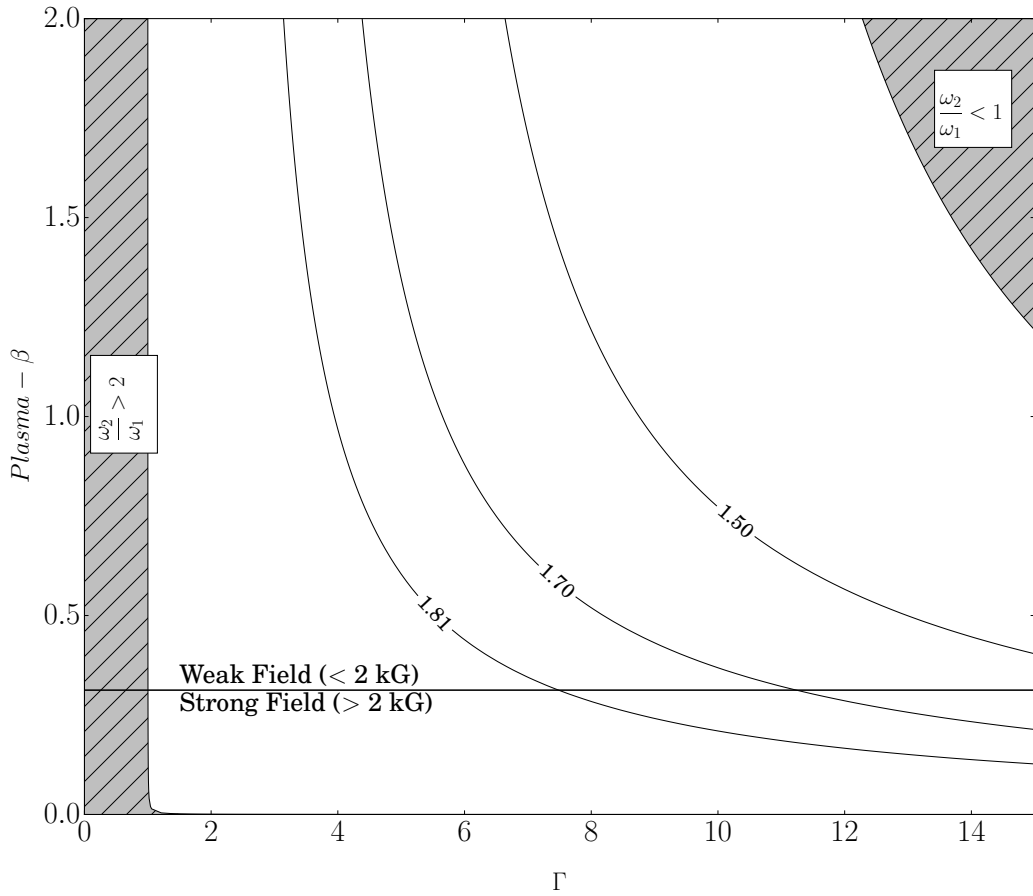


Fig. 4.4 The range of solutions for Equation 4.17. The threaded areas are where the period ratios are either less than one or greater than 2. The horizontal line divides the image into a weak (< 2 kG) and strong (> 2 kG) field regions for the plasma- β . The blue contour lines indicate observed period ratios for this paper and the values within Dorotović et al. (2014).

photosphere and at the transition region form a resonant cavity which can support standing waves (see Fleck and Deubner, 1989; Malins and Erdélyi, 2007).

Calculating the harmonic periods ($P \approx 2L/nc_{ph}$, where L is the distance between the boundaries (2 Mm), n is the harmonic number), a fast MHD oscillation ($c_p \approx 12 \text{ kms}^{-1}$) would have a fundamental period ~ 333 s, while the period of a slow MHD wave ($c_p \approx 5.7 \text{ kms}^{-1}$) would be ~ 700 s. Other slow MHD sausage waves have been observed with phase speeds similar to this (Moreels et al., 2015). The interpretation of the observed waves is that they are slow MHD sausage waves, which in the ideal homogeneous case is the most similar to the observed results, however, it is still different by two minutes. Therefore, the basic assumption of an ideal homogeneous flux tube (constant L , constant c_{ph} etc.) is inadequate to explain the results presented in this paper. There are several further considerations that need to be taken into account. From observations, many magnetic structures are not cylindrical or symmetrical and are often irregular in shape. Further to this, large-scale magnetic structures have been thought to be made up of either a tight collection of small-scale flux tubes or one large monolithic structure (Priest, 1984, and references within). Also, these magnetic structures extend from the photosphere to the transition region which means that the plasma- β will vary by an order of 2 magnitude, which will change the dynamics of the MHD waves considerably. We have also ignored the effect of gravity (*i.e.*, density stratification) (Andries and Cally, 2011; Díaz and Roberts, 2006), as well as the equally important fact that flux tubes expand with height (*i.e.*, magnetic stratification) which alters the ratio of the periods, *i.e.*, $P_1/P_2 \neq 2$ (Luna-Cardozo et al., 2012). All of these effects will further affect the wave dynamics inside flux tubes.

Here, we will ignore periods greater than 10 minutes as shown above, in the ideal homogeneous case, the largest period possible is 11.6 minutes for MHD waves (with the above assumptions). Here, we will consider two effects: the effect of density stratification and magnetic expansion with height in the radial direction. For the first case; Equation (4.18) is calculated with typical density values from the VAL-III C model Vernazza et al. (1981) at the apex (transition region) and footpoint (photosphere) of the flux tube. The VAL-III C model is an estimation of a quiet-Sun region and the interior density ratio between photosphere and transition region of a flux tube need not necessarily differ greatly from that of the exterior atmosphere (see Figures 3 and 1 of Gent et al., 2013 and Gent et al., 2014, respectively). The resulting value for the period ratio in this circumstance is 1.44 (density values are 2.727×10^{-7} and $2.122 \times 10^{-13} \text{ g cm}^{-3}$ for the footpoint and apex respectively). Using the model given by Maltby et al. (1986), which models a sunspot umbra, this period ratio is

1.38 (density values are 1.364×10^{-6} and 9.224×10^{-14} g cm $^{-3}$ for the footpoint and apex respectively). This does not correspond well to the results in this paper, but only for one previously reported result; a highly-dynamical non-radially uniform sunspot (Dorotović et al., 2014). The ratio is substantially smaller than what is detected here, which means the first harmonic should be at ≈ 5.9 minutes. This model does not seem to be applicable to the observational results presented here. The reason for this, the authors believe, is due to the effect of finite radius. The dispersion relation for slow MHD waves in a finite radial fluxtube, shows that the dispersion related to the finite tube radius increases the wave frequency. The shorter the wavelength, the stronger the dispersion effect is. Hence, the relative increase of the first overtone frequency due to the effect of finite radius is larger than that of the fundamental harmonic. This modifies the period of the first harmonic to be higher, which shifts the period ratio to be larger than values that are obtained theoretically in the thin tube approximation.

Figure 4.4 details the various solutions (*i.e.*, period ratio) for Equation 4.17 over a large range of plasma- β and expansion ratio (Γ). It is difficult to estimate how much a flux tube expands with height, therefore, we explore the parameter space widely, taking Γ of 0-15. The values for the plasma- β is divided into strong (≥ 2 kG) and weak (≤ 2 kG) field regions, as the magnetic field of flux tubes hypothesised, will vary from 0.5 kG to 4 kG. The magnetic pores were observed before the launch of NASA's Solar Dynamics Observatory (SDO), so the best magnetic data comes from the Michelson Doppler Imager (MDI) instrument on-board NASA's Solar and Heliospheric Observatory (SOHO). As such, the magnetic field of these pores is hard to know precisely due to their small scale and MDI's large pixel size. However, ground-based observations of similar sized pores reveal magnetic fields ranging from 1 kG to 2.5 kG. The blue contour lines show the parameter space that matches the period ratios reported in this article and the ones in Dorotović et al. (2014). For example, if the plasma- β is around 1, the expansion factor for the three period ratios reported here are around 4, 6 and 9. If we have plasma- $\beta \ll 1$, the expansion ratio starts to increase rapidly.

Once again, this effect can be dominant when the flux tube expands too much, however, it is unlikely that a flux tube would expand by such a large amount. Browning and Priest (1982), for example, suggests that when the internal gas pressure exceeds the external gas pressure, the flux tube becomes unstable and this occurs when the flux tube expands greatly with height.

For the cases presented in this paper, the flux tube has to expand four to six times to have a period ratio that is observed. In a number of numerical simulations that

model these types of flux tubes, the magnetic field expands approximately 4-10 times which happens to be not too dissimilar to our findings (see also Fedun et al., 2011a,b; Khomenko et al., 2008). It should be noted that these estimates for expansion are for flux tubes with magnetic fields that have a field strength less than 2 kG.

Unfortunately, as of yet, little is known about the source of the oscillations analysed in this paper. One possible origin of MHD sausage waves is suggested by e.g. Khomenko et al. (2008) and Fedun et al. (2011a), where magneto-acoustic wave propagation in small-scale flux tubes was modelled using non-linear MHD simulations. One of the results of their simulations is that five-minute vertical drivers can generate a mixture of slow and fast sausage modes in localised magnetic flux tubes that propagate upwards. Furthermore, Fedun et al. (2011b) model the effect of photospheric vortex motion on a thin flux tube, finding that vertex motions can excite dominantly slow sausage modes. However, these simulations need to be developed further, before we may comfortably link them to our assertions.

Another potential source is from mode conversion that will occur at the lower region of the photosphere within sunspots and magnetic pores. For example, Khomenko and Cally (2012), modelled a background sunspot-like atmosphere and solving the non-linear ideal MHD equations for this system, found that the fast MHD wave will turn into a slow MHD sausage wave at the Alfvén-acoustic equipartition level (which is where the sound speed is equal the Alfvén speed) and the reverse is also true. The fast MHD wave to Alfvén conversion occurs higher up where there is a steep Alfvén speed gradient, as the fast MHD wave will reflect from this boundary. Below this level, the MHD waves are fast and above this level, slow MHD waves can be supported. This level occurs at approximately 200 km in their model. The observations used within this paper are thought to form at a height around 250 km. Further, sunspot umbra's are depressed in height and it would likely be the same for magnetic pores. These facts can offer an insight into the formation height of G-band since we believe that we are observing a primary slow acoustic mode modified by the magnetic field i.e., the slow MHD sausage wave.

A word of caution: without LOS Doppler data, it is difficult to know whether the oscillations reported are standing or propagating. The data available for magnetic pores does not cover higher levels of the solar atmosphere such as the chromosphere or the transition region. The data presented here only represents a slice of the flux tube near the photosphere. Future work is needed to acquire simultaneous observations of magnetic pores in several wavelengths in order to sample the solar atmosphere at different heights. With detailed spectral images would allow other LOS quantities such as Doppler velocity and magnetic field to be measured. This

way, the oscillations could be determined confidently as standing or propagating due to their different phase relations.

4.5 Conclusions

The use of high-resolution data with short cadence, coupled with two methods of data analysis (wavelets and EMD), has allowed the observation of small-scale wave phenomena in magnetic waveguides situated on the solar surface. By studying the area and intensity perturbations of magnetic pores, it enables the investigation of the phase relations between these two quantities with the use of wavelets and EMD. The in-phase (0° phase difference) behaviour reveals that the oscillations observed are indicative of slow sausage MHD waves. Further, with the amplitude of oscillations measured, several properties could be estimated; such as the amplitude of the magnetic field perturbation and radial speed of the perturbation. The scale of the magnetic field perturbation that are caused by slow MHD waves are of the order 10% and have radial speeds that are sub-sonic when compared to the sound speed at the photosphere. With the MHD mode of these waves identified, the obtained vertical wavelength indicates that the flux tubes would have a strong reflection at the transition region boundary. Further indicating a chromospheric resonator. Finally, the investigation of the period ratio of the oscillations suggests that the fundamental and first harmonic has been observed within these flux tubes. The period ratio observed coupled with magneto-seismology enabled an expansion factor to be calculated that was in very good agreement to values found in numerical models used for MHD wave simulations.

Chapter 5

The detection of upwardly propagating waves in a magnetic pore¹

¹This chapter is based on Freij, N., Scullion, E. M., Nelson, C. J., Mumford, S., Wedemeyer, S., and Erdélyi, R. (2014). The Detection of Upwardly Propagating Waves Channeling Energy from the Chromosphere to the Low Corona. *The Astrophysical Journal*, 791:61. Reproduced with permission from AAS

5.1 Introduction

How energy is transported from the lower solar atmosphere into the corona is an important question that has yet to be fully answered despite decades of research(Erdélyi, 2004; Erdélyi and Ballai, 2007; Taroyan and Erdélyi, 2009). The complex interactions between strong magnetic fields and powerful flows, the latter created by the interplay of gravity, convection and magnetic forces, leads to a number of dynamic phenomena throughout the atmosphere, such as magneto-hydrodynamic (MHD) waves (Edwin and Roberts, 1983), which are theorised to supply energy into the corona. Strong inhomogeneities and steep gradients of key atmospheric properties (such as temperature and density) can lead to strong reflection of wave energy in the upper chromosphere. It has proved difficult to both observe (Aschwanden, 2006; Jess et al., 2009; Marsh and Walsh, 2006; Mathioudakis et al., 2013; McIntosh et al., 2011; Morton et al., 2012; Parnell and De Moortel, 2012; Taroyan and Erdélyi, 2009; Wedemeyer-Böhm et al., 2012) and simulate (Erdélyi and Fedun, 2007, 2010; Hasan et al., 2005; Peter et al., 2006; Steiner et al., 1998; Vigeesh et al., 2012) the propagation of energy from the lower atmosphere into the corona (De Pontieu et al., 2011, 2007; McIntosh, 2012; Rutten, 2012; Vecchio et al., 2007; Zaqrashvili and Erdélyi, 2009).

The most basic model of MHD theory suggests that three distinct types of waves should manifest in the solar atmosphere; namely slow and fast magneto-acoustic and the widely sought-after Alfvén wave (Banerjee et al., 2007; Jess et al., 2009; Mathioudakis et al., 2013; McIntosh et al., 2011; McLaughlin et al., 2011; Suzuki, 2011). High spatial and temporal resolution observations carried out using modern ground- and space-based instrumentation have revealed a plethora of energetic, incompressible (Aschwanden et al., 1999; De Pontieu et al., 2007; Jess et al., 2009), compressible (Morton et al., 2012), and significantly more complicated (De Pontieu et al., 2011; Wedemeyer-Böhm et al., 2012), oscillations and flows. What has yet to be observed is the direct propagation of energy from the lower regions of the solar atmosphere into the corona raising the question as to whether any of these wave processes are actually heating the outer solar atmosphere. Here, we contribute to addressing this question.

Running penumbral waves (RPWs) were originally thought to be evidence of horizontal wave propagation(Bloomfield et al., 2007; Giovanelli, 1972; Zirin and Stein, 1972) which traced the topology of the local magnetic field (Nye and Thomas, 1974; Zhugzhda, 1973) around large sunspots. Due to this assertion, RPWs have been largely ignored with regards to any potential injection of energy into the corona. More recently, it has been suggested that these events are, in fact, upwardly

propagating waves (UPWs)(Bloomfield et al., 2007; Bogdan and Judge, 2006; Jess et al., 2013), which could facilitate the propagation of non-thermal energy into the corona. Here, we present the first observations of UPWs situated around a pore and demonstrate that these waves can indeed penetrate from the lower solar atmosphere into the corona, potentially making them an excellent candidate for plasma heating within solar active regions (ARs).

I discuss here the propagation of UPWs through the plasma surrounding a large pore structure. By conducting a multi-wavelength, multi-instrument analysis, we are able to trace upward propagating wave-fronts from the chromosphere into the transition region (TR) and corona, estimating key properties such as apparent horizontal and vertical velocities, and non-thermal energy supply. The chapter is organised as follows: Sect.5.2 details the collection and reduction of the data presented; Sect.5.3 describes the analysis of the data and studies the observed UPWs within the AR; Sect.5.4 we summarise and conclude.

5.2 Data Collection and Reduction

The analysis presented here is conducted on AR 11511, which displayed a myriad of complex features during these observations. The ground-based data were obtained using the CRisp Imaging SpectroPolarimeter (CRISP)(Scharmer et al., 2008) instrument, situated at the Swedish 1-m Solar Telescope (SST), on the 22nd June 2012 between 07 : 23 UT and 08 : 28 UT, during a period of excellent seeing. These data have a high spatial resolution of around $0.2''$ ($1'' \approx 725$ km) and a cadence of 2.2 seconds, allowing the small-scale structures of the lower solar atmosphere to be resolved (diffraction-limited) using a narrow-band 0.0269 nm H α filter centred on 656.28 nm. H α line scans were returned for $-0.1032, -0.0774, 0$ and 0.1032 nm. Each frame captured by the SST/CRISP instrument sampled a $68''$ by $68''$ FOV close to the disc centre. The data were reconstructed using the *Multi-Object Multi-Frame Blind Deconvolution* (MOMFBD) technique, giving an overall cadence of 2.2 seconds and a spatial resolution of $0.12''$ (van Noort et al., 2005). We followed the standard procedures in the reduction pipeline for CRISP data (de la Cruz Rodríguez et al. (2015)) which includes the post-MOMFBD correction for differential stretching suggested by Henriques (2012), also see Sekse et al. (2013) for more details.

Finally, co-aligned highly ionised plasma comprising the upper solar atmosphere was observed using the Solar Dynamics Observatory's (SDO) Atmospheric Imaging Assembly (AIA) instrument at a spatial resolution of approximately $1.5''$ and a temporal resolution of 12 seconds.

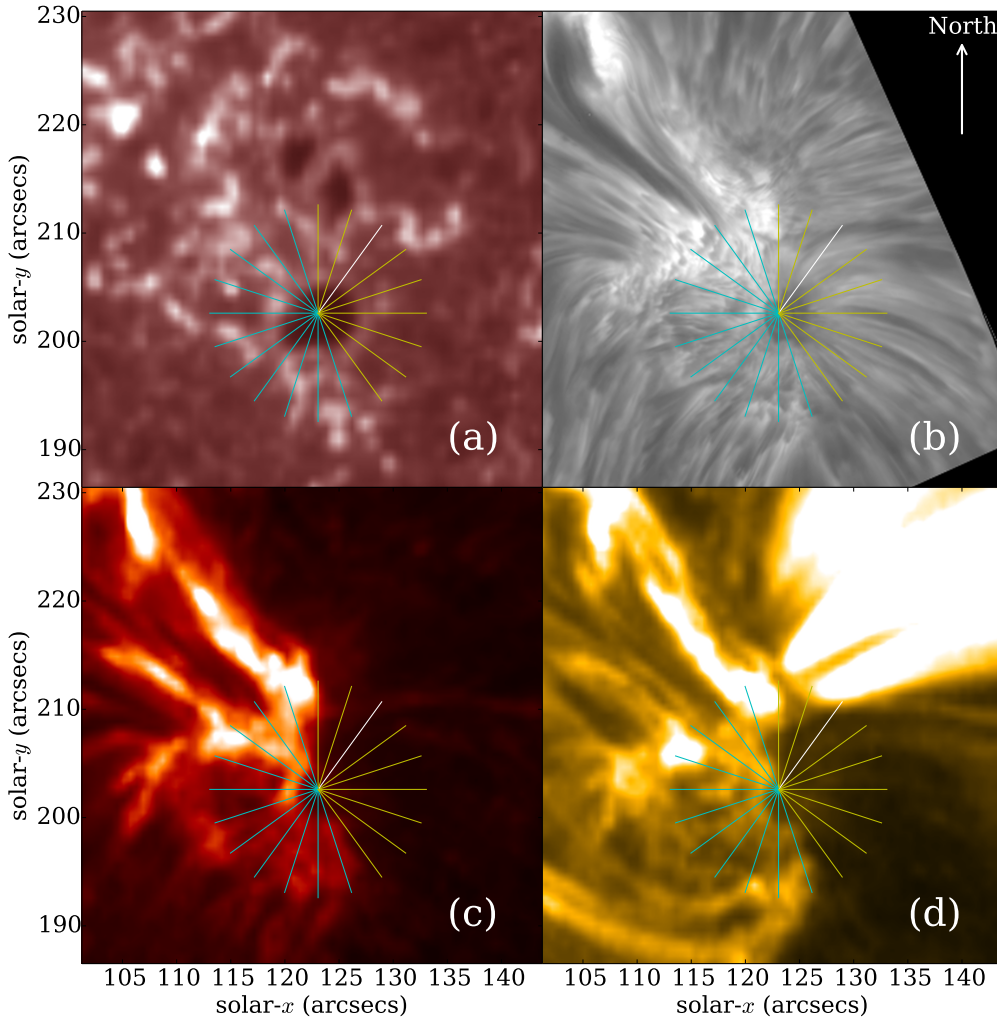


Fig. 5.1 An overview of the field-of-view (FOV) inferred by SST/CRISP and SDO/AIA consisting of: (a) SDO/AIA 170 nm, detailing the photosphere; (b) SST H α 656.28 nm (line core) sampling the chromosphere; the (c) SDO/AIA 30.4 nm filter (TR); and the lower corona detailed by (d) SDO/AIA 17.1 nm. The white line on each image represents the slit used to construct the time-distance diagrams plotted in Figure 5.3. The yellow and cyan lines outline each slit used to investigate UPW behaviour. The yellow slits show where UPWs were observed and cyan slits show no UPWs.

In Figure 5.1, we include a general overview of the FOV analysed here, taken at 07 : 23 UT. The pore of primary interest is located at approximately [123'', 203''] in helioprojective coordinates, and can be easily identified as it is situated underneath the overlaid cyan star symbol. Four images sampled at different heights in the atmosphere are included to give an impression of the three-dimensional structuring evident in this region. The photosphere and chromosphere are sampled by the SDO/AIA 170 nm filter (Figure 5.1a) and the SST/CRISP H α line core (Figure 5.1b), respectively. The dynamic fibril events which appear to protrude away from the large pore in the H α line core, obscure the majority of the large-scale structuring (such as the network) observed within the photosphere. Only in regions where strong vertical magnetic fields are present, such as within the confines of the large pore, does any evidence of the photospheric structuring penetrate into the chromosphere. Finally, the TR and corona are observed through the SDO/AIA 30.4 nm (Figure 5.1c) and 17.1 nm (Figure 5.1d) filters. It should be noted that two small pores are also within the FOV, situated at approximately [123'', 215''], however, they are not evident in the H α line core.

5.3 Results

5.3.1 The observed Active Region

In Figure 5.2, a stacked image outlining the coupling between the lower and upper regions of the solar atmosphere is presented. An extended FOV of the photospheric magnetic field is used as the base (with the SST/CRISP FOV overlaid as the purple box), from which the extrapolated field lines are plotted. Co-aligned photospheric magnetic field data were inferred by the SDO's Helioseismic and Magnetic Imager (HMI) instrument at a spatial resolution of around 1'' and a cadence of 45 seconds. Extrapolations of the magnetic field were then achieved by passing these data into the MPole Interactive Data Language package (Longcope, 1996; Longcope and Klapper, 2002).

We use MPOLE, to determine the 3D coronal magnetic field line connectivity about the FOV as observed by CRISP. MPOLE implements the Magnetic Charge Topology models and the Minimum Current Corona model to derive the coronal field from a set of point charges. In our analysis, the charges are an approximation of an observed photospheric magnetic field. The complete set of charge positions and strengths (fluxes) are contained as a set poles. The poles are extracted from the observations through applying a feature tracking algorithm to HMI magnetograms

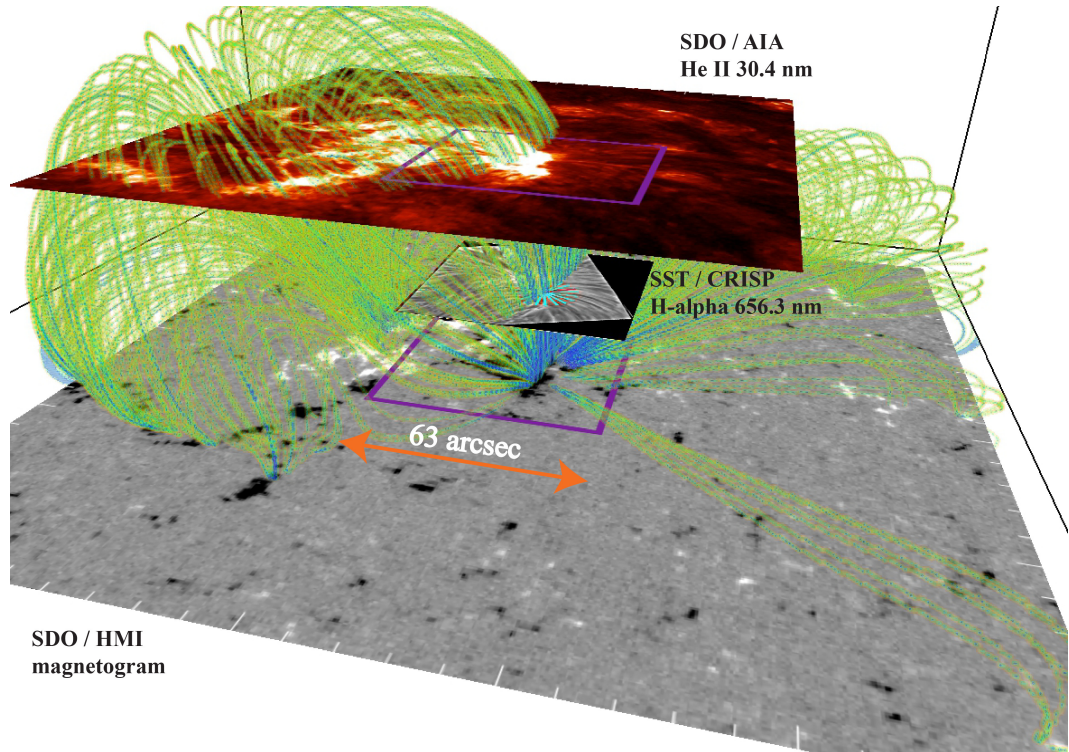


Fig. 5.2 The base layer indicates the magnetic field inferred by the SDO/HMI instrument. The purple box highlights the SST/CRISP FOV which is overlaid. An extended FOV context image from the SDO/AIA 30.4 nm filter is also included. The green lines are the visualisation of the magnetic field extrapolation. A strong correlation exists between these lines and the brighter regions in the SDO/AIA 30.4 nm image underpinning that the extrapolation is a reasonable approximation over such a large height.

of the active region of interest (extended about the CRISP co-aligned FOV by 50 arcsec in both solar-*x* and solar-*y* directions). Feature tracking of regions of positive and negative flux is carried out using YAFTA (Yet Another Feature Tracking Algorithm)(DeForest et al., 2007). Poles are labelled features which are collections of pixels in the magnetogram that are grouped according to criterion such as, spatial size and magnetic field strength. Subsequently, pixels below a threshold in flux density are not grouped, and receive a zero label in the mask. The thresholds are employed to ensure a suitably representative distribution of the magnetic flux concentrations of the active region of interest.

It is immediately noticeable that a non-rotationally symmetric distribution of field lines is present. Over-laid the magnetic field, we stack concurrent images from the SST/CRISP H α , SDO/AIA 30.4 nm, and SDO/AIA 17.1 nm filters. Typically, the formation heights of the H α line core is estimated to be around 1.5 Mm, which agrees to the mid-chromosphere (Leenaarts et al., 2007). The SDO/AIA 30.4 nm and 17.1 nm filters correspond to plasma in the TR and low corona, while SDO/AIA 19.3 nm and 21.1 nm filters correspond to plasma in the corona/hot flare plasma and AR corona, respectively. The chromosphere shows many elongated dark and bright structures surrounding the pore, identified as fibrils. Furthermore, a bright moss-like region to the north of the pore is evident, which corresponds well with regions of high magnetic flux, identified by the extrapolation process. The associated magnetic field from the large pore is observed to penetrate into the chromosphere and potentially higher, and corresponds well with the regions of increased intensity within the 30.4 nm and 17.1 nm filters, supporting that this extrapolation is reasonable over such a large height. The umbra of the two smaller pores do not appear to penetrate into the chromosphere, most likely due to insufficient magnetic flux. It should be noted, however, that UPWs patterns are still seen to propagate above the location of the rightmost pore in the H α line core. This indicates that the magnetic field lines do still expand into the solar chromosphere. In the higher temperature filters, the clarity of the pore fades, and large-scale loop structures, co-spatial with the extrapolated field lines, can be found. On the opposite side of the pore, a region of lower emission is observed in the TR and coronal lines co-spatially with less vertically inclined field lines returned by the magnetic field extrapolation. In the following sections, we discuss the influence of the magnetic field topology on observations of UPWs within this AR. It is imperative to note, that the height of each stacked image in Figure 5.2 was estimated merely for ease of visualisation and should not, therefore, be used as strong evidence that the less vertically inclined field lines do not penetrate into the upper atmosphere.

5.3.2 Upwardly Propagating Waves

The main focus of this chapter is the analysis of UPWs. These events manifest as dark wavefronts, easily identified against the H α background, which appear to propagate radially away from the large pore with a coverage angle of approximately 160°. The coverage of the UPWs is inclusive of both unstructured (such as at the north of the pore) and highly structured regions (on the east of the pore), implying that no specific magnetic topology is required in the H α line core to facilitate the propagation of these waves. It is interesting to note, however, that no UPWs are observed to propagate either south or west from the pore during these observations, implying that a fundamental, but as of yet unknown, factor is limiting either the observation or propagation of waves in this region. A reason for the absence could be the inclination of the magnetic field (see Figure 5.2) and will be expanded upon later in this Section.

In Figure 5.3, we present a series of time-distance diagrams constructed using the white representative slit overlaid on Figure 5.1. The top row of Figure 5.3 plots the raw data extracted for this slit between 07:23:35 UT and 07:41:53 UT for the H α line core (a), the SDO/AIA 30.4 nm filter (b), and the SDO/AIA 17.1 nm filter (c). It should be noted that the start times for the SDO/AIA 30.4 nm and 17.1 nm filters are 9 seconds and 1 second ahead of the SST/CRISP data series, respectively. The UPWs are easily identified within the H α line core (as dark wavefronts) and the SDO/AIA 30.4 nm filter (as bright wavefronts) propagating diagonally away from the pore between 3'' and, approximately, 8''. The apparent horizontal velocity of the observed UPWs appears to decrease as the wavefront propagates away from the source. It has been hypothesised that the decrease in speed may be explained by “the combined action of different frequency modes”(Kobanov et al., 2006), *i.e.*, that an UPW is a superposition of two or more waves with different frequencies. Within the representative H α slit, the detected UPWs slow from $17 \pm 0.5 \text{ km s}^{-1}$ to $12 \pm 0.5 \text{ km s}^{-1}$ at distances of 4'' to 5'', respectively. To conclusively test whether the observed deceleration was a physical property of the waves or a product of using straight slits for analysis, we conducted further research of time-distance diagrams constructed using curved slits, which traced fibril structures within the H α line core. Due to the occurrence of this deceleration in each analysed slit, we conclude that this behaviour of a reduction in apparent velocity is indeed a property of UPWs. Intuitively, as only two factors, namely the actual velocity and the angle of propagation, are required to formulate the apparent velocity, we are able to tentatively suggest that we observe either a physical slow-down of the wavefront or a change in the angle of propagation of these waves.

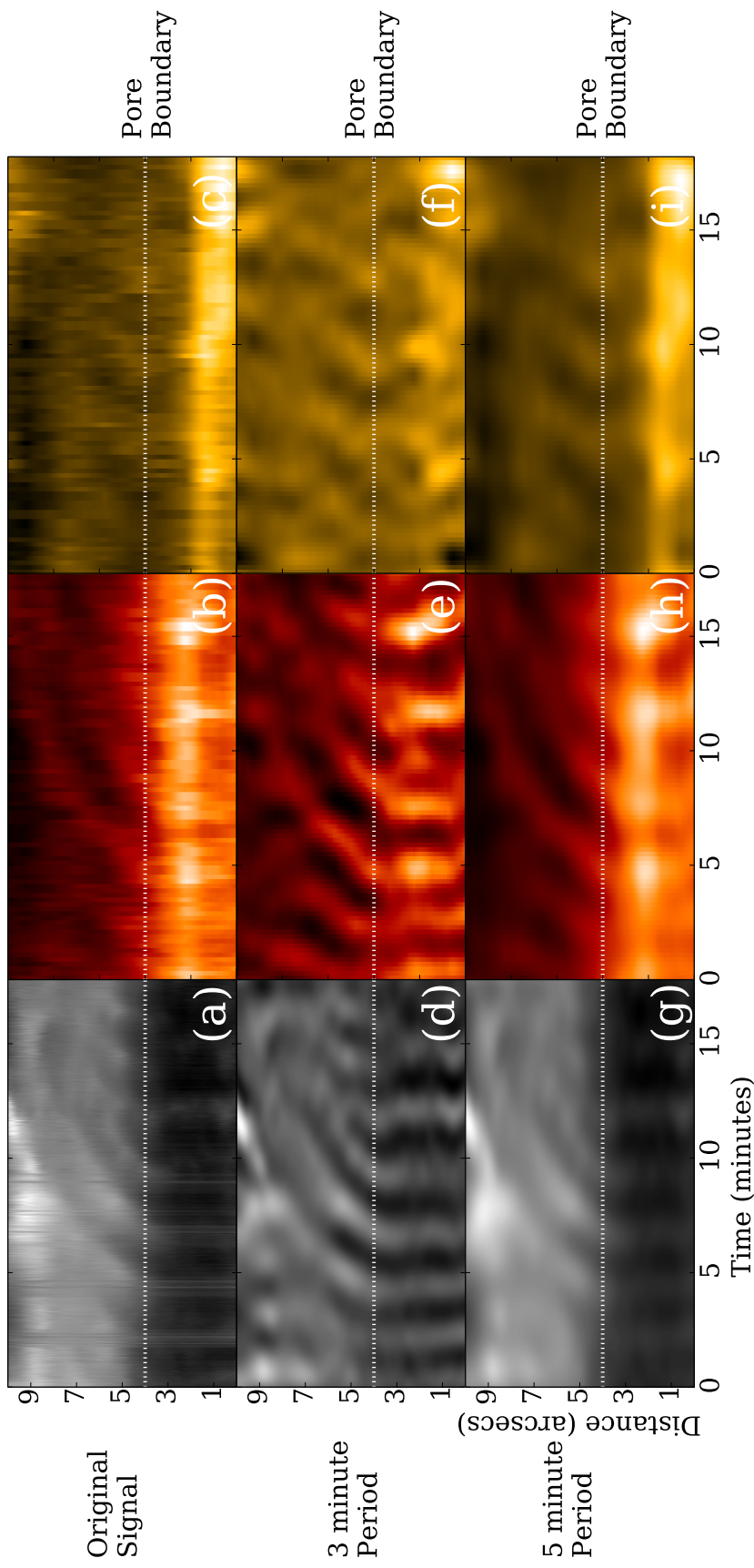


Fig. 5.3 (Top row) Unfiltered time-distance slits for the H α line core (a), SDO/AIA 30.4 nm filter (b), and 17.1 mm filter (c) constructed for the white slit in Figure 5.1. (Middle row) Time-filtered 3-minute FFT output for H α (d), SDO/AIA 30.4 nm (e), and SDO/AIA 17.1 nm (f). (Bottom row) 5-minute FFT output for H α (g), SDO/AIA 30.4 nm (h), and SDO/AIA 17.1 nm (i). The windows used are centred on 3 ± 1.5 mhz (referred to as 5 minutes) and 5 ± 1.5 mhz (referred to as 3 minutes). The white dotted line is the pore boundary, below the line is the pore and above is the background chromosphere.

The spatial occurrence of these waves is a further interesting point which requires discussion. Through the analysis of each cyan slit highlighted in Figure 5.1, investigation into how the behaviour of these waves changes spatially around the pore is feasible. At distances between 2'' and 3'' away from the pore boundary (indicated by the dashed white line in Figure 5.3) for each individual slit, the apparent phase speed ranges from $10\text{-}20 \text{ km s}^{-1}$ (*i.e.*, approximately the sound speed in the chromosphere). As UPWs are observed as single wavefronts, it is possible that the magnetic field topology is influencing the apparent horizontal velocity spatially around the pore. By overlaying the slits in which UPWs are observed onto the interpolated magnetic field, plotted in Figure 5.2, we are able to infer a spatial correlation between the apparently less vertically inclined magnetic fields and the occurrence of UPWs. The observations of such non-radially symmetric wavefronts around a pore, guided by the magnetic field, suggests that the extension of the magnetic field into the solar atmosphere from the pore, is non-axially symmetric. This result poses an interesting question: Does a combination of viewing angle and magnetic field topology limit the potential detection of propagating UPWs around the magnetic waveguide? It is imperative that a future analysis, ideally combining observations and simulations, be undertaken to further test this.

We now direct our investigation towards understanding the potential influence of different wave modes on the raw UPW signals. By employing the FFT technique on each row of the time-distance diagrams (Figure 5.3a-c), the 3-minute period for each wavelength can be isolated from the general wave behaviour. The windows used are Gaussian shaped, centred on $3 \pm 1.5 \text{ mhz}$ (referred to as 5 minutes) and $5 \pm 1.5 \text{ mhz}$ (referred to as 3 minutes) with a width of 2mHz.

The second row of Figure 5.3 depicts the result of such an analysis for the H α line core (d), the SDO/AIA 30.4 nm filter (e), and the SDO/AIA 17.1 nm filter (f). The H α 3-minute component starts off within the pore as an umbral flash-like event and, then, as the wave enters the surrounding atmosphere, moves away at a near constant speed, comparable to the raw data. It is easy to identify, that within the H α line core 3-minute slit, the contrast of the waves against the background is increased when compared to the raw data. This suggests that the 3-minute mode provides a high proportion of the energy carried by UPWs around the pore. A similar behaviour is observed within the SDO/AIA 30.4 nm wavelength, however, no signal is isolated within the SDO/AIA 17.1 nm filter for this slit. Understanding these observations in terms of the physical properties of waves is essential to fully understand the UPW phenomena. Overall, the coverage angle, around the pore, of the 3-minute mode within the SDO/AIA 17.1 nm filter is approximately 50 % lower than the 30.4 nm

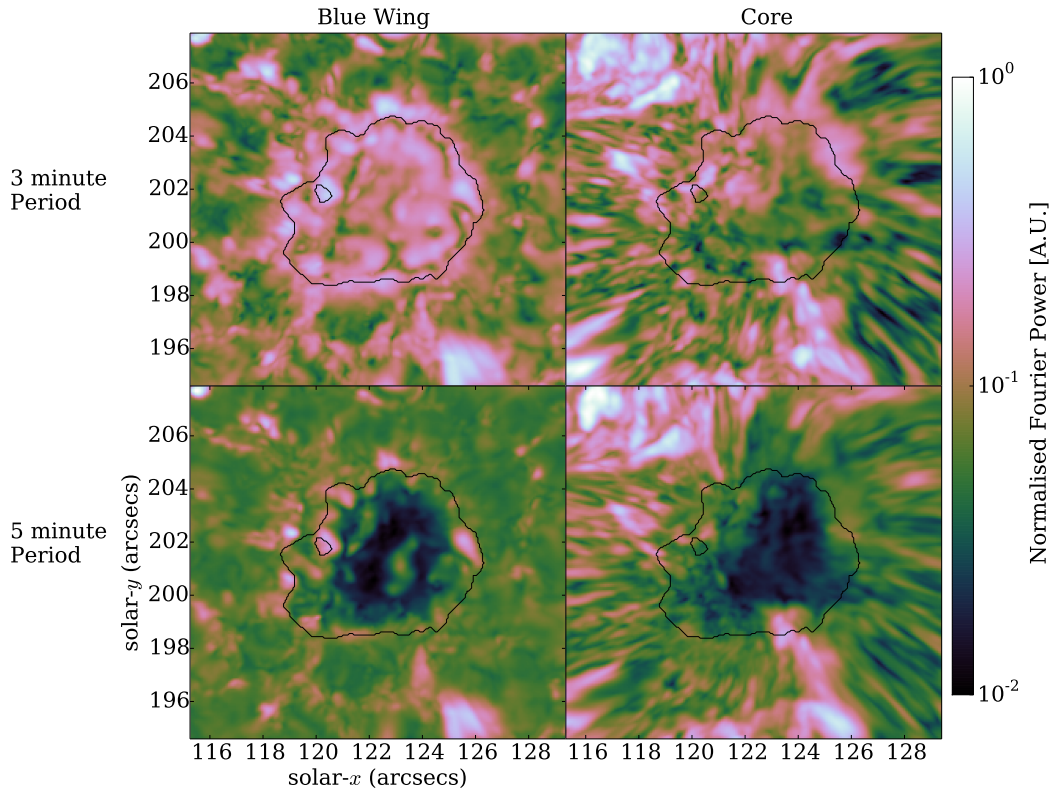


Fig. 5.4 The spatial distribution of normalised Fourier power of the LOS intensity with 3- and 5-minute filter windows. The black contour line highlights the pore boundary as observed within the H α line wings. We depict the: (a) 3-minute filtering of the H α wing; (b) 3-minute filtering of the H α core; (c) 5-minute filtering of the H α wing; (d) 5-minute filtering of the H α core.

filter. The question as to whether this is a result of the waves not propagating into the 17.1 nm passband or a reduced contrast against the background should lend itself to an interesting future study.

Analysis of the 5-minute period (Figure 5.3g-i) allows for further inferences about the nature of these waves to be made. Within the H α line core, the occurrence of the 5-minute mode is limited to regions outside of the pore, potentially due to the dependence of higher frequency modes on the magnetic field inclination(De Pontieu et al., 2004). The phase speed is also reduced by approximately 1-2 km s $^{-1}$ consistently around the pore. As there is more power within the 3-minute mode close to the pore, it is assumed that this comprises the dominant component of the raw wavefront. It is possible, therefore, that the increased influence of the 5-minute component as the wave moves away from the pore could explain the deceleration in raw phase speed, however, further research should be carried out to fully test

this assertion. Within the SDO/AIA 17.1 nm filter, the 5-minute mode has a more defined wave pattern than the 3-minute mode. We are, therefore, able to suggest that the 5-minute mode more easily penetrates into the 17.1 nm passband as has been suggested by previous researchers (De Moortel et al., 2002), potentially providing energy into the TR.

Another method that can be exploited to further understand the physical properties of these waves is a time-delay analysis. We were able to compare both the raw and FFT-filtered data for each wavelength in order to establish whether evidence of a lag exists. By taking into account the different start times for the SST/CRISP and SDO/AIA data, no observable lag was discernible. Therefore, we are able to conclude that either any lag between the signals is less than the cadence of these SDO/AIA data or that, indeed, no lag exists. Should the second hypothesis prove true, it would suggest that these observations support the propagation of a single wave, which occurs within the combined passbands of each of these filters, *i.e.*, around the TR.

By expanding the FFT analysis to the full FOV, we are able to analyse how power is manifested within the local plasma. Figure 5.4 shows the result of applying a 3- and 5-minute period FFT filter on the LOS intensity for the H α line core and far wing (-0.1032 nm). The same process was also applied to the concurrently taken SDO/AIA data, however, the obtained power maps lost their spatial structure and, as such, we were unable to make further conclusions. The black contour depicts the outline of the pore as observed in the photosphere sampled by the H α wing. Within the photosphere (Figure 5.4a,c) the 3-minute power is isolated inside the pore structure; specifically, there appears to be large regions of power tracing the boundary of the pore, apparently analogous to the distribution of power within a sunspot (Reznikova and Shibasaki, 2012; Stangalini et al., 2012). The power in the 5-minute band is minimal in the body of the pore but there is an increase at the pore-photosphere transition boundary corresponding to enhanced *p*-mode power (Mathew, 2008). We interpret the confinement of the power within the pore as evidence that UPWs are driven by *p*-modes propagating vertically within the pore, which acts as a magnetic waveguide.

Finally, we are able to analyse the H α line core. The increase of power especially within the 3-minute, easily observed to the north-east of the pore, corresponds well with the occurrence of UPWs within these data. It is intuitive to suggest that, as the FFT analysis is only applied in the vertical direction, the horizontal component of the UPWs in these regions limits the detection of power. Potentially, the increase in the FFT power observed to the north of the pore, could be indicative of the propagation

of UPWs into the upper solar atmosphere along more vertically inclined magnetic field lines (as observed within Figure 5.2). We interpret the lack of power co-spatially with the UPWs (in the east) as further evidence that the pore's magnetic field has become non-symmetric in the chromosphere. Evidence of the apparent dependence of both the observation of UPWs and the localised power within the plasma around a pore on the potential magnetic field topology, as presented within this chapter, is a key step in fully understanding the complex nature of coupling between layers of the solar atmosphere.

5.3.3 Energy of UPWs

Following the identification and detailed analysis of UPWs around a pore, it is essential to estimate the potential energy carried by these waves into the upper solar atmosphere. Due to the decrease and increase in intensity in comparison to the background plasma for the H α line core and the SDO/AIA filters, respectively, it can be inferred that the wavefront represents an increase in density (Allen, 1947; Leenaarts et al., 2012). By measuring the contrast between the background plasma and the wavefronts, it is apparent that the intensity perturbations are within the linear regime and, therefore, these waves appear to be magneto-acoustic in nature. In order to further this analysis, we assume here that the lack of observed time-delay in these data implies that the lag is below the cadence of these data. Given estimated formation height-differences between the chromospheric H α line core and the SDO/AIA 30.4 nm filter can be estimated to be around 0.5 ± 0.25 Mm, the upward propagation speed can be calculated as 42 ± 21 km s $^{-1}$. This speed is close to previous estimates of the fast speed in the chromosphere (Morton et al., 2012). It should be noted, that this corresponds well with previous results, which suggest that p -mode oscillations, which appear to drive these UPWs, are converted to fast modes (Vigeesh et al., 2012). The combination of these factors allows us to suggest that one of the most likely interpretations of these observations is that UPWs are *fast sausage* waves.

With the wave type being identified, it is now possible to calculate the estimated non-thermal energy for these waves. It is possible to estimate the energy flux at each pixel based on linearised MHD theory (e.g. Kitagawa et al., 2010). The equation for the total energy flux of the fast MHD sausage wave is

$$E_{wave} = \sum_{i=1}^N \rho_0 [\tilde{I}_i / I_0]^2 c_{ph}^3, \quad (5.1)$$

where \tilde{I}_i is the intensity perturbation for each pixel, I_0 is the background intensity, c_{ph} is the phase speed of the sausage wave, ρ_0 is the background density. We sum over each pixel which is part of the wave, giving us the average energy for that wave. Since the wave is a fast MHD sausage wave, the phase speed is c_{fast} which is the local fast speed, however, since the ratio of the Alfvén to the sound speed is $\gg 1$, the Alfvén speed is the dominant value in the fast speed calculation. This assumes that the plasma is optically thin (intensity is proportional to density), which is true for the coronal lines however, not the case for H α .

This analysis leads to energy estimates of the order of 150 W m^{-2} for the wavefronts in the H α line core. These values drop by two orders of magnitude within the SDO/AIA filters. These energy flux values are about a factor of 100 less than reported for other abundant sausage wave events in the chromosphere (Morton et al., 2012), however, they still comprise an important fraction of the energy flux required to heat the local quiet (Wedemeyer-Böhm et al., 2012) and active corona (Aschwanden et al., 2007), respectively. It should be noted, that these estimates are influenced by a number of observational factors, such as attenuation in the telescopic apparatus, changes in light levels throughout these data, and the angle of observation, to name a few. We do, however, suggest that during the period of these observations, there are approximately constant seeing conditions and, therefore, these energy estimates should be consistent. Magnetic pores cannot heat the entire corona, but can contribute to heating the local corona that is above and near the pore. The value for the energy flux is for the region where we can observe the UPWs and the most logical case is that UPWs occurs across the entire pore but are difficult to observe due to the local solar atmosphere. This should raise the value for the energy flux that has been obtained.

5.4 Discussion

The results presented in this chapter support the assertions that waves propagating radially away from concentrated magnetic waveguides (such as pores and sunspots) in the solar photosphere have significant vertical components that give rise to the illusion of horizontal propagation. The magnetic field reconstruction (as seen in Figure 5.2) gives us a useful insight into the non-radially symmetric nature of this pore and, specifically, how the apparent topology of the magnetic field influences UPWs. The case that RPWs are in fact UPWs that travel along the field lines is mounting (Bloomfield et al., 2007; Jess et al., 2013). Here, strong evidence is presented that energy from p -modes in the lower solar atmosphere travels directly

upwards into the TR and lower corona. It has been reported that there is absorption of power at the boundary of the umbra-penumbra for a sunspot (e.g. Gosain et al., 2011). Here, we observe enhanced power at the boundary of the pore at both three and five minutes, while in the chromosphere, where UPWs are observed, there is a reduction of power. As the energy from the acoustic *p*-modes is converted into MHD waves along the flux tube, the period of the *p*-mode becomes three minutes and traces the magnetic field. When the wave travels into the TR and solar corona, there is decrease of the wave period. Rudimentary energy flux calculations reveal that these waves are able to contribute to heating the local corona, however, how much they contribute requires further study.

From this primarily wave-based study of the solar atmosphere we deduce that, in the outside environment surrounding the pore, the magnetic field of the pore becomes non-symmetric. The non-symmetric magnetic field appears to be integral in allowing UPWs to be observed, however, whether these events occur in other regions around the pore but are undetected, requires further study. Further investigation is also required to fully assess whether the lack of UPW signal within some regions around the pore is a consequence of seeing or an, as of yet unascertained, physical property (such as the cut-off frequency). A possible interpretation of these waves is a singular wavefront observed in multiple pass bands, data from a wider range of sources should help answer these. This calls for an extensive investigation using detailed spectropolarimetry (ground-based) data to resolve the issue but also to determine the consequence of changing the LOS (i.e on the limb) on the observation of UPWs. We have shown that the complex lower solar atmosphere, which does act as a powerhouse in the heating of the outer atmosphere, can in fact be further understood through a purely wave-based investigation.

Chapter 6

Conclusion

6.1 Overview of the thesis

In this Thesis, the results of two-dimensional image analysis of sunspots and magnetic pores in the lower solar atmosphere is detailed. These results are compared to theoretically derived results and indicate the ubiquitous presence of slow MHD sausage waves in magnetic structures that inhabit the solar surface. In Chapter 2, the method used to measure the cross-sectional area and total intensity of the magnetic structures is analysed. This is in order to understand what effect this method has on the results of the signal analysis, which is important to reduce bias. In Chapter 3, this method is applied to several magnetic structures. The results indicate the presence of slow MHD sausage waves. This comes from the phase relations found using the signal analysis methods covered in Chapter 2. In Chapter 4, the previous method is applied further, on two magnetic pores. The method was extended by extracting the amplitude of the observed oscillations. This allowed the usage of magneto-seismology in order to calculate several properties of the waves as well as information on the background properties of these magnetic flux tubes. In Chapter 5, the focus shifted from analysing the cross-sectional to the analysis of a Running Penumbral Wave event in a magnetic pore. RPWs are typically observed in sunspot penumbrae, however it was observed emanating from a magnetic pore. This analysis showed that RPWs are most likely an upwardly propagating wave. These events are able to deliver a small amount of energy into the local corona.

6.2 Summary of Results

In Chapter 2, after the summary of signal analysis methods, there was an investigation on the principle method that is used to contour magnetic structures. This was undertaken in order to understand if the method adds a bias to the results. To do this, high quality ground-based data was used from the Dunn Solar Telescope (DST), using two instruments that are installed, the *Rapid Oscillations in the Solar Atmosphere* (ROSA) and the *Interferometric Bidimensional Spectrometer* (IBIS). There are two datasets, one for each instrument, with the telescope pointed at a magnetic pore and a sunspot for ROSA and IBIS respectively (see Figure 2.4). Since both sunspots and magnetic pores are analysed within this thesis, it was important to study the method on both types of magnetic structures. To start, both structures were contoured using a range of sigma multipliers, 3, 3.5, 4 and 4.5 and 2, 2.5, 3, 3.5 for the sunspot and magnetic pore respectively. The standard deviation values used came from a background box of quiet Sun, i.e., a region of the photosphere that contains

no magnetic features. The reason for this difference in sigma multipliers is due to the lack of a good quiet Sun region within the IBIS dataset. Figure 2.5 shows this clearly with the histograms shown on the right column. This had the result of increasing the sigma multipliers. Analysing the cross-sectional area signals using the wavelet transform revealed the range of periods within these magnetic structures. The range of periods found did not vary with the sigma value used, but what did vary was the strength of the detected periods (see Figure 2.6 and Figure 2.7). Thus, it is important to contour the magnetic structures by taking into account the structures's intensity distribution, as this makes choosing a sigma multiplier an easier and more robust choice than choosing a random percentage of the background intensity. Further, this implies that for the current range of ground-based solar telescopes, that the limiting factor for cross-sectional area oscillations is the resolution. This resolution has been fixed for the past couple of years and until Daniel K. Inouye Solar Telescope (DKIST) data becomes available, the range of sigma multipliers can vary without fear of biasing the results. Finally, since the phase relations are used to identified waves modes using Table 1.1. The wavelet transform offers a good insight into the phase difference between two signals. This was also checked with regards to the different sigma multipliers. It was found that there was no major effect as one varies sigma as it would be expected. There were small regions that were different due to the cross-sectional signals varying but nothing that changed the results.

In Chapter 3, the method detailed previously in Chapter 2 is applied to three magnetic structures. These are two sunspots and one magnetic pore (seen in Figure 3.1). The data used here came from the Dutch Open Telescope (DOT) and the Swedish Vacuum Solar Telescope (SVST). These were detailed in Chapter 2 and also within Chapter 3. While these telescopes are quite old and now out of service, they offer good quality data. By contouring these magnetic structures, using a sigma multiplier of 2.5, a range of periods were observed. Using both the wavelet transform and the Empirical Mode Decomposition (EMD), which can be seen in Figure 3.3,3.4,3.5 and 3.6, the range of periods found ranged from 2 minutes and up to 40 minutes. Many of these cross-sectional area periods overlap with line-of-sight (LOS) oscillations found in sunspots before. However, the link between them has not been established. From the signal analysis, the phase difference between the cross-sectional area and total intensity were mostly zero degrees. With the phase relations from Table. 1.1, it is possible to identify these oscillations. This indicates that these oscillations are slow MHD sausage waves. This implies that there is a prevalent amount of these waves in the magnetic structures in the photosphere. On a side note, there were small regions of out-of-phase but more interestingly, 45 degrees.

There is no theory that explains this phase difference, but whether this exists or is a signature of noise is unknown at this time. Finally, whether the oscillations are propagating or are standing is an open question, since it is not possible to know this by using just the cross-sectional area and total intensity phase relations. It should be noted that the periods of the observed oscillations, when the period ratios are calculated assuming the largest period is the fundamental, the period ratios give anecdotal evidence for standing harmonics. Further investigation is required to clarify this point.

In Chapter 4, two further magnetic pores are studied. This time, using more data from the DOT coupled with DST/ROSA which has an increased resolution than the previously used datasets (see Figure 4.1). Taking the method discussed in Chapter 2 and used in Chapter 3, both magnetic pores again show oscillations within their cross-sectional area signals (see Fig 4.2 and 4.3). Due to the shorter nature of these datasets, the periods found are shorter, they range from 2 minutes to 20 minutes. The phase relations once again indicate that these oscillations are slow MHD sausage waves. However, the results within this chapter were taken further. Using linear ideal MHD theory, it is possible to derive equations that will allow the calculation of the radial displacement speed of the oscillation as well as the magnetic field change of the structure due to the oscillation. To achieve this, the amplitude of the oscillations was required and the Fast Fourier Transform (FFT) was used to provide this. The radial displacement speeds were calculated to be within the range of 0.3 km s^{-1} to 3 km s^{-1} . Further, the magnetic field change was calculated to be from 5% up 30%. These results are stated within Table 4.1. The magnetic field change for the magnetic pore observed with ROSA is much larger than the magnetic pore observed in DOT. The reason is that the amplitude of the oscillations is of the same order for both magnetic pores despite that the ROSA magnetic pore has a much smaller cross-sectional area. Therefore, with the MHD wave type known, it is possible to estimate the phase speed for this wave type within a typical magnetic flux tube. This allows the calculation of the wavelength for the observed oscillations (see Table 4.2). The calculated wavelengths add more evidence to the anecdotal evidence shown in Chapter 3. There is a picture emerging that these oscillations could be standing harmonics supported within these magnetic flux tubes. If the assumption that these are standing harmonics is taken, using magneto-seismology it is possible to estimate the expansion factor of the flux tubes. This is the ratio of the radius at the base of the flux tube to the radius at the top of the flux tube. In this case, it is from the photosphere to the transition region. Table 4.3 lists the period ratios of the observed oscillations for the two magnetic pores. This forms the base to calculate

the expansion factor. The expansion factor is dependent on the plasma- β at the base of the flux tube and while it is not possible to know this value, it can be assumed to be around 1 for flux tubes that are within the photosphere. The results of this can be seen within Figure 4.4, which gives a factor that ranges from 4-8 for the magnetic structures analysed within this thesis. These numbers are not too dissimilar to the expansion factors for flux tubes used within MHD wave simulations.

In Chapter 5, the focus shifts from the analysis of the cross-sectional area of magnetic structures to Running Penumbral Waves (RPWs). RPWs have been observed in sunspots since the 1970's as intensity fronts propagating radially outwards from the outer umbra into the penumbra. Excellent seeing data from the Swedish Solar Telescope (SST) using the *CRisp Imaging SpectroPolarimeter* (CRISP) instrument was combined with co-aligned and co-temporal data from the *Atmospheric Imaging Assembly* (AIA) instrument onboard the Solar Dynamics Observatory (SDO) satellite (see Figure 5.1). The result was the first direct imaging of RPWs in a magnetic pore in the H α line core. The whitelight images show no penumbral structure in the photosphere for the observed magnetic pore. Further, the repeat period as well as the horizontal speed is typical of RPWs that have been observed before within sunspots. The RPWs can be seen to emanate from the magnetic pore radially outwards, however, it is not concentric as RPWs that are commonly observed within sunspots. These results came from slit analysis around the magnetic pore (see Figure 5.1 and 5.3). The RPWS are confined to a small region, which is a quiet part of the chromosphere. The waves do not appear to propagate in the region with large static fibrils and regions with dynamic fibrils. The answer from a magnetic field extrapolation (Figure 5.2) which suggests that the field where the RPWs are observed is more radial (i.e., horizontal to the surface) than other parts of the magnetic field. This fact coupled with previous research that indicates that RPWs are in fact Upwardly Propagating Waves (UPWs), is the final step in confirming this. Further, the UPWs were observed with SDO/AIA lines that sample the transition region and low corona, which suggests that UPWs are reaching the higher parts of the solar atmosphere. Mode identification for RPWs has been a difficult topic. Previous studies and most theoretical understanding of RPWs implies that they are slow magneto-acoustic waves. However, in the case presented within Chapter 5, we suggest that the RPWs/UPWs are actually fast magneto-acoustic waves, since the wave appears as dark and light fronts, which is a change in intensity which we conclude is a change in density implying a compressive nature to this waves. A time lag analysis between the H α slit and the SDO/AIA slits gives us a result of less than 12 seconds, i.e., the lag is less than the cadence of SDO/AIA. So the best assumption

that can be made is that the lag is at that cadence (12 seconds). This gives the low phase speed estimate, but the result suggests that the UPW phase speed is greater than the sound and Alfvén speed (assuming typical chromospheric physical values) which means it is a fast wave. However, this is the first report that of a RPW/UPW as a fast mode. With the wave mode identified, the next was the calculation of the energy of the observed waves. The energy is calculated to be around 150 W m^{-2} , which is enough to heat the quiet Sun corona but not an active region corona. This value has been found by another study for cross-sectional area oscillations in the low chromosphere. So overall, these waves have a small but important contribution to corona heating.

6.3 Future Work and Questions

This is always a tricky subject. With any body of work, there are always unanswered questions or gaps in knowledge that ideally should be filled. As such, this thesis does not offer a full view of MHD sausage waves in sunspots and magnetic pores.

Firstly, in Chapter 2, the method used to contour the magnetic structures was analysed. However, it was limited to low lying photospheric wavelengths. This would be expanded to cover other wavelengths which sample up into the chromosphere. Studying how the cross-sectional area oscillations change as a function of height would be an important next stage for this research. In order to map how the amplitudes change with height, if the phase difference varies and if detected periods at one height exist within another height. However, as one moves upwards in the solar atmosphere, the boundary between a magnetic structure and the background atmosphere becomes harder to distinguish, so the analysis in Chapter 2 would need to be refined with multiple heights to investigate any pitfalls with layered datasets. Further to this, the current range of ground-based and space-based solar data has approximately the same resolution and this limit will be around for another two years. This is a problem since the results are inherently dependant on this as this fixes the lower limit of any observations, especially when it comes to detecting perturbations. With DKIST, as well as Solar-C, this limit will be reduced. Thus, attempting this analysis on solar data from the next generation of solar telescopes would be a future extension of this work. Finally, in Chapter 4, the phase speed of the MHD wave was calculated from typical background properties. Thus, the results that came from that are determined by those properties. Further work would ideally employ magneto-seismology in order to calculate the phase speed of the detected oscillations. Normally, this is possible using multiple heights since a time

lag could be calculated with this method, as the height between wavelengths is known approximately. However, research (Moreels et al., 2015) have been published that makes it possible to do this with only the amplitude of the oscillations. This would be a further extension to the work in Chapter 3 and 4.

Secondly, Chapter 2 detailed the signal analysis methods employed within this thesis. While these methods were useful and achieved the overall goals for each chapter, the field of signal analysis is ever evolving. For example, the wavelet transform has had numerous papers published which extend the algorithm to account for power bias at lower periods (Liu et al., 2007; Velleda et al., 2012) as well as being able to discern if the signal is standing or propagating (Sych and Nakariakov, 2008). The Empirical Mode Decomposition has been extended, adding a step to the method where it does an ensemble averages (Wu and Huang, 2009), better methods to deal with the edge effects with the spline fit (Zeng and He, 2004) as well as improved stopping criterion (Huang and Wu, 2008). It is important that the methods used to analyse signals and extract phase relations and amplitudes be made robust in order to be certain in the period, phase and amplitudes of any oscillations found. If magneto-seismology requires these quantities to calculate the background properties of flux tubes, it is vital that any signal analysis method used is as robust as possible.

Finally, the observed UPWs within the magnetic pore is an interesting avenue of wave research. Here, there are many questions that need to be answered. To start, this observation indicated that the UPW events were fast sausage modes needs to be squared with the current literature. Either the interpretation is correct and UPWs can be either fast or slow waves or the analysis is incorrect. Further ground-based observations of magnetic pores would need to be conducted in order to understand UPWs within these structures. The author is only aware that RPWs have been only observed in sunspots , is the difference in wave mode due to a difference between sunspots and magnetic pores? Does the presence of the penumbra cause this or would it be that the plasma- β varies in a pore differently such that mode conversion leads to a fast magnetic-acoustic wave instead of a slow magnetic-acoustic wave? In Chapter 5, the region where the waves were observed was a small region of quiet chromosphere. Does the surrounding chromospheric atmosphere dictate if UPWs can be observed? Generally, symmetrical sunspots display concentric and clear RPWs, is that due to the magnetic field topology of the sunspot being much stronger than a magnetic pore, thus the observation of UPWs allows us to infer the magnetic field topology around sunspots and magnetic pores? Finally, do UPWs have a common source with the LOS oscillations and cross-sectional area oscillations observed in these magnetic structures, or are they the same wave that can be observed in several

different ways? Solar physics has a long way to go and so does the research presented within this Thesis.

References

- Alfvén, H. (1942). Existence of Electromagnetic-Hydrodynamic Waves. *Nature*, 150:405–406.
- Allen, C. W. (1947). Interpretation of Electron Densities from Corona Brightness. *Monthly Notices of the Royal Astronomical Society*, 107:426.
- Andries, J., Arregui, I., and Goossens, M. (2005a). Determination of the Coronal Density Stratification from the Observation of Harmonic Coronal Loop Oscillations. *The Astrophysical Journal, Letters*, 624:L57–L60.
- Andries, J. and Cally, P. S. (2011). On the Dispersion and Scattering of Magnetohydrodynamic Waves by Longitudinally Stratified Flux Tubes. *The Astrophysical Journal*, 743:164.
- Andries, J., Goossens, M., Hollweg, J. V., Arregui, I., and Van Doorsselaere, T. (2005b). Coronal loop oscillations. Calculation of resonantly damped MHD quasi-mode kink oscillations of longitudinally stratified loops. *Astronomy & Astrophysics*, 430:1109–1118.
- Andries, J., van Doorsselaere, T., Roberts, B., Verth, G., Verwichte, E., and Erdélyi, R. (2009). Coronal Seismology by Means of Kink Oscillation Overtones. *Space Science Reviews*, 149:3–29.
- Aschwanden, M. J. (2006). Coronal magnetohydrodynamic waves and oscillations: observations and quests. *Royal Society of London Philosophical Transactions Series A*, 364:417–432.
- Aschwanden, M. J., Fletcher, L., Schrijver, C. J., and Alexander, D. (1999). Coronal Loop Oscillations Observed with the Transition Region and Coronal Explorer. *The Astrophysical Journal*, 520:880–894.
- Aschwanden, M. J., Winebarger, A., Tsiklauri, D., and Peter, H. (2007). The Coronal Heating Paradox. *The Astrophysical Journal*, 659:1673–1681.

- Balthasar, H. (1999). Temporal fluctuations of the magnetic field in sunspots. *Solar Physics*, 187:389–403.
- Balthasar, H., Collados, M., and Muglach, K. (2000). Oscillations in a solar pore. *Astronomische Nachrichten*, 321(2):121–127.
- Banerjee, D., Erdélyi, R., Oliver, R., and O’Shea, E. (2007). Present and Future Observing Trends in Atmospheric Magnetoseismology. *Solar Physics*, 246:3–29.
- Basu, S., Chaplin, W. J., Elsworth, Y., New, R., and Serenelli, A. M. (2009). Fresh insights on the structure of the solar core. *The Astrophysical Journal*, 699(2):1403.
- Bloomfield, D. S., Lagg, A., and Solanki, S. K. (2007). The Nature of Running Penumbral Waves Revealed. *The Astrophysical Journal*, 671:1005–1012.
- Bogdan, T. J. and Judge, P. G. (2006). Observational aspects of sunspot oscillations. *Royal Society of London Philosophical Transactions Series A*, 364:313–331.
- Bonet, J., Márquez, I., Muller, R., Sobotka, M., and Roudier, T. (2005). Phase diversity restoration of sunspot images. *Astronomy & Astrophysics*, 430(3):1089–1097.
- Browning, P. K. and Priest, E. R. (1982). The structure of untwisted magnetic flux tubes. *Geophys. Astro. Fluid.*, 21:237–263.
- Cameron, R., Schüssler, M., Vögler, A., and Zakharov, V. (2007). Radiative magnetohydrodynamic simulations of solar pores. *Astronomy & Astrophysics*, 474(1):261–272.
- Cavallini, F. (2006). Ibis: A new post-focus instrument for solar imaging spectroscopy. *Solar Physics*, 236(2):415–439.
- Chorley, N., Foulon, C., Hnat, B., Nakariakov, V. M., and Shibasaki, K. (2011). Period persistence of long period oscillations in sunspots. *Astronomy & Astrophysics*, 529:A123.
- Chorley, N., Hnat, B., Nakariakov, V. M., Inglis, A. R., and Bakunina, I. A. (2010). Long period oscillations in sunspots. *Astronomy & Astrophysics*, 513:A27.
- Christopoulou, E. B., Georgakilas, A. A., and Koutchmy, S. (2000). Oscillations and running waves observed in sunspots. *Astronomy & Astrophysics*, 354:305–314.

- Christopoulou, E. B., Skodras, A., Georgakilas, A. A., and Koutchmy, S. (2003). Wavelet Analysis of Umbral Oscillations. *The Astrophysical Journal*, 591:416–431.
- Cooley, J. W. and Tukey, J. W. (1965). An algorithm for the machine calculation of complex fourier series. *Mathematics of computation*, 19(90):297–301.
- Cooper, F. C., Nakariakov, V. M., and Tsiklauri, D. (2003a). Line-of-sight effects on observability of kink and sausage modes in coronal structures with imaging telescopes. *Astronomy & Astrophysics*, 397:765–770.
- Cooper, F. C., Nakariakov, V. M., and Williams, D. R. (2003b). Short period fast waves in solar coronal loops. *Astronomy & Astrophysics*, 409:325–330.
- Cox, A. N., Livingston, W. C., and Matthews, M. S. (1991). *Solar interior and atmosphere*. University of Arizona Press.
- de la Cruz Rodríguez, J., Löfdahl, M. G., Sütterlin, P., Hillberg, T., and Rouppe van der Voort, L. (2015). CRISPRED: A data pipeline for the CRISP imaging spectropolarimeter. *Astronomy & Astrophysics*, 573:A40.
- De Moortel, I. (2005). An overview of coronal seismology. *Royal Society of London Philosophical Transactions Series A*, 363:2743–2760.
- De Moortel, I., Hood, A. W., and Ireland, J. (2002). Coronal seismology through wavelet analysis. *Astronomy & Astrophysics*, 381:311–323.
- De Moortel, I., Ireland, J., and Walsh, R. W. (2000). Observation of oscillations in coronal loops. *Astronomy & Astrophysics*, 355:L23–L26.
- De Moortel, I. and Nakariakov, V. M. (2012). Magnetohydrodynamic waves and coronal seismology: an overview of recent results. *Royal Society of London Philosophical Transactions Series A*, 370:3193–3216.
- De Pontieu, B., Erdélyi, R., and James, S. P. (2004). Solar chromospheric spicules from the leakage of photospheric oscillations and flows. *Nature*, 430:536–539.
- De Pontieu, B., McIntosh, S. W., Carlsson, M., Hansteen, V. H., Tarbell, T. D., Boerner, P., Martinez-Sykora, J., Schrijver, C. J., and Title, A. M. (2011). The Origins of Hot Plasma in the Solar Corona. *Science*, 331:55–.
- De Pontieu, B., McIntosh, S. W., Carlsson, M., Hansteen, V. H., Tarbell, T. D., Schrijver, C. J., Title, A. M., Shine, R. A., Tsuneta, S., Katsukawa, Y., Ichimoto,

- K., Suematsu, Y., Shimizu, T., and Nagata, S. (2007). Chromospheric Alfvénic Waves Strong Enough to Power the Solar Wind. *Science*, 318:1574–.
- DeForest, C. E., Hagenaar, H. J., Lamb, D. A., Parnell, C. E., and Welsch, B. T. (2007). Solar Magnetic Tracking. I. Software Comparison and Recommended Practices. *The Astrophysical Journal*, 666:576–587.
- Díaz, A. J. and Roberts, B. (2006). Slow MHD oscillations in density structured coronal loops. *Astronomy & Astrophysics*, 458:975–985.
- Domingo, V., Fleck, B., and Poland, A. (1995). Soho: the solar and heliospheric observatory. *Space Science Reviews*, 72(1-2):81–84.
- Dorotovič, I., Erdélyi, R., Freij, N., Karlovský, V., and Márquez, I. (2014). Standing sausage waves in photospheric magnetic waveguides. *Astronomy & Astrophysics*, 563.
- Dorotovič, I., Erdélyi, R., and Karlovský, V. (2008). Identification of linear slow sausage waves in magnetic pores. In Erdélyi, R. and Mendoza-Briceño, C. A., editors, *Proc. IAU Symposium No. 247*, volume 247, page 351. Cambridge University Press.
- Dorotovič, I., Sobotka, M., Brandt, P. N., and Simon, G. W. (2002). Evolution and motions of small-scale photospheric structures near a large solar pore. *Astronomy & Astrophysics*, 387:665.
- Edwin, P. M. and Roberts, B. (1982). Wave propagation in a magnetically structured atmosphere. III - The slab in a magnetic environment. *Solar Physics*, 76:239–259.
- Edwin, P. M. and Roberts, B. (1983). Wave propagation in a magnetic cylinder. *Solar Physics*, 88:179–191.
- Erdélyi, R. (2004). Coronal heating: Heating in the solar atmosphere. *Astronomy and Geophysics*, 45(4):34–4.
- Erdélyi, R. and Ballai, I. (2007). Heating of the solar and stellar coronae: a review. *Astronomische Nachrichten*, 328:726–733.
- Erdélyi, R., Doyle, J. G., Perez, M. E., and Wilhelm, K. (1998). Center-to-limb line width measurements of solar chromospheric, transition region and coronal lines. *Astronomy & Astrophysics*, 337:287–293.

- Erdélyi, R. and Fedun, V. (2007). Are There Alfvén Waves in the Solar Atmosphere? *Science*, 318:1572–.
- Erdélyi, R. and Fedun, V. (2010). Magneto-Acoustic Waves in Compressible Magnetically Twisted Flux Tubes. *Solar Physics*, 263:63–85.
- Erdélyi, R., Hague, A., and Nelson, C. J. (2013). Effects of Stratification and Flows on P₁/P₂ Ratios and Anti-node Shifts Within Closed Loop Structures. *Solar Physics*.
- Erdélyi, R., Malins, C., Tóth, G., and De Pontieu, B. (2007). Leakage of photospheric acoustic waves into non-magnetic solar atmosphere. *Astronomy & Astrophysics*, 467(3):1299–1311.
- Erdélyi, R. and Morton, R. J. (2009). Magnetohydrodynamic waves in a compressible magnetic flux tube with elliptical cross-section. *The Astrophysical Journal*, 494:295–309.
- Evans, D. and Roberts, B. (1990). The oscillations of a magnetic flux tube and its application to sunspots. *The Astrophysical Journal*, 348:346–356.
- Fedun, V., Shelyag, S., and Erdélyi, R. (2011a). Numerical modeling of footpoint-driven magneto-acoustic wave propagation in a localized solar flux tube. *The Astrophysical Journal*, 727:17.
- Fedun, V., Shelyag, S., Verth, G., Mathioudakis, M., and Erdélyi, R. (2011b). Mhd waves generated by high-frequency photospheric vortex motions. *Ann. Geophys.*, 29:1029–1035.
- Fleck, B. and Deubner, F. (1989). Dynamics of the solar atmosphere. ii-standing waves in the solar chromosphere. *Astronomy & Astrophysics*, 224:245–252.
- Freeland, S. L. and Handy, B. N. (1998). Data Analysis with the SolarSoft System. *Solar Physics*, 182:497–500.
- Freij, N., Scullion, E. M., Nelson, C. J., Mumford, S., Wedemeyer, S., and Erdélyi, R. (2014). The Detection of Upwardly Propagating Waves Channeling Energy from the Chromosphere to the Low Corona. *The Astrophysical Journal*, 791:61.
- Friis-Christensen, E. and Lassen, K. (1991). Length of the solar cycle: An indicator of solar activity closely associated with climate. *Science*, 254(5032):698–700.

- Fujimura, D. and Tsuneta, S. (2009). Properties of Magnetohydrodynamic Waves in the Solar Photosphere Obtained with Hinode. *The Astrophysical Journal*, 702:1443–1457.
- Gai, M. (2000). From the sun to the great attractor. *Lecture Notes in Physics, Springer*, page 49.
- Gary, G. (2001). Plasma beta above a solar active region: rethinking the paradigm. *Solar Physics*, 203(1):71–86.
- Gent, F. A., Fedun, V., and Erdélyi, R. (2014). Magnetohydrostatic Equilibrium. II. Three-dimensional Multiple Open Magnetic Flux Tubes in the Stratified Solar Atmosphere. *The Astrophysical Journal*, 789:42.
- Gent, F. A., Fedun, V., Mumford, S. J., and Erdélyi, R. (2013). Magnetohydrostatic equilibrium - I. Three-dimensional open magnetic flux tube in the stratified solar atmosphere. *Monthly Notices of the Royal Astronomical Society*, 435:689–697.
- Georgakilas, A. A., Christopoulou, E. B., and Koutchmy, S. (2002). Oscillations and waves related to sunspots. *Nuovo Cimento C Geophysics Space Physics C*, 25:601.
- Giovanelli, R. G. (1972). Oscillations and Waves in a Sunspot. *Solar Physics*, 27:71–79.
- Goedbloed, J. and Poedts, S. (2004). *Principles of Magnetohydrodynamics: With Applications to Laboratory and Astrophysical Plasmas*. Cambridge University Press.
- Goossens, M., Andries, J., and Aschwanden, M. J. (2002). Coronal loop oscillations. An interpretation in terms of resonant absorption of quasi-mode kink oscillations. *Astronomy & Astrophysics*, 394:L39–L42.
- Gosain, S., Mathew, S. K., and Venkatakrishnan, P. (2011). Acoustic Power Absorption and its Relation to Vector Magnetic Field of a Sunspot. *Solar Physics*, 268:335–348.
- Grant, S. D. T., Jess, D. B., Moreels, M. G., Morton, R. J., Christian, D. J., Giagkiozis, I., Verth, G., Fedun, V., Keys, P. H., Doorsselaere, T. V., and Erdélyi, R. (2015). Wave damping observed in upwardly propagating sausage-mode oscillations contained within a magnetic pore. *The Astrophysical Journal*, 806(1):132.

- Handy, B., Acton, L., Kankelborg, C., Wolfson, C., Akin, D., Bruner, M., Caravalho, R., Catura, R., Chevalier, R., Duncan, D., Edwards, C., Feinstein, C., Freeland, S., Friedlaender, F., Hoffmann, C., Hurlburt, N., Jurcevich, B., Katz, N., Kelly, G., Lemen, J., Levay, M., Lindgren, R., Mathur, D., Meyer, S., Morrison, S., Morrison, M., Nightingale, R., Pope, T., Rehse, R., Schrijver, C., Shine, R., Shing, L., Strong, K., Tarbell, T., Title, A., Torgerson, D., Golub, L., Bookbinder, J., Caldwell, D., Cheimets, P., Davis, W., Deluca, E., McMullen, R., Warren, H., Amato, D., Fisher, R., Maldonado, H., and Parkinson, C. (1999). The transition region and coronal explorer. *Solar Physics*, 187(2):229–260.
- Hasan, S. and Van Ballegooijen, A. (2008). Dynamics of the solar magnetic network. ii. heating the magnetized chromosphere. *The Astrophysical Journal*, 680:1542.
- Hasan, S. S., van Ballegooijen, A. A., Kalkofen, W., and Steiner, O. (2005). Dynamics of the Solar Magnetic Network: Two-dimensional MHD Simulations. *The Astrophysical Journal*, 631:1270–1280.
- Henriques, V. M. J. (2012). Three-dimensional temperature mapping of solar photospheric fine structure using Ca ii H filtergrams. *Astronomy & Astrophysics*, 548:A114.
- Hirzberger, J., Bonet, J. A., Sobotka, M., Vázquez, M., and Hanslmeier, A. (2002). Fine structure and dynamics in a light bridge inside a solar pore. *Astronomy & Astrophysics*, 383:275–282.
- Huang, N., Shen, Z., Long, S., Wu, M., Shih, H., Zheng, Q., Yen, N., Tung, C., and Liu, H. (1998). The empirical mode decomposition and the hilbert spectrum for nonlinear and non-stationary time series analysis. *Proc. R. Soc. A*, 454(1971):903.
- Huang, N. E. and Wu, Z. (2008). A review on hilbert-huang transform: Method and its applications to geophysical studies. *Reviews of Geophysics*, 46(2).
- Hunter, J. D. (2007). Matplotlib: A 2D graphics environment. *Computing in Science & Engineering*, 9(3):90–95.
- Jess, D., Mathioudakis, M., Christian, D., Keenan, F., Ryans, R., and Crockett, P. (2010). Rosa: A high-cadence, synchronized multi-camera solar imaging system. *Solar Physics*, 261(2):363–373.
- Jess, D. B., Andić, A., Mathioudakis, M., Bloomfield, D. S., and Keenan, F. P. (2007). High-frequency oscillations in a solar active region observed with the RAPID DUAL IMAGER. *Astronomy & Astrophysics*, 473:943–950.

- Jess, D. B., Mathioudakis, M., Erdélyi, R., Crockett, P. J., Keenan, F. P., and Christian, D. J. (2009). Alfvén Waves in the Lower Solar Atmosphere. *Science*, 323:1582–.
- Jess, D. B., Morton, R. J., Verth, G., Fedun, V., Grant, S. D. T., and Giagkiozis, I. (2015). Multiwavelength Studies of MHD Waves in the Solar Chromosphere. An Overview of Recent Results. *Space Science Reviews*, 190:103–161.
- Jess, D. B., Reznikova, V. E., Van Doorsselaere, T., Keys, P. H., and Mackay, D. H. (2013). The Influence of the Magnetic Field on Running Penumbral Waves in the Solar Chromosphere. *The Astrophysical Journal*, 779:168.
- Jones, E., Oliphant, T., and Peterson, P. (2001). SciPy: Open source scientific tools for python.
- Kato, Y., Steiner, O., Steffen, M., and Suematsu, Y. (2011). Excitation of Slow Modes in Network Magnetic Elements Through Magnetic Pumping. *The Astrophysical Journal, Letters*, 730:L24.
- Katsiyannis, A. C., Williams, D. R., McAteer, R. T. J., Gallagher, P. T., Keenan, F. P., and Murtagh, F. (2003). Eclipse observations of high-frequency oscillations in active region coronal loops. *Astronomy & Astrophysics*, 406:709–714.
- Keller, C. U. and von der Luehe, O. (1992). Solar speckle polarimetry. *Astronomy & Astrophysics*, 261:321–328.
- Kelvinsong (2015). http://en.wikipedia.org/wiki/User:Kelvinsong/File:Sun_poster.svg. Accessed: 2015-01-01. License: Creative Commons Attribution-ShareAlike 3.0 Unported.
- Khomenko, E. and Cally, P. S. (2012). Numerical simulations of conversion to alfvén waves in sunspots. *The Astrophysical Journal*, 746(1):68.
- Khomenko, E., Collados, M., and Felipe, T. (2008). Nonlinear numerical simulations of magneto-acoustic wave propagation in small-scale flux tubes. *Solar Physics*, 251(1):589–611.
- Kiselman, D., Pereira, T. M. D., Gustafsson, B., Asplund, M., Meléndez, J., and Langhans, K. (2011). Is the solar spectrum latitude-dependent?. An investigation with SST/TRIPPEL. *Astronomy & Astrophysics*, 535:A14.
- Kitagawa, N., Yokoyama, T., Imada, S., and Hara, H. (2010). Mode Identification of MHD Waves in an Active Region Observed with Hinode/EIS. *The Astrophysical Journal*, 721:744–749.

- Kobanov, N. and Makarchik, D. (2004). Pulsating evershed flows and propagating waves in a sunspot. *Astron. Rep.*, 48(11):954–964.
- Kobanov, N. I., Kolobov, D. Y., and Makarchik, D. V. (2006). Umbral Three-Minute Oscillations and Running Penumbral Waves. *Solar Physics*, 238:231–244.
- Kontar, E. P., Hannah, I. G., and MacKinnon, A. L. (2008). Chromospheric magnetic field and density structure measurements using hard X-rays in a flaring coronal loop. *Astronomy & Astrophysics*, 489:L57–L60.
- Kosovichev, A. G. (2009). Solar Oscillations. In Guzik, J. A. and Bradley, P. A., editors, *American Institute of Physics Conference Series*, volume 1170 of *American Institute of Physics Conference Series*, pages 547–559.
- Leenaarts, J., Carlsson, M., Hansteen, V., and Rutten, R. J. (2007). Non-equilibrium hydrogen ionization in 2D simulations of the solar atmosphere. *Astronomy & Astrophysics*, 473:625–632.
- Leenaarts, J., Carlsson, M., and Rouppe van der Voort, L. (2012). The Formation of the H α Line in the Solar Chromosphere. *The Astrophysical Journal*, 749:136.
- Leibacher, J., Gouttebroze, P., and Stein, R. (1982). Solar atmospheric dynamics. ii-nonlinear models of the photospheric and chromospheric oscillations. *The Astrophysical Journal*, 258:393–403.
- Lemen, J. R., Title, A. M., Akin, D. J., Boerner, P. F., Chou, C., Drake, J. F., Duncan, D. W., Edwards, C. G., Friedlaender, F. M., Heyman, G. F., Hurlburt, N. E., Katz, N. L., Kushner, G. D., Levay, M., Lindgren, R. W., Mathur, D. P., McFeaters, E. L., Mitchell, S., Rehse, R. A., Schrijver, C. J., Springer, L. A., Stern, R. A., Tarbell, T. D., Wuelser, J.-P., Wolfson, C. J., Yanari, C., Bookbinder, J. A., Cheimets, P. N., Caldwell, D., Deluca, E. E., Gates, R., Golub, L., Park, S., Podgorski, W. A., Bush, R. I., Scherrer, P. H., Gummin, M. A., Smith, P., Auker, G., Jerram, P., Pool, P., Soufli, R., Windt, D. L., Beardsley, S., Clapp, M., Lang, J., and Waltham, N. (2012). The Atmospheric Imaging Assembly (AIA) on the Solar Dynamics Observatory (SDO). *Solar Physics*, 275:17–40.
- Lin, H., Kuhn, J. R., and Coulter, R. (2004). Coronal magnetic field measurements. *The Astrophysical Journal Letters*, 613(2):L177.
- Liu, Y., San Liang, X., and Weisberg, R. H. (2007). Rectification of the bias in the wavelet power spectrum. *Journal of Atmospheric and Oceanic Technology*, 24(12):2093–2102.

- Longcope, D. W. (1996). Topology and Current Ribbons: A Model for Current, Reconnection and Flaring in a Complex, Evolving Corona. *Solar Physics*, 169:91–121.
- Longcope, D. W. and Klapper, I. (2002). A General Theory of Connectivity and Current Sheets in Coronal Magnetic Fields Anchored to Discrete Sources. *The Astrophysical Journal*, 579:468–481.
- Luna-Cardozo, C., Verth, G., and Erdélyi, R. (2012). Longitudinal oscillations in density stratified and expanding solar waveguides. *The Astrophysical Journal*, 748(2):110.
- Malins, C. and Erdélyi, R. (2007). Direct propagation of photospheric acoustic modes into nonmagnetic solar atmosphere. *Solar Physics*, 246:41–52.
- Maltby, P., Avrett, E. H., Carlsson, M., Kjeldseth-Moe, O., Kurucz, R. L., and Loeser, R. (1986). A new sunspot umbral model and its variation with the solar cycle. *The Astrophysical Journal*, 306:284–303.
- Marsh, M. S. and Walsh, R. W. (2006). p-Mode Propagation through the Transition Region into the Solar Corona. I. Observations. *The Astrophysical Journal*, 643:540–548.
- Marsh, M. S., Walsh, R. W., and Bromage, B. J. I. (2002). A wavelet analysis of quasi-periodic variability across a solar coronal hole region. *Astronomy & Astrophysics*, 393:649–659.
- Mathew, S. K. (2008). Enhanced p-Mode Absorption Seen Near the Sunspot Umbral Penumbra Boundary. *Solar Physics*, 251:515–522.
- Mathioudakis, M., Bloomfield, D., Jess, D., Dhillon, V., and Marsh, T. (2006). The periodic variations of a white-light flare observed with ultracam. *Astronomy & Astrophysics*, 456(1):323–327.
- Mathioudakis, M., Jess, D. B., and Erdélyi, R. (2013). Alfvén Waves in the Solar Atmosphere. From Theory to Observations. *Space Science Reviews*, 175:1–27.
- McIntosh, S. W. (2012). Recent Observations of Plasma and Alfvénic Wave Energy Injection at the Base of the Fast Solar Wind. *Space Science Reviews*, 172:69–87.
- McIntosh, S. W., de Pontieu, B., Carlsson, M., Hansteen, V., Boerner, P., and Goossens, M. (2011). Alfvénic waves with sufficient energy to power the quiet solar corona and fast solar wind. *Nature*, 475:477–480.

- McLaughlin, J. A., Hood, A. W., and de Moortel, I. (2011). Review Article: MHD Wave Propagation Near Coronal Null Points of Magnetic Fields. *Space Science Reviews*, 158:205–236.
- Mein, N. and Mein, P. (1976). Velocity waves in the quiet solar chromosphere. *Solar Physics*, 49(2):231–248.
- Metcalf, T. R., Jiao, L., McClymont, A. N., Canfield, R. C., and Uitenbroek, H. (1995). Is the solar chromospheric magnetic field force-free? *The Astrophysical Journal*, 439:474–481.
- Moreels, M. G., Freij, N., Erdélyi, R., Van Doorsselaere, T., and Verth, G. (2015). Observations and mode identification of sausage waves in a magnetic pore. *Astronomy & Astrophysics*, 579:A73.
- Moreels, M. G., Goossens, M., and Van Doorsselaere, T. (2013). Cross-sectional area and intensity variations of sausage modes. *Astronomy & Astrophysics*, 555:A75.
- Moreels, M. G. and Van Doorsselaere, T. (2013). Phase relations for seismology of photospheric flux tubes. *Astronomy & Astrophysics*, 551:A137.
- Moreton, G. E. (1960). H α Observations of Flare-Initiated Disturbances with Velocities \sim 1000 km/sec. *Astronomical Journal*, 65:494.
- Morton, R. J. and Erdélyi, R. (2009). The effect of elliptic shape on the period ratio P₁/P₂ of emerging coronal loops. *Astronomy & Astrophysics*, 502:315–323.
- Morton, R. J., Erdélyi, R., Jess, D. B., and Mathioudakis, M. (2011). Observations of Sausage Modes in Magnetic Pores. *The Astrophysical Journal, Letters*, 729:L18.
- Morton, R. J. and Ruderman, M. S. (2011). Kink and fluting modes of stratified coronal magnetic loops with elliptical cross-sections. *Astronomy & Astrophysics*, 527:A53.
- Morton, R. J., Verth, G., Jess, D. B., Kuridze, D., Ruderman, M. S., Mathioudakis, M., and Erdélyi, R. (2012). Observations of ubiquitous compressive waves in the Sun’s chromosphere. *Nature Communications*, 3.
- Mumford, S. J., Fedun, V., and Erdélyi, R. (2015). Generation of magnetohydrodynamic waves in low solar atmospheric flux tubes by photospheric motions. *The Astrophysical Journal*, 799(1):6.

- Nakariakov, V. M., Ofman, L., Deluca, E. E., Roberts, B., and Davila, J. M. (1999). TRACE observation of damped coronal loop oscillations: Implications for coronal heating. *Science*, 285:862–864.
- Nakariakov, V. M. and Verwichte, E. (2005). Coronal waves and oscillations. *Living Reviews in Solar Physics*, 2(3).
- Nelson, C. J. and Doyle, J. G. (2013). Excitation of an outflow from the lower solar atmosphere and a co-temporal EUV transient brightening. *Astronomy & Astrophysics*, 560:A31.
- Nelson, C. J., Doyle, J. G., Erdélyi, R., Huang, Z., Madjarska, M. S., Mathioudakis, M., Mumford, S. J., and Reardon, K. (2013a). Statistical Analysis of Small Ellerman Bomb Events. *Solar Physics*, 283:307–323.
- Nelson, C. J., Scullion, E. M., Doyle, J. G., Freij, N., and Erdélyi, R. (2015). Small-scale Structuring of Ellerman Bombs at the Solar Limb. *The Astrophysical Journal*, 798:19.
- Nelson, C. J., Shelyag, S., Mathioudakis, M., Doyle, J. G., Madjarska, M. S., Uitenbroek, H., and Erdélyi, R. (2013b). Ellerman Bombs—Evidence for Magnetic Reconnection in the Lower Solar Atmosphere. *The Astrophysical Journal*, 779:125.
- Nye, A. H. and Thomas, J. H. (1974). The nature of running penumbral waves. *Solar Physics*, 38:399–413.
- Ofman, L. and Aschwanden, M. J. (2002). Damping time scaling of coronal loop oscillations deduced from transition region and coronal explorer observations. *Astrophys. J. Lett.*, 576:L153–L156.
- Ofman, L., Romoli, M., Poletto, G., Noci, G., and Kohl, J. L. (1997). Ultraviolet Coronagraph Spectrometer Observations of Density Fluctuations in the Solar Wind. *The Astrophysical Journal, Letters*, 491:L111–L114.
- Olcott, W. (1914). *Sun Lore of All Ages: A Collection of Myths and Legends Concerning the Sun and Its Worship*. G.P. Putnam's sons.
- O'Shea, E., Srivastava, A., Doyle, J., and Banerjee, D. (2007). Evidence for wave harmonics in cool loops. *Astronomy & Astrophysics*, 473(2):13–16.
- Parnell, C. E. and De Moortel, I. (2012). A contemporary view of coronal heating. *Royal Society of London Philosophical Transactions Series A*, 370:3217–3240.

- Perez, F. and Granger, B. E. (2007). IPython: A system for interactive scientific computing. *Computing in Science & Engineering*, 9(3):21–29.
- Peter, H., Gudiksen, B. V., and Nordlund, Å. (2006). Forward Modeling of the Corona of the Sun and Solar-like Stars: From a Three-dimensional Magnetohydrodynamic Model to Synthetic Extreme-Ultraviolet Spectra. *The Astrophysical Journal*, 638:1086–1100.
- Priest, E. (2014). *Magnetohydrodynamics of the Sun*.
- Priest, E. R. (1984). *Solar magneto-hydrodynamics*. Springer.
- Project, G. (2015). http://galileo.rice.edu/images/things/sunspot_drawings/ss623-1.gif. Accessed: 2015-01-01. No copyright.
- Reznikova, V. E. and Shibasaki, K. (2012). Spatial Structure of Sunspot Oscillations Observed with SDO/AIA. *The Astrophysical Journal*, 756:35.
- Rieutord, M. and Rincon, F. (2010). The sun’s supergranulation. *Living Reviews in Solar Physics*, 7(2).
- Roberts, B. (2006). Slow magnetohydrodynamic waves in the solar atmosphere. *Phil. Trans. R. Soc. London. Ser. A*, 364:447.
- Roudier, T., Bonet, J. A., and Sobotka, M. (2002). Properties of horizontal flows inside and outside a solar pore. *Astronomy & Astrophysics*, 395:249–255.
- Ruderman, M. S. (2003). The resonant damping of oscillations of coronal loops with elliptic cross-sections. *Astronomy & Astrophysics*, 409:287–297.
- Ruderman, M. S. and Erdélyi, R. (2009). Transverse Oscillations of Coronal Loops. *Space Science Reviews*, 149:199–228.
- Rutten, R., Hammerschlag, R., Bettonvil, F., Sütterlin, P., and De Wijn, A. (2004). Dot tomography of the solar atmosphere. *Astronomy & Astrophysics*, 413(3):1183–1189.
- Rutten, R. J. (2012). The quiet-Sun photosphere and chromosphere. *Royal Society of London Philosophical Transactions Series A*, 370:3129–3150.
- Scharmer, G., Brown, D., Pettersson, L., and Rehn, J. (1985). Concepts for the swedish 50-cm vacuum solar telescope. *Applied Optics*, 24(16):2558–2564.

- Scharmer, G. and Lofdahl, M. (1991). Swedish Solar Telescope - Short summary of instrumentation and observation techniques. *Advances in Space Research*, 11:129–132.
- Scharmer, G. B., Narayan, G., Hillberg, T., de la Cruz Rodríguez, J., Löfdahl, M. G., Kiselman, D., Sütterlin, P., van Noort, M., and Lagg, A. (2008). CRISP Spectropolarimetric Imaging of Penumbral Fine Structure. *The Astrophysical Journal, Letters*, 689:L69–L72.
- Schou, J., Scherrer, P. H., Bush, R. I., Wachter, R., Couvidat, S., Rabello-Soares, M. C., Bogart, R. S., Hoeksema, J. T., Liu, Y., Duvall, T. L., Akin, D. J., Allard, B. A., Miles, J. W., Rairden, R., Shine, R. A., Tarbell, T. D., Title, A. M., Wolfson, C. J., Elmore, D. F., Norton, A. A., and Tomczyk, S. (2012). Design and Ground Calibration of the Helioseismic and Magnetic Imager (HMI) Instrument on the Solar Dynamics Observatory (SDO). *Solar Physics*, 275:229–259.
- Schrijver, C. J., Title, A. M., Berger, T. E., Fletcher, L., Hurlburt, N. E., Nightingale, R. W., Shine, R. A., Tarbell, T. D., Wolfson, J., Golub, L., Bookbinder, J. A., Deluca, E. E., McMullen, R. A., Warren, H. P., Kankelborg, C. C., Handy, B. N., and de Pontieu, B. (1999). A new view of the solar outer atmosphere by the Transition Region and Coronal Explorer. *Solar Physics*, 187:261–302.
- Scullion, E., Erdélyi, R., Fedun, V., and Doyle, J. G. (2011). The response of a three-dimensional solar atmosphere to wave-driven jets. *The Astrophysical Journal*, 743(1):14.
- Sekse, D. H., Rouppe van der Voort, L., De Pontieu, B., and Scullion, E. (2013). Interplay of Three Kinds of Motion in the Disk Counterpart of Type II Spicules: Upflow, Transversal, and Torsional Motions. *The Astrophysical Journal*, 769:44.
- Shelyag, S., Fedun, V., Keenan, F. P., Erdélyi, R., and Mathioudakis, M. (2011). Photospheric magnetic vortex structures. *Annales Geophysicae*, 29:883–887.
- Simon, G. W. and Weiss, N. O. (1970). On the Magnetic Field in Pores. *Solar Physics*, 13:85–103.
- Sobotka, M., Brandt, P. N., and Simon, G. W. (1997). Fine structure in sunspots 1.sizes and lifetimes of umbral dots. *Astronomy & Astrophysics*, 328:682.
- Solanki, S. K. (2003). Sunspots: An overview. *Astronomy & Astrophysics Reviews*, 11:153–286.

- Soward, A. M., Jones, C. A., Hughes, D. W., and Weiss, N. O. (2005). *Fluid dynamics and dynamos in astrophysics and geophysics*. CRC press.
- Stangalini, M., Giannattasio, F., Del Moro, D., and Berrilli, F. (2012). Three-minute wave enhancement in the solar photosphere. *Astronomy & Astrophysics*, 539:L4.
- Staude, J. (1999). Sunspot Oscillations. In Schmieder, B., Hofmann, A., and Staude, J., editors, *Third Advances in Solar Physics Euroconference: Magnetic Fields and Oscillations*, volume 184 of *Astronomical Society of the Pacific Conference Series*, pages 113–130.
- Steiner, O., Grossmann-Doerth, U., Knoelker, M., and Schuessler, M. (1998). Dynamical Interaction of Solar Magnetic Elements and Granular Convection: Results of a Numerical Simulation. *The Astrophysical Journal*, 495:468.
- Strong, K., Bruner, M., Tarbell, T., Title, A., and Wolfson, C. (1994). Trace — the transition region and coronal explorer. *Space Science Reviews*, 70(1-2):119–122.
- Suzuki, T. K. (2011). Self-consistent Simulations of Alfvén Wave Driven Winds from the Sun and Stars. *Space Science Reviews*, 158:339–363.
- Sych, R. A. and Nakariakov, V. M. (2008). The Pixelised Wavelet Filtering Method to Study Waves and Oscillations in Time Sequences of Solar Atmospheric Images. *Solar Physics*, 248:395–408.
- Sympy Development Team (2014). *Sympy: Python library for symbolic mathematics*.
- Taroyan, Y. and Erdélyi, R. (2009). Heating Diagnostics with MHD Waves. *Space Science Reviews*, 149:229–254.
- Taroyan, Y., Erdélyi, R., Doyle, J., and Bradshaw, S. (2005). Footpoint excitation of standing acoustic waves in coronal loops. *Astronomy & Astrophysics*, 438(2):713–720.
- Terradas, J., Oliver, R., and Ballester, J. (2004). Application of statistical techniques to the analysis of solar coronal oscillations. *The Astrophysical Journal*, 614:435.
- The Astropy Collaboration, Robitaille, T. P., Tollerud, E. J., Greenfield, P., Droettboom, M., Bray, E., Aldcroft, T., Davis, M., Ginsburg, A., Price-Whelan, A. M., Kerzendorf, W. E., Conley, A., Crighton, N., Barbary, K., Muna, D., Ferguson, H., Grollier, F., Parikh, M. M., Nair, P. H., Günther, H. M., Deil, C., Woillez,

- J., Conseil, S., Kramer, R., Turner, J. E. H., Singer, L., Fox, R., Weaver, B. A., Zabalza, V., Edwards, Z. I., Azalee Bostroem, K., Burke, D. J., Casey, A. R., Crawford, S. M., Dencheva, N., Ely, J., Jenness, T., Labrie, K., Lim, P. L., Pierfederici, F., Pontzen, A., Ptak, A., Refsdal, B., Servillat, M., and Streicher, O. (2013). Astropy: A community python package for astronomy. *Astronomy & Astrophysics*, 558:A33.
- The SunPy Community, Mumford, S. J., Christe, S., Pérez-Suárez, D., Ireland, J., Shih, A. Y., Inglis, A. R., Liedtke, S., Hewett, R. J., Mayer, F., Hughitt, K., Freij, N., Meszaros, T., Bennett, S. M., Malocha, M., Evans, J., Agrawal, A., Leonard, A. J., Robitaille, T. P., Mampaey, B., Campos-Rozo, J. I., and Kirk, M. S. (2015). SunPy—python for solar physics. *Computational Science & Discovery*, 8(1):014009.
- Thompson, B. J., Plunkett, S. P., Gurman, J. B., Newmark, J. S., St. Cyr, O. C., and Michels, D. J. (1998). SOHO/EIT observations of an Earth-directed coronal mass ejection on May 12, 1997. *Geophysics Research Letters*, 25:2465–2468.
- Tian, H., Curdt, W., Teriaca, L., Landi, E., and Marsch, E. (2009). Solar transition region above sunspots. *Astronomy & Astrophysics*, 505(1):307–318.
- Torrence, C. and Compo, G. (1998). A practical guide to wavelet analysis. *Bulletin of the American Meteorological Society*, 79(1):61–78.
- Uitenbroek, H. and Tritschler, A. (2006). The contrast of magnetic elements in synthetic ch- and cn-band images of solar magnetoconvection. *The Astrophysical Journal*, 639(1):525.
- van der Walt, S., Schönberger, J. L., Nunez-Iglesias, J., Boulogne, F., Warner, J. D., Yager, N., Gouillart, E., and Yu, T. (2014). scikit-image: image processing in python. *PeerJ*, 2:e453.
- van Noort, M., Rouppe van der Voort, L., and Löfdahl, M. G. (2005). Solar Image Restoration By Use Of Multi-frame Blind De-convolution With Multiple Objects And Phase Diversity. *Solar Physics*, 228:191–215.
- Vecchio, A., Cauzzi, G., Reardon, K. P., Janssen, K., and Rimmele, T. (2007). Solar atmospheric oscillations and the chromospheric magnetic topology. *Astronomy & Astrophysics*, 461:L1–L4.

- Veleda, D., Montagne, R., and Araujo, M. (2012). Cross-wavelet bias corrected by normalizing scales. *Journal of Atmospheric and Oceanic Technology*, 29(9):1401–1408.
- Vernazza, J. E., Avrett, E. H., and Loeser, R. (1981). Structure of the solar chromosphere. III - Models of the EUV brightness components of the quiet-sun. *The Astrophysical Journal, Supplement*, 45:635–725.
- Verth, G. and Erdélyi, R. (2008). Effect of longitudinal magnetic and density inhomogeneity on transversal coronal loop oscillations. *Astronomy & Astrophysics*, 486:1015–1022.
- Verth, G., Erdélyi, R., and Jess, D. B. (2008). Refined Magnetoseismological Technique for the Solar Corona. *The Astrophysical Journal, Letters*, 687:L45–L48.
- Verwichte, E., Nakariakov, V. M., and Cooper, F. C. (2005). Transverse waves in a post-flare supra-arcade. *Astronomy & Astrophysics*, 430:L65–L68.
- Vigeesh, G., Fedun, V., Hasan, S. S., and Erdélyi, R. (2012). Three-dimensional Simulations of Magnetohydrodynamic Waves in Magnetized Solar Atmosphere. *The Astrophysical Journal*, 755:18.
- Vögler, A., Shelyag, S., Schüssler, M., Cattaneo, F., Emonet, T., and Linde, T. (2005). Simulations of magneto-convection in the solar photosphere. *Astronomy & Astrophysics*, 429(1):335–351.
- Wang, T. (2011). Standing slow-mode waves in hot coronal loops: Observations, modeling, and coronal seismology. *Space Science Reviews*, 158(2):397–419.
- Wang, T. J. (2004). Coronal Loop Oscillations: Overview of Recent Results In Observations. In Lacoste, H., editor, *SOHO 13 Waves, Oscillations and Small-Scale Transients Events in the Solar Atmosphere: Joint View from SOHO and TRACE*, volume 547 of *ESA Special Publication*, page 417.
- Wang, T. J., Solanki, S. K., Curdt, W., Innes, D. E., Dammasch, I. E., and Kliem, B. (2003). Hot coronal loop oscillations observed with SUMER: Examples and statistics. *Astronomy & Astrophysics*, 406:1105–1121.
- Wedemeyer-Böhm, S., Scullion, E., Steiner, O., Rouppe van der Voort, L., de La Cruz Rodriguez, J., Fedun, V., and Erdélyi, R. (2012). Magnetic tornadoes as energy channels into the solar corona. *Nature*, 486:505–508.

- Williams, D. R., Mathioudakis, M., Gallagher, P. T., Phillips, K. J. H., McAteer, R. T. J., Keenan, F. P., Rudawy, P., and Katsiyannis, A. C. (2002). An observational study of a magneto-acoustic wave in the solar corona. *Monthly Notices of the Royal Astronomical Society*, 336:747–752.
- Williams, D. R., Phillips, K. J. H., Rudawy, P., Mathioudakis, M., Gallagher, P. T., O’Shea, E., Keenan, F. P., Read, P., and Rompolt, B. (2001). High-frequency oscillations in a solar active region coronal loop. *Monthly Notices of the Royal Astronomical Society*, 326:428–436.
- Wöger, F., von der Lühe, O., and Reardon, K. (2008). Speckle interferometry with adaptive optics corrected solar data. *Astron. Astrophys.*, 488:375–381.
- Woods, T. N., Eparvier, F. G., Hock, R., Jones, A. R., Woodraska, D., Judge, D., Didkovsky, L., Lean, J., Mariska, J., Warren, H., McMullin, D., Chamberlin, P., Berthiaume, G., Bailey, S., Fuller-Rowell, T., Sojka, J., Tobiska, W. K., and Viereck, R. (2012). Extreme Ultraviolet Variability Experiment (EVE) on the Solar Dynamics Observatory (SDO): Overview of Science Objectives, Instrument Design, Data Products, and Model Developments. *Solar Physics*, 275:115–143.
- Wu, Z. and Huang, N. E. (2009). Ensemble empirical mode decomposition: a noise-assisted data analysis method. *Advances in adaptive data analysis*, 1(01):1–41.
- Zaqarashvili, T. V. and Erdélyi, R. (2009). Oscillations and Waves in Solar Spicules. *Space Science Reviews*, 149:355–388.
- Zeng, K. and He, M.-X. (2004). A simple boundary process technique for empirical mode decomposition. In *Geoscience and Remote Sensing Symposium, 2004. IGARSS’04. Proceedings. 2004 IEEE International*, volume 6, pages 4258–4261. IEEE.
- Zhugzhda, I. and Dzhalilov, N. (1982). Transformation of magnetogravitational waves in the solar atmosphere. *Astronomy & Astrophysics*, 112:16–23.
- Zhugzhda, Y. D. (1973). Resonance in a Semi-Infinite Isothermal Atmosphere. *The Astrophysical Journal, Letters*, 15:119.
- Zirin, H. and Stein, A. (1972). Observations of Running Penumbral Waves. *The Astrophysical Journal, Letters*, 178:L85.

Appendix A

Mathematical Derivation

Chapter 4

In Chapter 4, the set of equations (Equations 4.1, 4.2, 4.3, 4.4, 4.5 and 4.6) are the ideal MHD equations which govern linear magneto-acoustic wave motions and are repeated below,

$$\rho_0 \frac{\partial v_r}{\partial t} = -\frac{\partial}{\partial r} \left(p_1 + \frac{B_0 b_z}{\mu_0} \right) + \frac{B_0}{\mu_0} \frac{\partial b_r}{\partial z}, \quad (\text{A.1})$$

$$\rho_0 \frac{\partial v_z}{\partial t} = -\frac{\partial p_1}{\partial z}, \quad (\text{A.2})$$

$$\frac{\partial b_r}{\partial t} = B_0 \frac{\partial v_r}{\partial z}, \quad (\text{A.3})$$

$$\frac{\partial b_z}{\partial t} = -B_0 \frac{1}{r} \frac{\partial (rv_r)}{\partial r}, \quad (\text{A.4})$$

$$\frac{\partial p_1}{\partial t} = -\rho_0 c_s^2 \left(\frac{1}{r} \frac{\partial (rv_r)}{\partial r} + \frac{\partial v_z}{\partial z} \right), \quad (\text{A.5})$$

$$\frac{\partial \rho_1}{\partial t} = -\rho_0 \left(\frac{1}{r} \frac{\partial (rv_r)}{\partial r} + \frac{\partial v_z}{\partial z} \right). \quad (\text{A.6})$$

Here, p is the gas pressure, ρ is the density and $\mathbf{b} = (b_r, b_\theta, b_z)$ is the perturbed magnetic field. We have assumed that the plasma motion is adiabatic. The subscripts 0 and 1 refer to unperturbed and perturbed states, respectively. The velocity perturbation is denoted as $\mathbf{v}_1 = (v_r, v_\theta, v_z)$.

So by assuming that all the perturbed quantities are a harmonic propagating wave of the form, $v_r = \hat{v}_r \cos(kz - \omega t)$, where \hat{v}_r is the amplitude of the perturbation and is a function of the radius i.e., $A(r)$.

From Equation 4.3 or A.3, we can substitute the radial velocity perturbation,

$$\omega \hat{b}_r \sin(kz - \omega t) = -B_0 k \hat{v}_r \sin(kz - \omega t) \quad (\text{A.7})$$

$$\omega \hat{b}_r = -B_0 k \hat{v}_r, \quad (\text{A.8})$$

$$\omega b_r = -B_0 k \hat{v}_r \cos(kz - \omega t), \quad (\text{A.9})$$

$$\omega b_r = -B_0 k v_r \quad (\text{A.10})$$

which is Equation 4.7.

From Equation 4.1 or A.1, we can substitute the radial velocity perturbation,

$$\rho_0 \omega \hat{v}_r \sin(kz - \omega t) = -\frac{\partial}{\partial r} \left(p_1 + \frac{B_0 b_z}{\mu_0} \right) + \frac{B_0}{\mu_0} \left(-\hat{b}_r k \sin(kz - \omega t) \right), \quad (\text{A.11})$$

$$\left(\rho_0 \omega \hat{v}_r + \frac{B_0}{\mu_0} \hat{b}_r k \right) \sin(kz - \omega t) = -\frac{\partial}{\partial r} \left(p_1 + \frac{B_0 b_z}{\mu_0} \right). \quad (\text{A.12})$$

Since $\hat{v}_r = A(r)$ and from Equation A.8, we have that $\hat{b}_r = -\frac{B_0 k}{\omega} A(r)$,

$$\left(\rho_0 \omega A(r) - \frac{B_0^2 k^2}{\mu_0 \omega} A(r) \right) \sin(kz - \omega t) = -\frac{\partial}{\partial r} \left(p_1 + \frac{B_0 b_z}{\mu_0} \right), \quad (\text{A.13})$$

$$\rho_0 \left(\frac{B_0^2 k^2}{\mu_0 \omega \rho_0} - \omega \right) A(r) \sin(kz - \omega t) = \frac{\partial}{\partial r} \left(p_1 + \frac{B_0 b_z}{\mu_0} \right), \quad (\text{A.14})$$

and since $v_A^2 = \frac{B_0^2}{\mu_0 \rho_0}$,

$$\rho_0 \left(\frac{v_A^2 k^2}{\omega} - \omega \right) A(r) \sin(kz - \omega t) = \frac{\partial}{\partial r} \left(p_1 + \frac{B_0 b_z}{\mu_0} \right), \quad (\text{A.15})$$

which is Equation 4.8.

Equation 4.2 or A.2 is the same as Equation 4.9

If we integrate Equation 4.3 or A.3, with respect time,

$$\frac{\partial b_z}{\partial t} = -B_0 \frac{1}{r} \frac{\partial(rv_r)}{\partial r}, \quad (\text{A.16})$$

$$b_z = \int -B_0 \frac{1}{r} \frac{\partial(rv_r)}{\partial r} dt, \quad (\text{A.17})$$

$$b_z = -\frac{B_0}{r} \int \frac{\partial(rA(r)\cos(kz-\omega t))}{\partial r} dt, \quad (\text{A.18})$$

$$b_z = -\frac{B_0}{r} \frac{\partial(rA(r))}{\partial r} \int \cos(kz-\omega t) dt, \quad (\text{A.19})$$

$$b_z = -\frac{B_0}{r} \frac{\partial(rA(r))}{\partial r} \left(\frac{-1}{\omega} \right) \sin(kz-\omega t) dt, \quad (\text{A.20})$$

$$b_z = \frac{B_0}{r\omega} \frac{\partial(rA(r))}{\partial r} \sin(kz-\omega t) dt, \quad (\text{A.21})$$

$$(\text{A.22})$$

which is Equation 4.10.

Next, using Equations 4.5 and 4.6 or Equations A.5 and A.6 and multiplying Equation 4.6 or A.6 by c_s^2 ,

$$\frac{\partial p_1}{\partial t} = c_s^2 \frac{\partial \rho_1}{\partial t} = -\rho_0 c_s^2 \left(\frac{1}{r} \frac{\partial(rv_r)}{\partial r} + \frac{\partial v_z}{\partial z} \right), \quad (\text{A.23})$$

which is Equation 4.11.

Finally, integrating Equation 4.11 or A.23 with respect to time,

$$p_1 = c_s^2 \rho_1 = \frac{-\rho_0 c_s^2}{r} \int \frac{\partial(rv_r)}{\partial r} dt - \rho_0 c_s^2 \int \frac{\partial v_z}{\partial z} dt, \quad (\text{A.24})$$

$$= \frac{-\rho_0 c_s^2}{r} \int \frac{\partial(r(A(r))\cos(kz-\omega t))}{\partial r} dt - \rho_0 c_s^2 \int \frac{\partial v_z}{\partial z} dt, \quad (\text{A.25})$$

$$= \frac{-\rho_0 c_s^2}{r} \frac{\partial(r(A(r)))}{\partial r} \int \cos(kz-\omega t) dt - \rho_0 c_s^2 \int \frac{\partial v_z}{\partial z} dt. \quad (\text{A.26})$$

Integrating Equation 4.9 with respect to time gives, $v_z = \int -\frac{1}{\rho} \frac{\partial p_1}{\partial z} dt$, thus, substituting this gives,

$$p_1 = c_s^2 \rho_1 = \frac{\rho_0 c_s^2}{r\omega} \frac{\partial(r(A(r)))}{\partial r} \sin(kz-\omega t) + \frac{\rho_0 c_s^2}{\rho\omega} \int \frac{\partial}{\partial z} \left(\int \frac{\partial p_1}{\partial z} dt \right) dt, \quad (\text{A.27})$$

$$= \frac{\rho_0 c_s^2}{r\omega} \frac{\partial(r(A(r)))}{\partial r} \sin(kz-\omega t) + c_s^2 \int \int \frac{\partial^2 p_1}{\partial z^2} dt dt. \quad (\text{A.28})$$

If we let $p_1 = \hat{p}_1 q(kz-\omega t)$ and $\rho_1 = \hat{\rho}_1 q(kz-\omega t)$, where q is representative of a harmonic wave i.e., it could be cos or sin or some combination such as, $q =$

$a \sin(kz - \omega t) + b \cos(kz - \omega t)$. Thus, the right most term of Equation A.28 will give,

$$\int \int \frac{\partial^2 q}{\partial z^2} dt dt, \quad (\text{A.29})$$

$$\frac{\partial^2 q}{\partial z^2} = -k^2 q, \quad (\text{A.30})$$

$$\int \int -k^2 q dt dt = \frac{k^2}{\omega^2} q. \quad (\text{A.31})$$

Since,

$$\frac{\partial^2 \sin(kz - \omega t)}{\partial z^2} = -k^2 \sin(kz - \omega t), \quad (\text{A.32})$$

$$\frac{\partial^2 \cos(kz - \omega t)}{\partial z^2} = -k^2 \cos(kz - \omega t), \quad (\text{A.33})$$

$$\int \int \sin(kz - \omega t) dt dt = -\frac{1}{\omega^2} \sin(kz - \omega t), \quad (\text{A.34})$$

$$\int \int \cos(kz - \omega t) dt dt = -\frac{1}{\omega^2} \cos(kz - \omega t), \quad (\text{A.35})$$

$$(A.36)$$

or any combination of them.

Finally,

$$\hat{p}_1 q = \frac{\rho_0 c_s^2}{r \omega} \frac{\partial(r(A(r)))}{\partial r} \sin(kz - \omega t) + \frac{c_s^2 k^2}{\omega^2} \hat{p}_1 q, \quad (\text{A.37})$$

$$\hat{p}_1 q \left(1 - \frac{c_s^2 k^2}{\omega^2} \right) = \frac{\rho_0 c_s^2}{r \omega} \frac{\partial(r(A(r)))}{\partial r} \sin(kz - \omega t), \quad (\text{A.38})$$

$$p_1 \left(1 - \frac{c_s^2 k^2}{\omega^2} \right) = \frac{\rho_0 c_s^2}{r \omega} \frac{\partial(r(A(r)))}{\partial r} \sin(kz - \omega t), \quad (\text{A.39})$$

$$p_1 = \frac{\rho_0 c_s^2}{\frac{\omega^2}{\omega^2} (\omega^2 - c_s^2 k^2)} \frac{1}{r} \frac{\partial(r(A(r)))}{\partial r} \sin(kz - \omega t), \quad (\text{A.40})$$

$$p_1 = -\frac{\rho_0 c_s^2 \omega}{c_s^2 k^2 - \omega^2} \frac{1}{r} \frac{\partial(r(A(r)))}{\partial r} \sin(kz - \omega t), \quad (\text{A.41})$$

which is Equation 4.12.